APPLIED COMPUTATIONAL ELECTROMAGNETICS SOCIETY JOURNAL

April 2014
Vol. 29 No. 4
ISSN 1054-4887

The ACES Journal is abstracted in INSPEC, in Engineering Index, DTIC, Science Citation Index Expanded, the Research Alert, and to Current Contents/Engineering, Computing & Technology.

The illustrations on the front cover have been obtained from the research groups at the Department of Electrical Engineering, The University of Mississippi.

EMERITUS EDITORIAL ASSISTANTS

APRIL 2014 REVIEWERS

THE APPLIED COMPUTATIONAL ELECTROMAGNETICS SOCIETY

JOURNAL

Vol. 29 No. 4 April 2014

TABLE OF CONTENTS

Convergence Analysis in Deterministic 3D Ray Launching Radio Channel Estimation in Complex Environments

L. Azpilicueta [1], M. Rawat [2], K. Rawat [2], F. Ghannouchi [2] and F. Falcone [1]

[1] Department of Electrical and Electronic Engineering
Public University of Navarre, Pamplona 31006, Spain
leyre.azpilicueta@unavarra.es, francisco.falcone@unavarra.es

[2] Department of Electrical and Computer Engineering
University of Calgary, Calgary, Alberta, Canada
mrawat@ucalgary.ca, krawat@ucalgary.ca, fghannou@ucalgary.ca

Abstract **─** In this paper, a convergence analysis to obtain the optimal calculation parameters in an in-house 3D ray launching algorithm to model the radio wave propagation channel in complex indoor environments is presented. Results show that these parameters lead to accurate estimations with reduced computational time. In addition, simulation results of an indoor complex scenario in terms of received power and power delay profile are presented, showing significant influence of multipath propagation in an indoor radio channel. The adequate election of simulation parameters given by convergence conditions, can aid in optimizing required computational time.

Index Terms – Convergence analysis, 3D ray launching, radio channel simulation, radio wave propagation.

I. INTRODUCTION

With the growing demand for wireless communication services in the last two decades, a radioplanning tasks for these systems is compulsory. Thus, a thorough analysis of indoor propagation channel characteristics represents a fundamental step toward the design and the implementation for an efficient setup of an indoor wireless network.

Traditionally, empirical methods were used (such as COST-231, Walfish-Bertoni, Okumura-Hata, etc.) for initial coverage estimation [1-3]. These empirical models can give rapid results but cannot take into account site-specific features, exhibiting limited accuracy. As an alternative, deterministic methods have been proposed [4-10] based on numerical approaches involving either solution of Maxwell's equations using full-wave simulation techniques, such as method of moment (MoM) and finite difference time domain (FDTD) [11]; or, using geometrical approximations such as Ray Launching (RL) [12] and Ray Tracing (RT) [13]. During the 1990s, RL and RT were both classified as ray tracing methods; although, more recently the differences between both methods have been distinguished. RL is based on the fact that a transmitter launches thousands of test rays in a solid angle and the true path is determined by searching for the rays arriving at the receiver; whereas, RT estimates the principal radio wave propagation regions and rays are traced in such regions. These methods are precise but are time-consuming due to inherent computational complexity. Their combination with Uniform Theory of Diffraction (UTD) [14] is frequently applied to radio coverage prediction [15-18]. RT and RL models potentially represent the most accurate and versatile methods for urban and indoor multipath propagation characterization. Nevertheless, the computational time in conventional ray launching defined by the Shooting-and-Bouncing-Ray (SBR) method [19], can be very large depending on the required accuracy of the results.

A prerequisite to the modeling of complex environments with standard computer equipment,

Submitted On: July 10, 2013
Accepted On: April 17, 2014

1054-4887

is an outstanding reduction of memory efforts with an accurate approach. In [20], Weinmann presents a new efficient approach in order to assess the simulation of scattered fields from arbitrary metallic objects with a ray tracing algorithm, which combines the principles of Physical Optics (PO) and the Physical Theory of Diffraction (PTD). This paper demonstrates that both CPU time and accurate results depend strongly on the number of rays N and the accuracy of the geometric model. The treatment of multiple interactions in a GO-PO approach has been studied in [21], showing that on one hand the multiple PO approach indeed is more accurate. On the other hand, the simulation efforts increase exponentially with the order of the reflection, which makes multiple PO not applicable to more than double reflections. In [22], a description of a novel implementation of diffracted rays according to the Uniform Theory of Diffraction (UTD) concept into a SBR code is presented, describing a convergence analysis with respect to the number of diffracted rays and in terms of multiple diffractions. In [23], a Geometrical Ray Implementation for Mobile Propagation Modeling (GRIMM) is presented, which splits the 3-D ray construction problem into two successive two-dimensional (2-D) stages, without loss of generality and with a great gain in time and simplicity. This permits to take into account reflections and diffractions in any order to meet convergence. In [24], a convergence analysis of a refined ray-tracing algorithm is carried out with respect to the propagation time and the number of bounces.

It is proved that an increase of the number of rays and angular resolution in a SBR approach achieves satisfying results but leads to the significant drawback of higher computational time [20]. Therefore, it is relevant to study the convergence of the results when using ray tracing methods.

In this work, an analysis of the convergence of an in-house developed 3D ray launching algorithm has been presented with respect to the computational time, the angular resolution of the shooting rays and the number of reflections considered. This code has been employed as an effective tool to analyze the effect of radio wave propagation in different complex environments [25-28]. Results show the optimal parameters to achieve the commitment between accuracy and computational time in radio wave simulations of complex indoor environments.

This paper is organized as follows: the in-house developed 3D ray launching code is analytically described in sections II and III. Section IV presents the considered scenario for the analysis and the convergence analysis of the algorithm, whereas simulation results of the algorithm are discussed in section V. Finally, conclusions are given in section VI.

II. THE RAY-LAUNCHING TECHNIQUE

As it is illustrated in Fig. 1, ray launching techniques are based on identifying a single point on the wave front of the radiated wave, with a ray that propagates along the space following a combination of optic and electromagnetic theories.

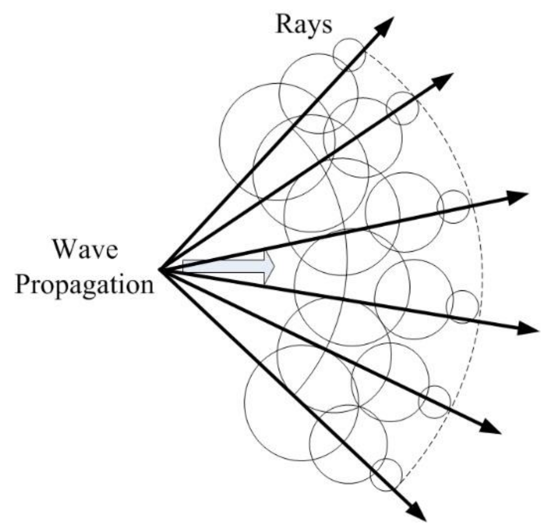

Fig. 1. Wave front propagation with rays associated with single wave front points.

Each ray propagates in the space as a single optic ray. The electric field E created by an antenna with a radiated power P_{rad}, with a directivity $D_t(\theta_t,\Phi_t)$ and polarization ratio $(X^{\perp}, X^{\parallel})$ at distance d in the free space is calculated by [29]:

$$E_i^{\perp} = \sqrt{\frac{P_{rad} D_t(\theta_t,\phi_t)\eta_0}{2\Pi}}\,\frac{e^{-j\beta_0 r}}{d}\,\mathrm{X}^{\perp}L^{\perp}, \quad (1)$$

$$E_i^{\parallel} = \sqrt{\frac{P_{rad} D_t(\theta_t,\phi_t)\eta_0}{2\Pi}}\,\frac{e^{-j\beta_0 r}}{d}\,\mathrm{X}^{\parallel}L^{\parallel}, \quad (2)$$

where $\beta_0 = 2\pi f_c\sqrt{\varepsilon_0\mu_0}$, ε_0=8.854*10^{-12}, μ_0=4π*10^{-7} and η_0=120π. $L^{\perp\parallel}$ are the path loss coefficients for each polarization.

When this ray finds an object in its path, two new rays are created: a reflected ray and a transmitted ray. These rays have new angles provided by Snell's law [30]. Once the parameters of transmission *T* and reflection *R* are calculated and the angle of incidence Ψ_i and Ψ_t, the new angles (θ_r,Φ_r) of the reflected wave and (θ_t,Φ_t) of the transmitted wave can be calculated. A general case where a ray impinges with an obstacle with (θ_i',Φ_i') angles, is represented in Fig. 2. Taking into account all the possible angles of incidence, the new angles for the reflected and transmitted wave are calculated, as it is shown for a general case in Fig. 2.

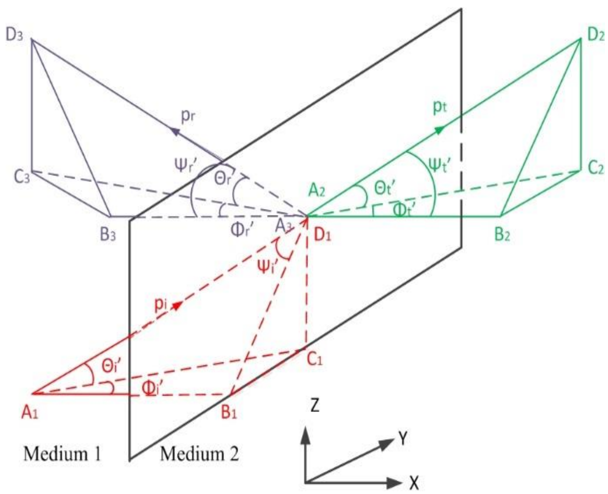

Fig. 2. Reflection and transmission by plane interface at the oblique wave incidence.

The diffracted field is calculated by [31]:

$$E_{UTD} = e_0 \frac{e^{-jks_1}}{s_1} D^{\perp\parallel} \sqrt{\frac{s_1}{s_2(s_1+s_2)}}\, e^{-jks_2}, \quad (3)$$

where s_1, s_2 are the distances represented in Fig. 3, from the source to the edge and from the edge to the receiver point. $D^{\perp\parallel}$ are the diffraction coefficients in (4) given by [31-33] as:

$$D^{\parallel\perp} = \frac{-e^{(-j\pi/4)}}{2n\sqrt{2\pi k}} \begin{Bmatrix} \cot\left(\frac{\pi+(\Phi_2-\Phi_1)}{2n}\right) F\left(kLa^+(\Phi_2-\Phi_1)\right) \\ +\cot\left(\frac{\pi-(\Phi_2-\Phi_1)}{2n}\right) F\left(kLa^-(\Phi_2-\Phi_1)\right) \\ +R_0^{\parallel\perp}\cot\left(\frac{\pi-(\Phi_2+\Phi_1)}{2n}\right) F\left(kLa^-(\Phi_2+\Phi_1)\right) \\ +R_n^{\parallel\perp}\cot\left(\frac{\pi+(\Phi_2+\Phi_1)}{2n}\right) F\left(kLa^+(\Phi_2+\Phi_1)\right) \end{Bmatrix}, \quad (4)$$

where nπ is the wedge angle, *F*, *L* and $a^{\pm}$ are defined in [31], and $R_{0,n}$ are the reflection coefficients for the appropriate polarization for the 0 face or n face, respectively. The Φ_2 and Φ_1 angles in (4) would refer to the angles in Fig. 3.

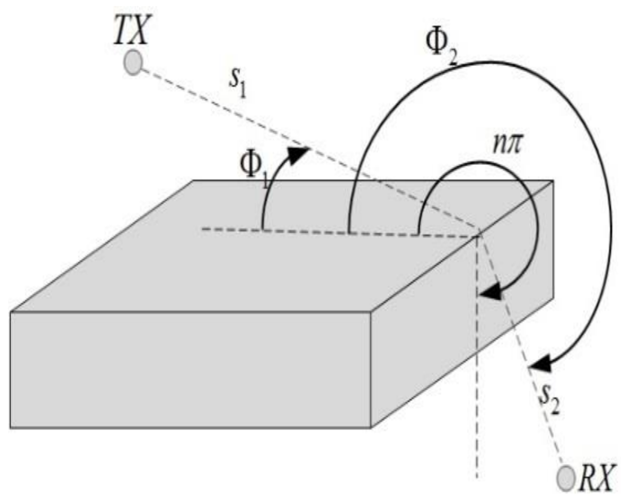

Fig. 3. Geometry for wedge diffraction coefficients.

The received power is calculated at each point taking into account the losses of propagation through a medium (ε, μ, σ) at a distance *d*, with the attenuation constant α (Np/m) and the phase constant β (rad/m). The received power is calculated with the sum of incident electric vector fields in an interval of time Δ_t inside each cuboid of the defined mesh. Based on the above theory, the main characteristic of the ray-launching technique is that it provides the impulse response of the channel *h* (*t*, *fc* , *Δf, d*) for each transmitter, at a given carrier frequency, *fc*, at a given bandwidth (*fc* ± *Δf*), where the materials have a similar response and at a given position. With this information, a stationary channel can be wholly characterized.

III. THE 3D RAY-LAUNCHING ALGORITHM

The developed in-house 3D ray-launching algorithm has three phases:

- Phase I: Scenario creation
- Phase II: 3D ray-launching simulation
- Phase III: Analysis results

In phase I, the 3D scenario is created by considering several objects, walls, transmitters, receivers and the whole components of the environment. It is important to emphasize that a grid is defined in the space to save the parameters of each ray. Accordingly, the environment is divided into a number of cuboids of a fixed size. When a ray enters a specific hexahedron, its parameters are saved in a matrix. Parameters such as frequency of operation, radiation patterns of the antennas, number of multipath reflections, separation angle between rays and cuboid dimension can be modified in the algorithm. In order to achieve adequate values, it is highly important to take into account, not only the parameters which result in more accurate results, but also the computational time, which can be substantial for a complex environment.

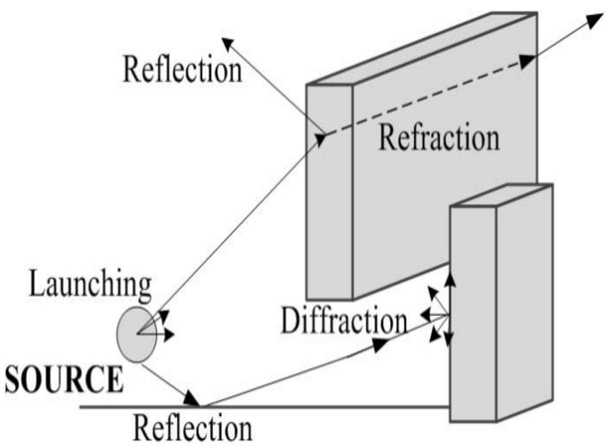

Fig. 4. Principle of operation of the in-house developed 3D ray launching code.

In phase II, rays are launched and they propagate along the space interacting with the obstacles, causing physical phenomena such as reflection, refraction and diffraction, as shown in Fig. 4. The parameters of these rays are stored as they enter to each hexahedral until the ray has a certain number of reflections or it has exceeded the pre-propagation time set. The algorithm operates in an iterative manner, considering a ray and its reflections and storing the created ray for processing later the diffraction contribution. Figure 5 shows the different steps of this phase of the algorithm.

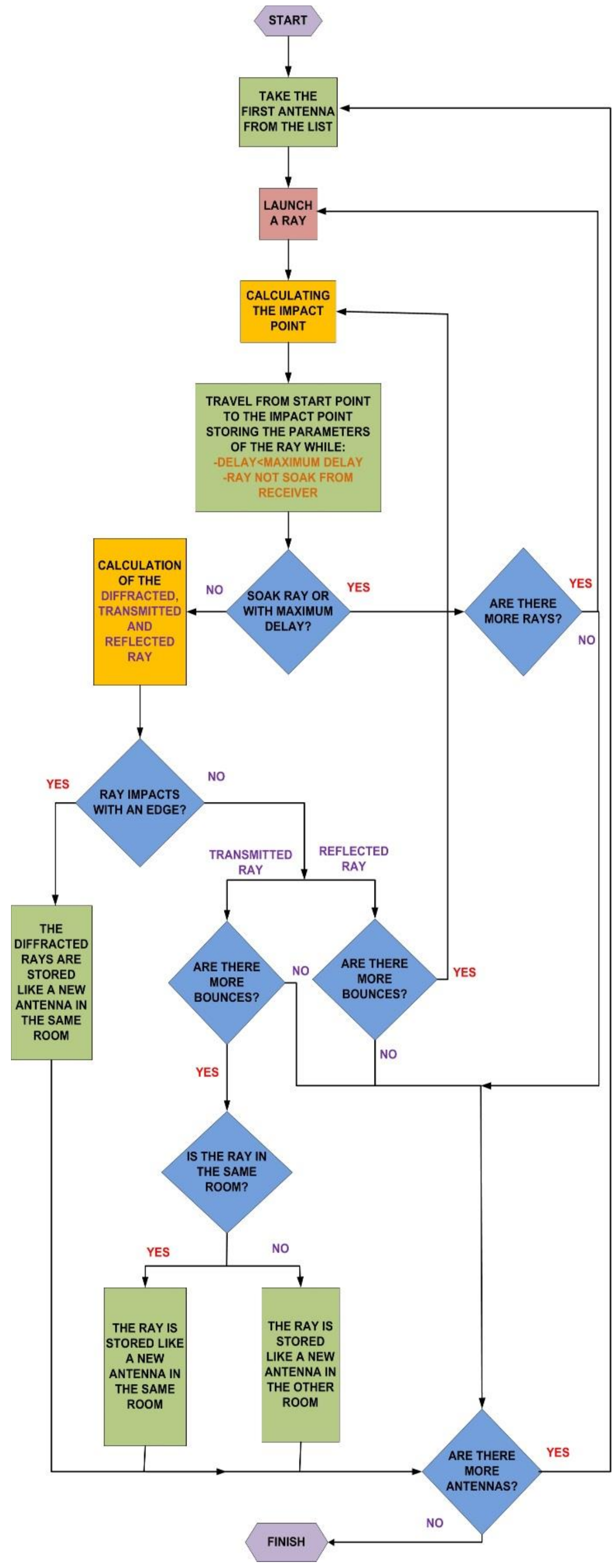

Fig. 5. Functional diagram of the 3D ray launching algorithm.

In phase III, by using the parameters stored in phase II and considering the predefined transmitter's characteristics, such as radiated power, the emitting antenna's directivity *(θ,Φ)*, wave polarization and the carrier frequency, it is possible to easily derive the relevant parameters for channel modeling.

IV. CONVERGENCE ANALYSIS

In principle, it can be stated that simulation results tend to be more accurate whether more rays are launched and more reflections are considered. However, computational time has to be taken into account in order to obtain accurate results with an acceptable time span.

In this work, the influence of considering a different number of reflections and launching rays has been done. For that purpose, two different angular resolutions of launching rays have been considered and analyzed, versus the number of reflections. Afterwards, once the optimal number of reflections has been obtained, the assessment of the most accurate angular resolution of launching rays has been done taking into account the computational time.

The scenario under consideration is a complex environment, which corresponds to several rooms of the iRadio Laboratory of the University of Calgary. A schematic view of the scenario is represented in Fig. 6.

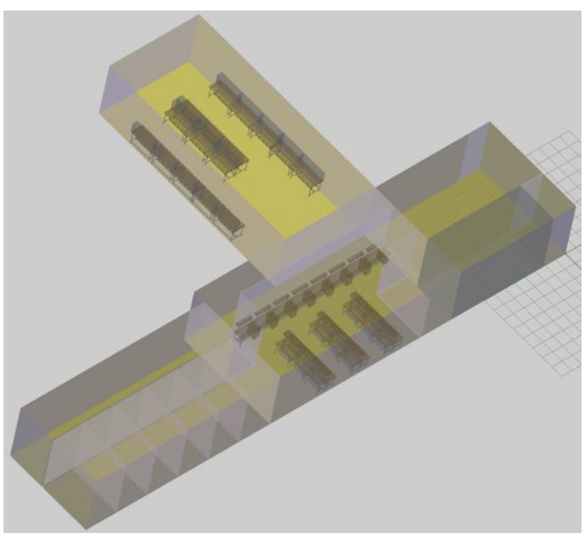

Fig. 6. Complete scenario of iRadio Laboratory of the University of Calgary.

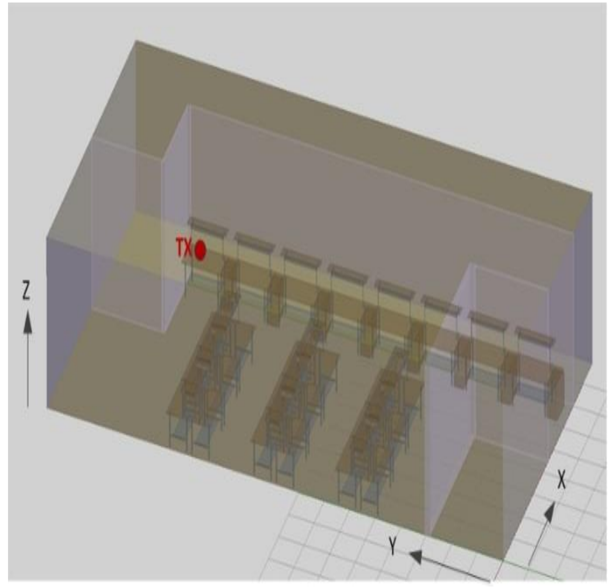

Fig. 7. Detail of room 2 of the complete scenario representing the iRadio Laboratory.

Within the complete scenario, only one room has been chosen to analyze exhaustively, room 2, which is depicted in detail in Fig. 7. The red point in this figure corresponds to the transmitter antenna, which is placed at the point (X=6.24 m, Y=16.94 m and Z=0.96 m). All the elements within the scenario have been taking into account (i.e. the different dimension and distribution of tables and chairs and walls). The material parameters used in the simulation models are defined in Table 1 [34].

Table 1: Material parameter definition

Material Properties in the Ray Launching Simulation		
Material	Permittivity (ε_r)	Conductivity (σ)[S/m]
Air	1	0
Aluminum	4.5	$4*10^7$
Glass	6.06	10^{-12}
Wood	3	0.0006
Brick wall	5.2	0.028

A. Convergence versus the number of reflections

First, a convergence analysis of the algorithm versus the number of reflections that the ray could impact with the obstacles and walls has been obtained. Different cases have been considered varying the number of reflections. These cases correspond to different angular resolutions when the rays are launched, as shown in Table 2.

Table 2: Different cases considered for simulation versus the number of reflections

	$N_{launching\ rays}$	$\Delta\Phi=\Delta\theta$
Case 0	16200	2º
Case 1	64800	1º
Case 2	259200	0.5º

Table 3: Simulation parameters

Ray Launching Parameters	
Frequency	2.4 GHz
Transmitter power	20 dBm
Cuboids resolution	12x12x12 cm
Transmitter point	(X=6.24 m,Y=16.94 m and Z=0.96 m)

Case 1 and case 2 have been analyzed versus the number of reflections and simulation, parameters for both cases are shown in Table 3.

Figures 9, 10, 11 and 12 depict simulation results for case 1. The mean value and the standard deviation of power (dBm) for different X and Z and along the Y-axis are presented. These linear radials correspond to the red lines in Figs. 8 (a) and (b). The mean power values exhibits large variability, due to the influence of the morphology and topology of the scenario. Therefore, the way in which the elements within the indoor scenario are configured and the different material properties play a fundamental role in the overall performance of the network.

The standard deviation of power decreases as the number of reflections increases and converges approximately for six reflections in all cases, which implies that the maximum efficiency of the algorithm will be reached when six reflections are considered.

Figure 10 shows the linear regression lines of the received power for different locations in the X axis, along the Y-axis and for different heights. It is demonstrated that when the number of reflections considered in the algorithm has been increased, the algorithm tends to converge and it exhibits the same behavior from a threshold value for the number of reflections, corresponding to six reflections. In all cases, the trend is to decrease over distance and it is observed that with more reflections the slope of the lines is smaller.

Figure 11 shows the mean and the standard deviation of power (dBm) for different Y and Z locations and along the X-axis (green lines in Fig. 8 (a)). It is observed that mean power converges as the number of reflections increases. Besides, the standard deviation of the received power decreases and also converges at approximately six reflections.

Figure 12 shows the linear regression lines of the received power for different values in Y axis and heights and along the X-axis. It is observed that for smaller values in the Y axis, the slope of the lines is smaller as the number of reflections increases. From Y=6 m, figures of smaller heights show more variability due to the obstacles within the ray path. Lines converge as the number of reflections is increased. From Y=12 m, power increases along the X-axis due to the proximity of the transmitter antenna.

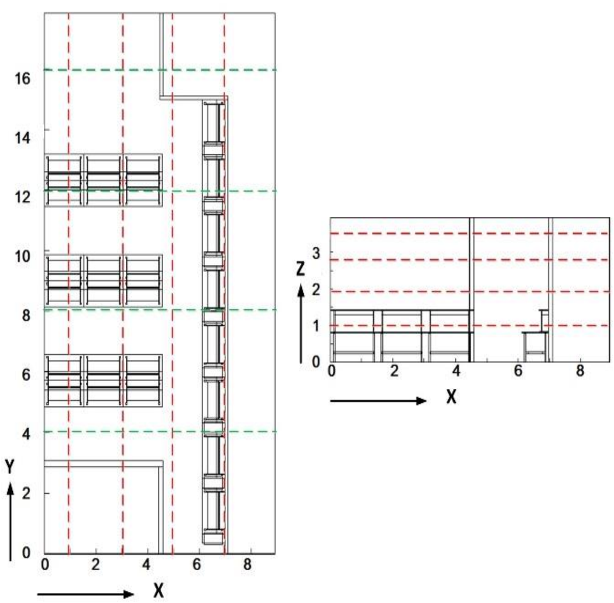

(a) (b)

Fig. 8. Schematic representation of the linear TX-RX distances chosen for the convergence analysis of the algorithm: (a) along the X-axis and the Y-axis and (b) different heights in the Z-axis.

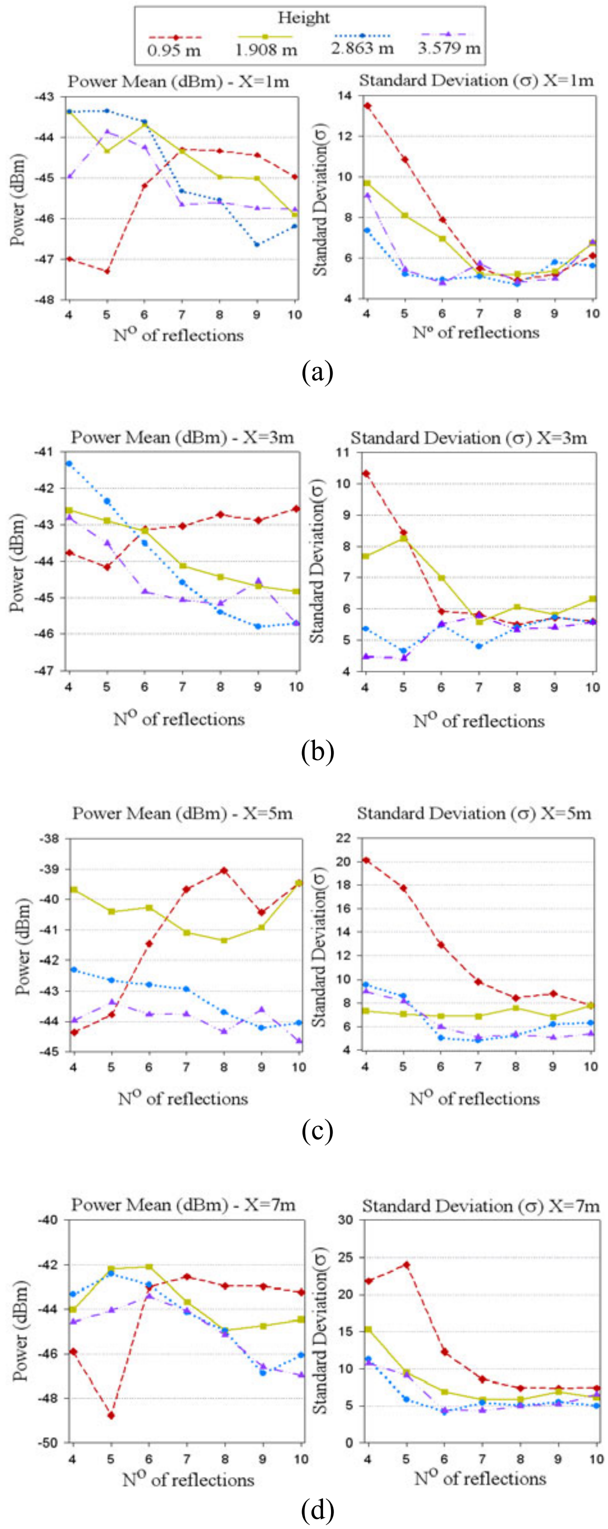

Fig. 9. Mean and standard deviation of power for different X and Z versus the number of reflections with $N_{\text{launching rays}}$=64800: (a) X=1 m, (b) X=3 m, (c) X=5 m and (d) X=7 m.

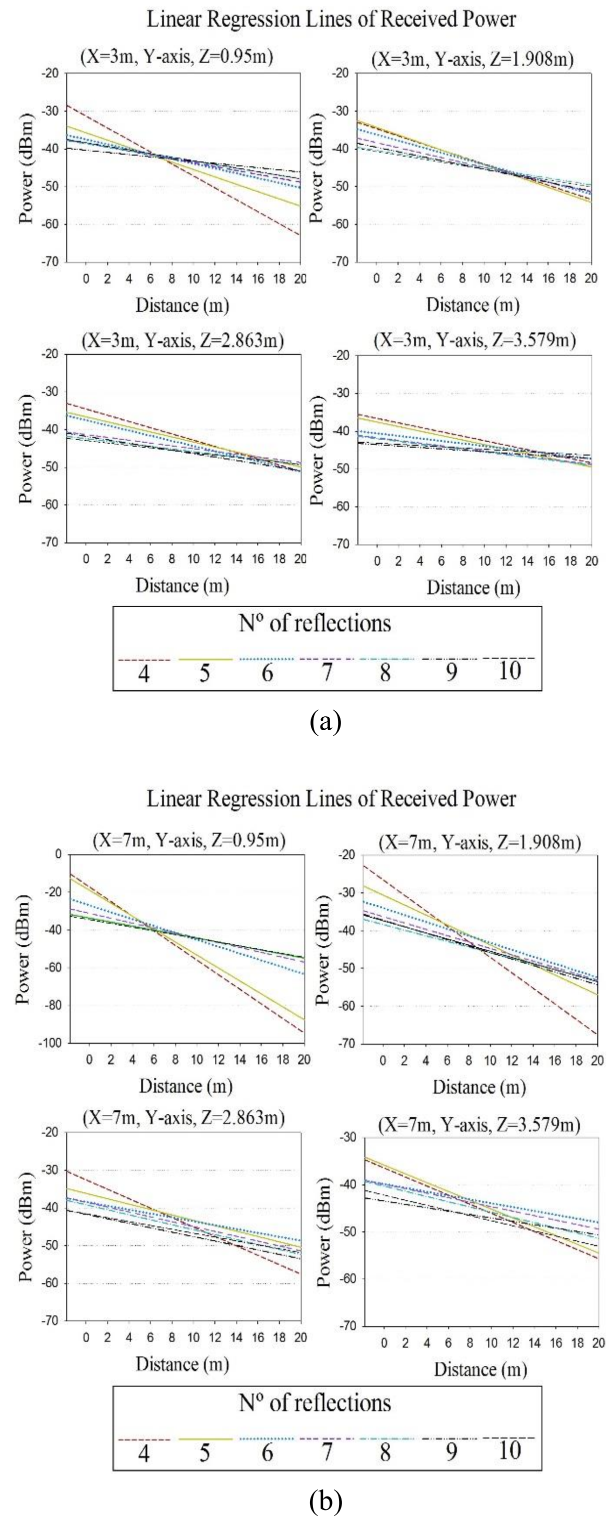

Fig. 10. Linear regression lines of the received power for different X, along the Y-axis and for different heights with $N_{\text{launching rays}}$=64800: (a) X=3 m and (b) X=7 m.

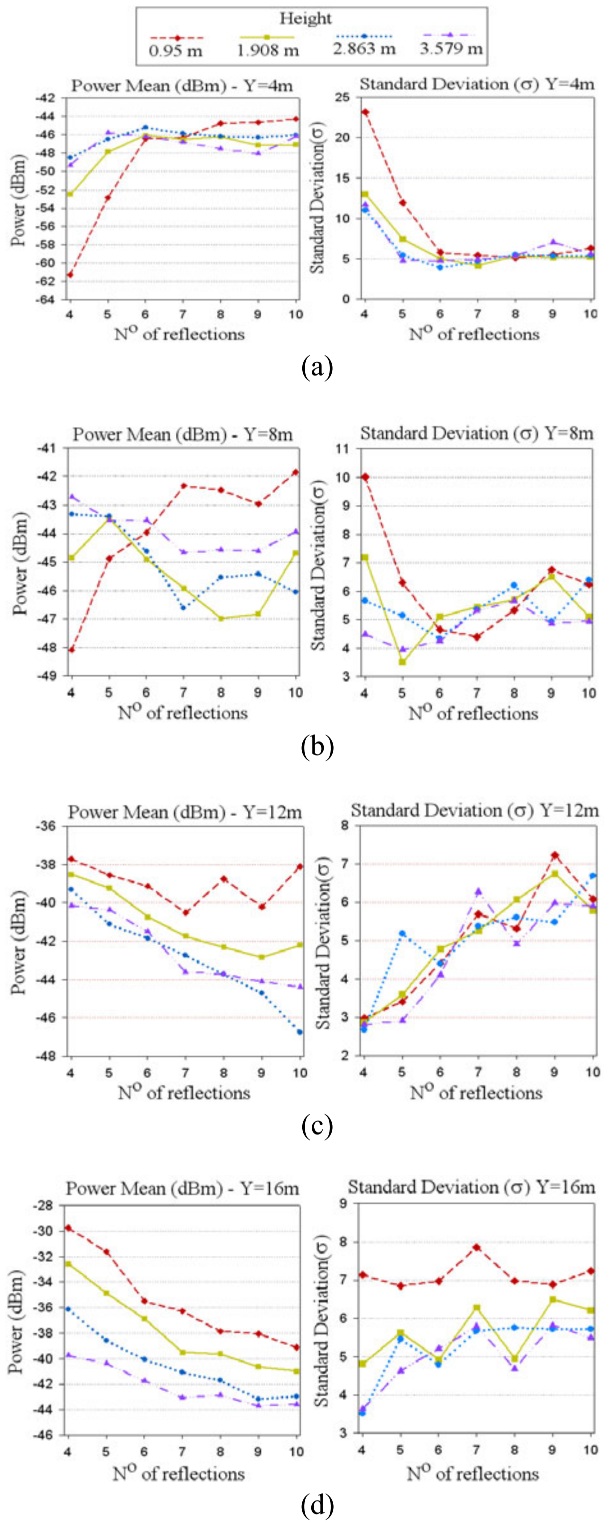

Fig. 11. Mean and standard deviation of power for different Y and Z versus the number of reflections with $N_{\text{launching rays}}$=64800: (a) Y=4 m, (b) Y=8 m (c) Y=12 m and (d) Y=16 m.

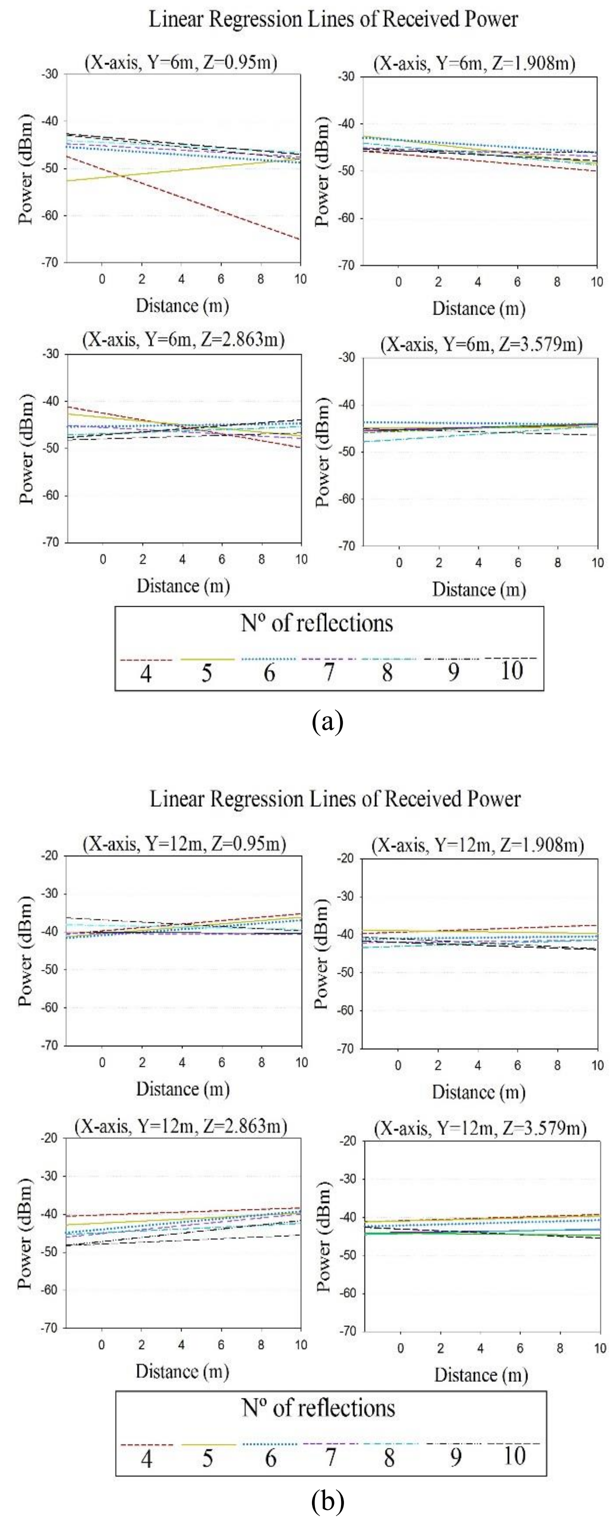

Fig. 12. Linear regression lines of the received power for different Y, along the X-axis and for different heights with $N_{\text{launching rays}}$=64800: (a) Y=6 m and (b) Y=12 m.

In order to validate previous results, which conclude that six reflections must be considered in complex indoor scenarios, the same analysis has been done with a lower angular resolution (case 2 in Table 2). This implies that the number of shooting rays is increased to test if the number of rays has an influence in the algorithm convergence. Simulation parameters are shown in Table 3.

Figure 13 represents the mean and the standard deviation of power (dBm) for different X and Z, along the Y-axis, with $\Delta\ \Phi = \pi/360$ and $\Delta\theta = \pi/360$. As in the previous case, large variability in the mean of the received power is observed, due to the influence of the morphology and topology of the scenario and multipath fading, which is a relevant phenomenon in this type of indoor scenarios. The standard deviation of the power does not converge as clearly as in the previous case. However, Figs. 13 (b) and (d) depict convergence of the algorithm.

The linear regression lines of the received power for different X, along the Y-axis and for different heights with angular resolution of launching rays of 0.5º, are presented in Fig. 14. It is observed that in all cases the received power decreases with the distance and the slope of the lines are smaller as the number of reflections increases. In case 2, the algorithm converges with one reflection less considered because of the rise of launching rays. The slope of the regression lines in Figs. 14 and 16 are for every height, smaller than case 1; therefore, the number of considered reflections to achieve the convergence is smaller.

However, the computational time is also deeply important. Simulations have been performed in an Intel Xeon CPU X5650 @ 2.67 GHz and 2.66 GHz. In case 2, the computational complexity is increased overall. Figure 17 shows the simulation time of the considered scenario depending on the number of reflections and the number of launching rays. Computational time with angular resolution of 0.5º (case 2) is hugely greater than case 1, with angular resolution of 1º for each number of reflections considered. It can be seen that the optimal parameters to achieve the most accurate results with an acceptable computational time, is to consider six reflections and angular resolution of launching rays of 1º.

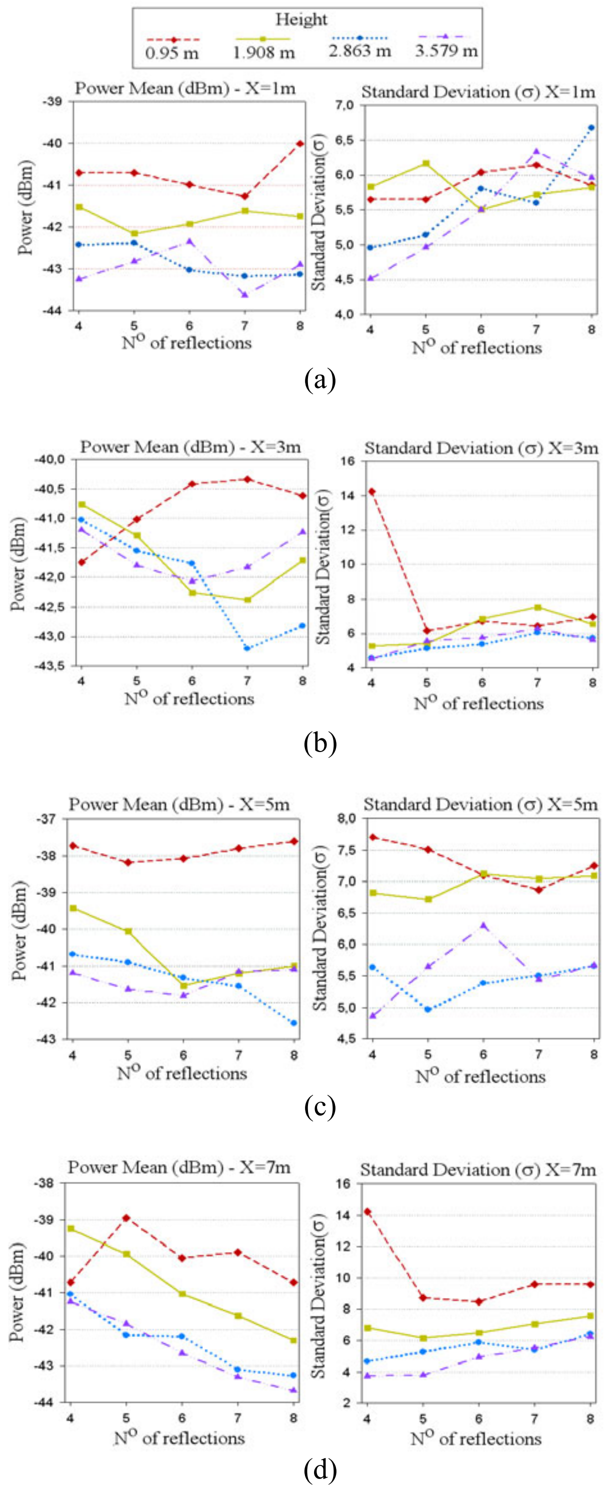

Fig. 13. Mean and standard deviation of power for different X and Z versus the number of reflections with $N_{launching\ rays}$=259200: (a) X=1 m, (b) X=3 m, (c) X=5 m and (d) X=7 m.

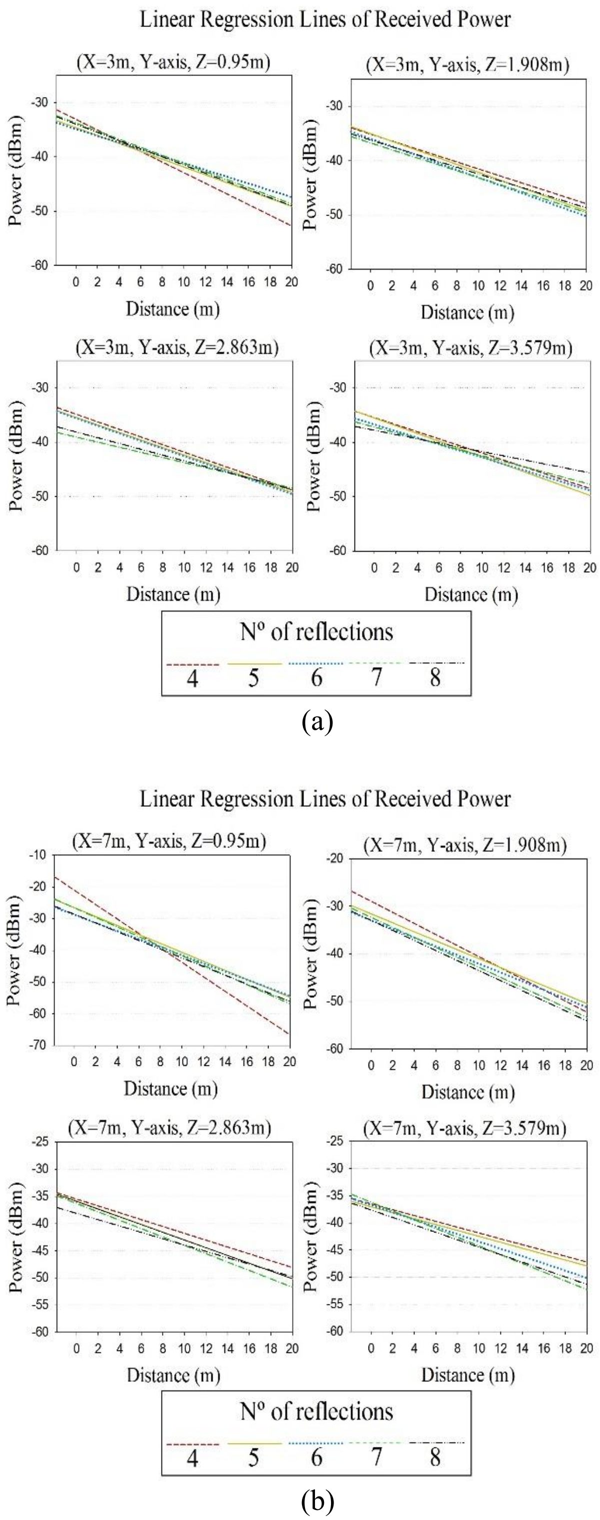

Fig. 14. Linear regression lines of the received power for different X, along the Y-axis and for different heights with $N_{launching\ rays}$=259200: (a) X=3 m and (b) X=7 m.

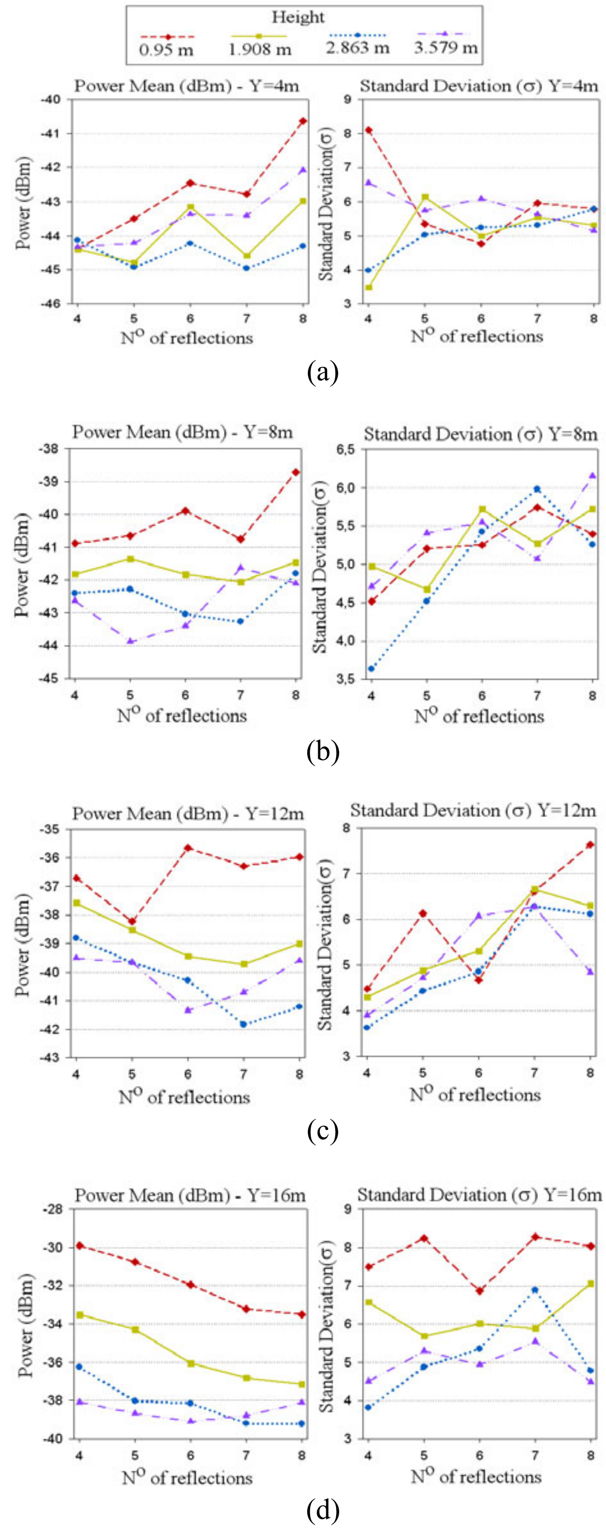

Fig. 15. Mean and standard deviation of power for different Y and Z versus the number of reflections with $N_{launching\ rays}$=259200: (a) Y=4 m, (b) Y=8 m, (c) Y=12 m and (d) Y=16 m.

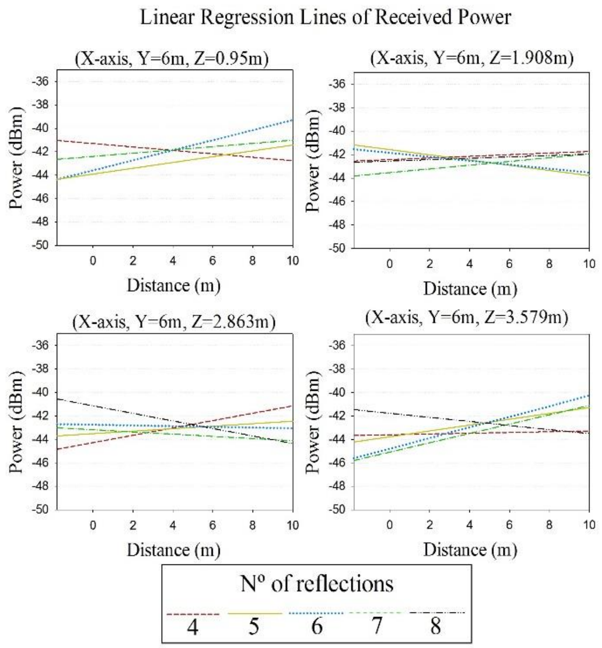

(a)

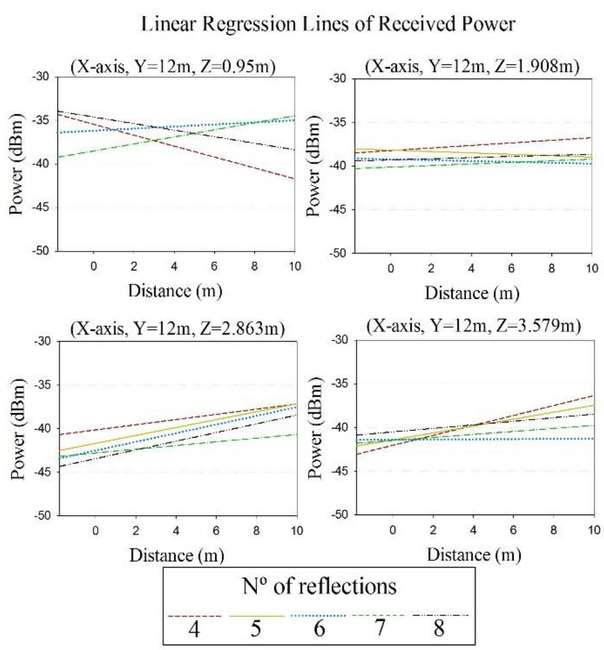

(b)

Fig. 16. Linear regression lines of the received power for different Y, along the X-axis and for different heights with $N_{\text{launching rays}}$=259200: (a) Y=6 m and (b) Y=12 m.

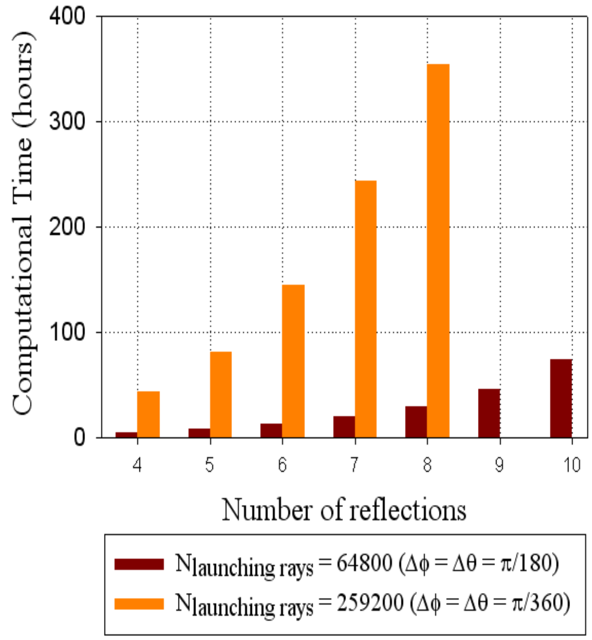

Fig. 17. Comparison of computational time versus different number of launching rays and different number of reflections considered in the algorithm.

B. Convergence versus the number of launching rays

In order to validate the results obtained in the previous section, an analysis of the convergence of the algorithm versus the number of launching rays has been performed considering six reflections. Figures 18 and 19 show the mean and the standard deviation of power for different locations in the X, Y axes and heights, in comparison with the three cases shown in Table 2. It can be seen that mean value of received power increases as the number of shooting rays is increased, which is in agreement with previous results in the sense that the algorithm is more accurate with more shooting rays. Alternatively, the standard deviation of power decreases sharply for case 0 to case 1, and converges in all cases in case 1, which corresponds to angular resolutions of 1º. Accordingly, these results validate the previous statements taking into account the high amount of CPU-time required to analyze the large amount of rays of case 3, which is shown in Fig. 20.

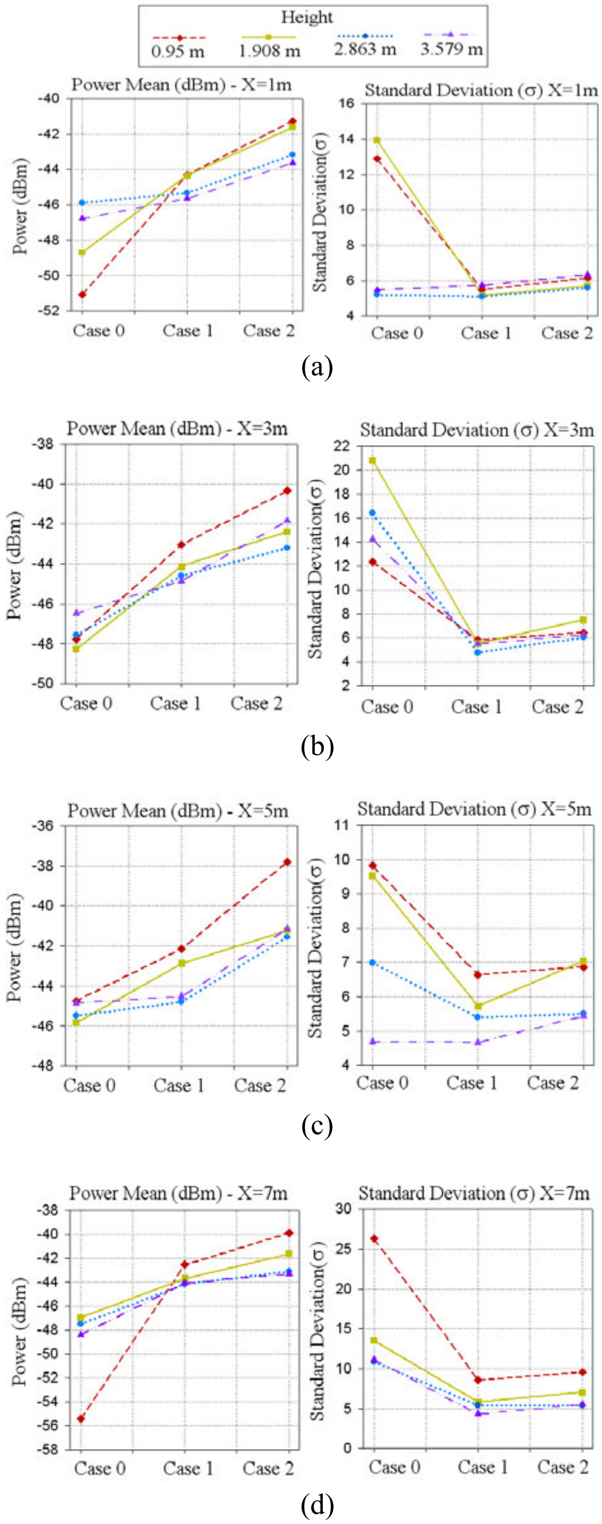

Fig. 18. Mean and standard deviation of power in room 2 versus different cases of shooting rays for different X.

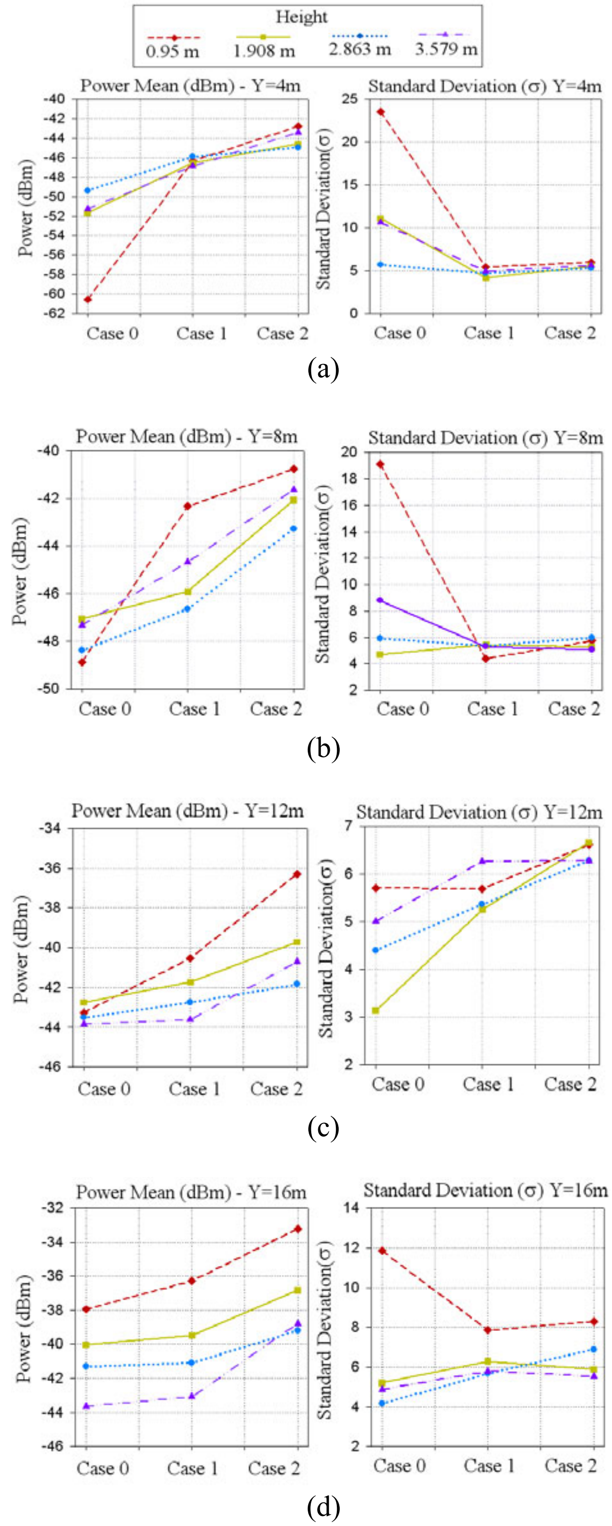

Fig. 19. Mean and standard deviation of power in room 2 versus different cases of shooting rays for different Y.

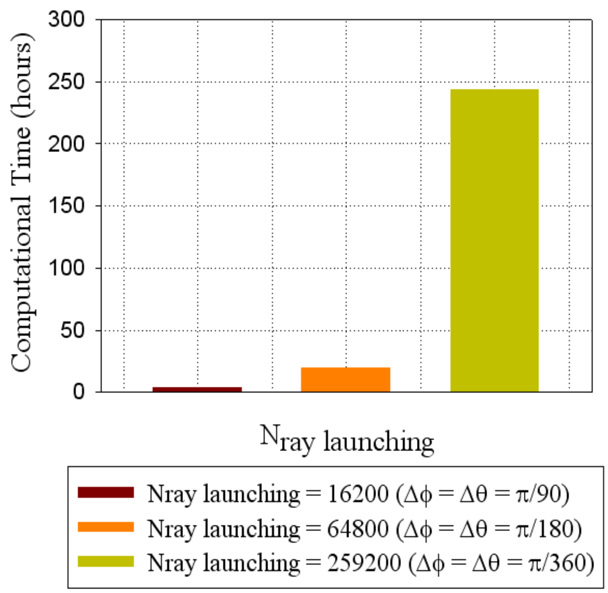

Fig. 20. Comparison of computational time versus different number of launching rays.

V. SIMULATIONS RESULTS

In order to gain insight in the effect of parameter variation in wireless channel estimation, several test cases have been simulated. Figure 21 shows the estimated received power for two different heights in the indoor scenario of the iRadio Laboratory (depicted in Fig. 7). Simulations have been performed with the parameters shown in Table 3, with an angular resolution of one degree and six reflections.

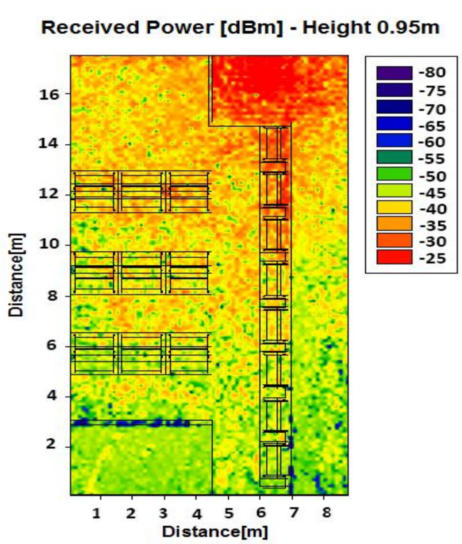

(a)

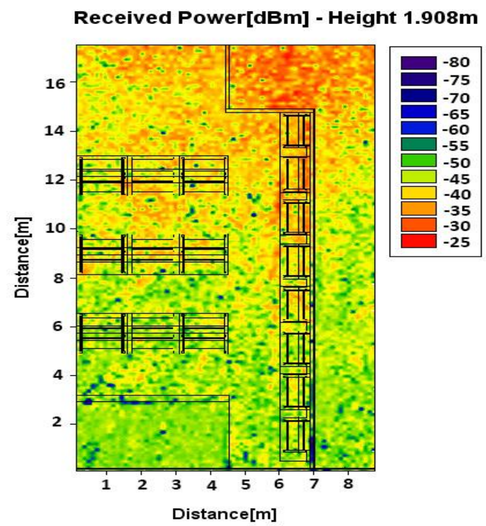

(b)

Fig. 21. Bi-dimensional planes of estimated received power: (a) hight 0.95 m and (b) height 1.908 m.

To illustrate the relevance of the multipath effect, the power delay profile has been predicted along for x=3 m, y=12 m and z=1.908 m, as shown in Fig. 22. It can be seen that there are a large number of echoes in the scenario, due to multipath propagation, which is the most important phenomena in this type of indoor scenarios.

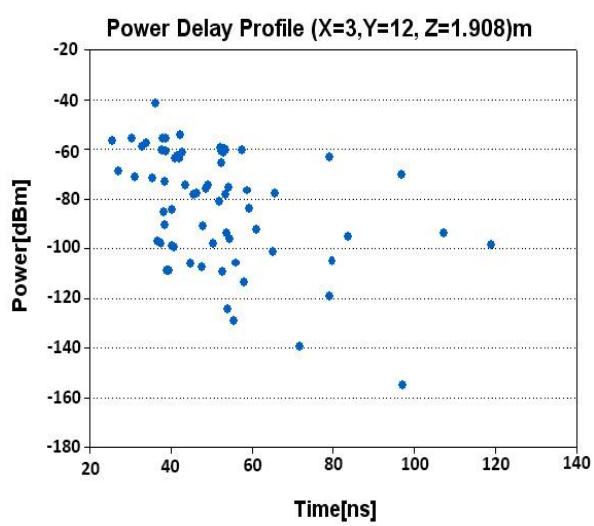

Fig. 22. Power-delay profile for: x=3 m, y=12 m and z=1.908 m, in the considered scenario.

VI. CONCLUSION

In this work, the convergence analysis to obtain the optimal parameters to introduce in a 3D in-house implemented ray launching code have been presented. Results show that adequate election of parameters such as ray angular resolution, number of reflections and cuboid resolution, lead to accurate results with adequate computational time as a consequence of algorithm convergence. In addition, simulation results of an indoor complex scenario in terms of received power and power delay profile are presented, showing the significant influence of multipath propagation in an indoor radio channel. These results can aid in the correct development of radioplanning tasks with optimal computational time.

ACKNOWLEDGMENT

The authors wish to acknowledge the financial support of project TEC2010-21563-C02-01 ENEIDA, funded by the Ministry of Science, Spain.

REFERENCES

[1] M. Hata, "Empirical formula for propagation loss in land mobile radio services," *IEEE Trans. Antennas and Propag*., vol. 29, no. 3, pp. 317-325, 1980.

[2] F. Ikegami, S. Yoshida, T. Takeuchi and M. Umehira, "Propagation factors controlling mean field strength on urban streets," *IEEE Trans. Antennas and Propa*g., vol. 32, no. 8, pp. 822-829, 1984.

[3] S. Phaiboon and P. Phokharatkul, "Path loss prediction for low-rise buildings with image classification on 2-D aerial photographs," *Progress in Electromagnetics Research*, vol. 95, pp. 135-152, 2009.

[4] S. H. Lee, "A photon modeling method for the characterization of indoor optical wireless communication," *Progress in Electromagnetics Research*, vol. 92, pp. 121-136, 2009.

[5] D. J. Y. Lee and W. C. Y. Lee, "Propagation prediction in and through buildings," *IEEE Trans. Veh. Tech*., vol. 49, no. 5, pp. 1529-1533, 2000.

[6] S. Y. Tan and H. S. Tan, "A microcellular communications propagation model based on the uniform theory of diffraction and multiple image theory," *IEEE Trans. Antennas and Propag*., vol 44, no. 10, pp. 1317-1326, 1996.

[7] A. G. Kanatas, I. D. Kountouris, G. B. Kostaras and P. Constantinou, "A UTD propagation model in urban microcellular environments," *IEEE Trans. Veh. Tech*., vol. 46, no. 1, pp. 185-193, 1997.

[8] A. G. Dimitriou and G. D. Sergiadis, "Architectural features and urban propagation," *IEEE Trans. Antennas and Propag*., vol. 54, no. 3, pp. 774-784, 2006.

[9] M. Franceschetti, J. Bruck and L. J. Schulman, "A random walk model of wave propagation," *IEEE Trans. Antennas and Propag*., vol. 52, no. 5, pp. 1304-1317, 2004.

[10] J. Blas Prieto, R. M. Lorenzo Toledo, P. Fernández Reguero, E. J. Abril, A. Bahillo Martínez, S. Mazuelas Franco and D. Bullido, "A new metric to analyze propagation models," *Progress in Electromagnetics Research*, vol. 91, pp. 101-121, 2009.

[11] J. W. Schuster and R. J. Luebbers, "Comparison of GTD and FDTD predictions for UHF radio wave propagation in a simple outdoor urban environment," *IEEE Antennas and Propag. Society International Symposium*, vol. 3, pp. 2022-2025, 1997.

[12] S. Y. Seidel and T. S. Rappaport, "Site-specific propagation prediction for wireless in-building personal communication system design," *IEEE Transactions on Vehicular Technology*, vol. 43, no. 4, pp. 879-891, 1994.

[13] C. F. Yang, "A ray-tracing method for modeling indoor wave propagation and penetration," *IEEE Transactions on Antennas and Propagation*, vol. 46, no. 6, pp. 907-919, 1998.

[14] R. G. Kouyoumjian and P. H. Pathak, "A uniform theory of diffraction for an edge in a perfectly conducting surface," *Proc. IEEE*, vol. 62, no. 4, pp. 1448-1462, 1974.

[15] G. Gennarelli and G. Riccio, "A uapo-based model for propagation prediction in microcellular environments," *Progress in Electromagnetics Research B*., vol. 17, pp. 101-116, 2009.

[16] H. W. Son and N. H. Myung, "A deterministic ray tube method for microcellular wave propagation prediction model," *IEEE Trans. Antennas and Propag.*, vol. 47, no. 8, pp. 1344-1350, 1999.

[17] A. Tayebi, J. Gómez, F. S. de Adana and O. Gutierrez, "The application of arrival and received signal strength in multipath indoor environments," *Progress In Electromagnetics Research*, vol. 91, pp. 1-15, 2009.

[18] H. B. Song, H. G. Wang, K. Hong and L. Wang, "A novel source localization scheme based on unitary esprit and city electronic maps in urban environments," *Progress In Electromagnetics Research*, vol. 94, pp. 243-262, 2009.

[19] H. Ling, R. C. Chou and S. W. Lee, "Shooting and bouncing rays: calculating the RCS of an arbitrarily

shaped cavity," *IEEE Transactions on Antennas and Propagation*, vol. 37, pp. 194-205, 1989.

[20] F. Weinmann, "Ray tracing with PO/PTD for RCS modeling of large complex objects," *IEEE Transactions on Antennas and Propagation*, vol. 54, nº. 6, pp. 1797-1806, 2006.

[21] T. Griesser and C. A. Balanis, "Backscatter analysis of dihedral corner reflectors using physical optics and the physical theory of diffraction," *IEEE Transactions on Antennas and Propagation*, vol. 35, pp. 1137-1147, October 1987.

[22] F. Weinmann, "UTD shooting-and-bouncing extension to a PO/PTD ray tracing algorithm," *Applied Computational Electromagnetics Society Journal*, vol. 24, nº. 3, pp. 281-293, 2009.

[23] J. P. Rossi and Y. Gabillet, "A mixed ray launching/tracing method for full 3-D UHF propagation modeling and comparison with wide-band measurements," *IEEE Transactions on Antennas and Propagation*, vol. 50, nº. 4, pp. 517-523, 2002.

[24] B. Choudhury, H. Singh, J. P. Bommer and R. M. Jha, "RF field mapping inside a large passenger-aircraft cabin using a refined ray-tracing algorithm," *IEEE Antennas and Propagation Magazine*, vol. 55, nº. 1, pp. 276-288, 2013.

[25] L. Azpilicueta, F. Falcone, J. J. Astráin, J. Villadangos, I. J. García Zuazola, H. Landaluce, I. Angulo and A. Perallos, "Measurement and modeling of a UHF-RFID system in a metallic closed vehicle," *Microwave and Optical Technology Letters*, vol. 54, issue 9, pp. 2126-2130, 2012.

[26] J. A. Nazábal, P. López Iturri, L. Azpilicueta, F. Falcone and C. Fernández-Valdivielso, "Performance analysis of IEEE 802.15.4 compliant wireless devices for heterogeneous indoor home automation environments," *International Journal of Antennas and Propagation*, Hindawi Publishing Corporation, 2012.

[27] S. Led, L. Azpilicueta, E. Aguirre, M. Martínez de Espronceda, L. Serrano and F. Falcone, "Analysis and description of HOLTIN service provision for AECG monitoring in complex indoor environments," *Sensors*, vol. 13, issue 4, pp. 4947-4960, 2013.

[28] P. López Iturri, J. A. Nazábal, L. Azpilicueta, P. Rodriguez, M. Beruete, C. Fernández-Valdivielso and F. Falcone, "Impact of high power interference sources in planning and deployment of wireless sensor networks and devices in the 2.4 GHz frequency band in heterogeneous environments," *Sensors*, vol. 12, issue 11, pp. 15689-15708, 2012.

[29] A. Cardama Aznar, "Antenas," *Edicions UPC*, 1993.

[30] H. D. Hristov, "Fresnel zones in wireless links, zone plate lenses and antennas," *Artech House, Inc.*, 2000.

[31] Recomendattion UIT-R, p. 526-11, s. l., "Propagación por difracción, serie p. propagación de las ondas radioeléctricas," October 2009.

[32] R. J. Luebbers, "A heuristic UTD slope diffraction coefficient for rough lossy wedges," *IEEE Transactions on Antennas and Propagation*, vol. 37, pp. 206-211, 1989.

[33] R. J. Luebbers, "Comparison of lossy wedge diffraction coefficients with application to mixed path propagation loss prediction," *IEEE Transactions on Antennas and Propagation*, vol. 36, nº. 7, pp. 1031-1034, 1988.

[34] C. A. Balanis, "Advanced engineering electromagnetics," *Wiley New York,* vol. 205, 1989.

Leire Azpilicueta received her Telecommunications Engineering Bachelor degree from the Public University of Navarre (UPNa), Pamplona, Spain in 2009. In 2010, she worked in the R&D department of RFID Osés as a Radio Engineer. In 2011, she obtained her Master of Communications degree held by the Public University of Navarre. She is currently pursuing her Ph.D. degree in Telecommunication Engineering. Her research interests are mobile radio systems, wireless communications and channel modeling.

Meenakshi Rawat (S'09) received her B.Tech. degree in Electrical Engineering from Govind Ballabh Pant University of Agriculture and Technology, Pantnagar, Uttaranchal, India in 2006 and her Ph.D. degree from Schulich School of Engineering, University of Calgary, Calgary, AB, Canada in 2012. She was associated with Telco Construction Equipment Co. Ltd., India from 2006-2007 and Hindustan Petroleum Corporation Limited (HPCL), India during 2007-2008. She is now working with the iRadio Lab of the Schulich School of Engineering, University of Calgary as a as Post-Doctoral-Research fellow. Her current research interests are in the area of digital signal processing, nonlinear filters, artificial neural networks and microwave active and passive nonlinear circuit modeling.

Karun Rawat (M'08, S'09) received his B.E. degree in Electronics and Communication Engineering from Meerut University, UP, India in 2002 and his Ph.D. in Electrical and Computer Engineering, Schulich School of Engineering, University of Calgary, Calgary, AB, Canada in 2012. He worked as a Scientist in the Indian Space Research Organization (ISRO) from 2003-2007. He also worked in iRadio Laboratory of the Schulich School of Engineering, University of Calgary from 2012-2013, where he has been working as a Post Doctoral Research fellow. Currently, he is an Assistant Professor at Indian Institute of Technology, Delhi. He is a Reviewer of several well-known journals. He was also a leader of the University of Calgary team, which won first prize and the best design award in the 3rd Annual Smart Radio Challenge 2010 conducted by Wireless Innovation Forum. His current research interests are in the areas of microwave active and passive circuit design and advanced transmitter and receiver architecture for software defined radio applications

Fadhel M. Ghannouchi is currently a Professor and iCORE/Canada Research Chair with the Department of Electrical and Computer Engineering, Schulich School of Engineering, University of Calgary, Calgary, AB, Canada and Director of the Intelligent RF Radio Laboratory (iRadio Lab). He has held numerous invited positions with several academic and research institutions in Europe, North America and Japan. He has provided consulting services to a number of microwave and wireless communications companies. He has authored or co-authored over 500 publications. He holds ten U.S. patents with five pending. His research interests are in the areas of microwave instrumentation and measurements, nonlinear modeling of microwave devices and communications systems, design of power and spectrum efficient microwave amplification systems and design of intelligent RF transceivers for wireless and satellite communications.

Francisco Falcone (M'05, SM'09) received his Telecommunications Engineering Degree in 1999 and Ph.D. in Communications Engineering in 2005, both at the Universidad Pública de Navarra (UPNA) in Spain. From 1999 to 2000 he worked as Microwave Commissioning Engineer at Siemens-Italtel. From 2000 to 2008 he worked as a Radio Network Engineer in Telefónica Móviles. In 2009 he co-founded Tafco Metawireless, a spin off devoted to complex EM analysis. From 2003 to 2009 he was also Assistant Lecturer at UPNA, becoming Associate Professor in 2009. He has over 280 contributions in journal and conference publications. He has been recipient of the CST Best Paper award in 2003 and 2005, Best Ph.D. in 2006 awarded by the Colegio Oficial de Ingenieros de Telecomunicación, Doctorate award in 2004-2006 awarded by UPNA, Juan Lopez de Peñalver Young Researcher award in 2010 awarded by the Royal Academy of Engineering of Spain and Premio Talgo in 2012 for Technological Innovation. His research area is artificial electromagnetic media, complex electromagnetic scenarios and wireless system analysis.

The Error Cross-Section Method for Quantifying the Error in Electromagnetic Scattering Problems

Ahmed M. Kord and Islam A. Eshrah

Department of Electronics and Electrical Communications Engineering
Cairo University, Faculty of Engineering, Giza, Egypt
akord@ieee.org, isattar@eng.cu.edu.eg

Abstract **─** The Error Cross-Section (ECS) is introduced to quantify the error associated with the numerical solution of electromagnetic scattering problems. The ECS accounts for different approximations and inaccuracies in the object discretization and numerical computations. The ECS definition is based on the power conservation principle and is visualized by comparing it to the radar cross-section of a thin wire for two-dimensional (2-D) problems or a small sphere for three-dimensional (3-D) problems. The proposed ECS method is independent of the adopted numerical technique and therefore can be used to give confidence in the obtained solution using several methods, such as the Method of Moments (MoM) and the Finite-Difference Frequency-Domain (FDFD) method. Application of the ECS to the optimization of certain parameters for some numerical formulations, such as the Combined-Field Integral Equation (CFIE) is also presented.

Index Terms – CFIE, numerical error, radar cross-section.

I. INTRODUCTION

Numerical treatment of Maxwell's equations has steadily advanced for decades and a variety of computational methods have been devised to solve electromagnetic problems, especially problems involving scattering from arbitrarily shaped objects [1]-[4]. Such problems require using geometrical discretization methods to model the objects in a manner amenable to computers, followed by approximations of the equations associated with the used formulation and finally adopting a numerical routine to evaluate such approximate forms.

As yet, there have been quite a few works on the quantification of the error associated with the above procedure in computational electromagnetics [5]-[8]. Commercial software packages do not provide a confidence level to the user in the accuracy of the produced results. Verifying the boundary conditions (frequently used to guarantee that the solution satisfies them) typically uses the same operator equation, which has been approximated and thus suffers from complications related to singularities, mesh inaccuracy etc. and is specific to the adopted method.

This work proposes an error quantification approach, which is not only independent of the adopted numerical method but also visualizes the error by the so-called Error Cross-Section (ECS). In section II, the numerical error in solving a general electromagnetic scattering problem is discussed. In the same section, the definition of the ECS is presented and its relation to the Radar Cross-Section (RCS) of a thin conducting wire is investigated. Also, the correlation between the proposed error measure and the actual error is studied. In section III, the ECS is computed for various scattering problems using different numerical methods, such as the MoM and the FDFD, with an application to the optimization of the mixing factors in the MoM combined-field formulation. Conclusions and discussions are given in section IV.

II. PROBLEM FORMULATION

A. Residual error in scattering problems

Figure 1 shows an arbitrary object illuminated by a uniform plane wave. The total fields in the region enclosing the scatterer are given by:

Submitted On: December 3, 2013
Accepted On: April 5, 2014

$$\mathbf{E}^t = \mathbf{E}^i + \mathbf{E}^s, \tag{1}$$
$$\mathbf{H}^t = \mathbf{H}^i + \mathbf{H}^s. \tag{2}$$

Typically, the scattered fields are determined using a numerical technique for arbitrarily shaped objects. The inaccuracies associated with the adopted technique result in an error in the total fields, i.e.:

$$\delta\mathbf{E}^t = \mathbf{E}^t|_{num} - \mathbf{E}^t|_{exact}, \tag{3}$$
$$\delta\mathbf{H}^t = \mathbf{H}^t|_{num} - \mathbf{H}^t|_{exact}. \tag{4}$$

Estimation of the residual error $\delta\mathbf{E}^t$ and $\delta\mathbf{H}^t$ requires obtaining the exact solution $\mathbf{E}^t|_{exact}$ and $\mathbf{H}^t|_{exact}$, which is usually unknown for non canonical problems. Conventionally, numerical methods adopt certain convergence criteria to the solution by increasing the number of unknowns till the difference between the current and the previous solutions becomes acceptable. This, however, neither gives an indication about the error in the current solution with respect to the exact one, nor provides a physical insight into the quantified error. In this work, the goal is to define a new quantity, conveniently referred to as the Error Cross-Section (ECS), which is correlated with the actual residual error in a way that is independent of the adopted numerical technique. Unlike most error estimates [5]-[8], only few have a physical meaning like the Sobolev norm [9]. The ECS has this advantage and can be used to visualize the quantified error by comparing its definition to the RCS. Furthermore, the highest solution accuracy that can be achieved on a specific machine can be deduced by finding the lower limit of the ECS.

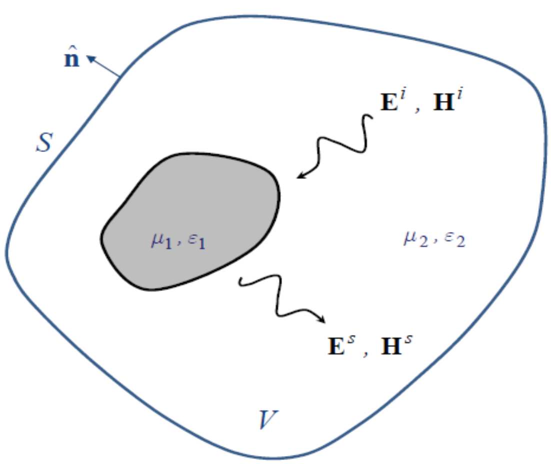

Fig. 1. Geometry of a general scattering problem.

B. Definition of the ECS

In electromagnetic scattering problems, the power conservation principle [10] requires that the total exiting power W^t must vanish if the media bounded by S were lossless, i.e.:

$$W^t = \frac{1}{2}\oiint_S \operatorname{Re}\left\{\mathbf{E}^t|_{exact} \times \mathbf{H}^{t^*}\big|_{exact}\right\} \cdot \hat{\boldsymbol{n}} dS = 0, \tag{5}$$

where $\hat{\boldsymbol{n}}$ is the outward normal to the surface S. Ideally, (5) should be satisfied; however, due to the errors in the scattered fields computation, the integral in (5) yields a residual value, viz.

$$W^t_{res} = \frac{1}{2}\oiint_S \operatorname{Re}\left\{\mathbf{E}^t|_{num} \times \mathbf{H}^{t^*}\big|_{num}\right\} \cdot \hat{\boldsymbol{n}} dS \neq 0. \tag{6}$$

Thus, the ECS is defined as follows:

$$\text{ECS} = \frac{W^t_{res}}{P_i|_{num}}, \tag{7}$$

where $P_i|_{num} = \frac{1}{2}\operatorname{Re}\left\{\mathbf{E}^i\big|_{num} \times \mathbf{H}^{i^*}\big|_{num}\right\}$ is the incident power density.

For 2-D problems, the Error Width (EW) is used instead of the more general term ECS and the integral in (6) is performed on a contour C rather than on a surface S. This is similar to using the scattering width in 2-D problems, instead of the radar cross-section used in 3-D problems.

A fundamental lower limit to the EW is attributed to the error in the numerical evaluation of (6) in the absence of the scatterer, i.e.:

$$\text{EW}^{min} = \frac{W^i_{res}}{P_i|_{num}}, \tag{8}$$

where $W^i_{res} = \frac{1}{2}\oint_C \operatorname{Re}\left\{\mathbf{E}^i\big|_{num} \times \mathbf{H}^{i^*}\big|_{num}\right\} \cdot d\mathbf{l} \neq 0.$

Although there could be different combinations of $\mathbf{E}^t|_{num}$ and $\mathbf{H}^t|_{num}$, which satisfy the power conservation principle, only one of them is correct in light of the uniqueness theorem [10]. Therefore, before finding the ECS, the boundary conditions should be verified to guarantee that the solution under consideration is actually the correct one. It is important to underline that the goal behind using any error estimate is not to decide whether the solution is correct or not, but to find out how accurate a correct solution is and to establish a confidence level in it. In light of this, error estimates can be employed for many purposes, i.e.: to minimize the computational effort using a specific numerical method by determining the optimum number of unknowns and to find the highest obtainable accuracy. Also, they can be used to compare the accuracy of different methods for a given problem and to provide a physical meaning for the error.

C. Physical meaning of the ECS

To visualize the quantified error and to have a feeling about how much this error is for a specific problem, the definition of the ECS is compared to the RCS or the scattering width (SW) in case of 2-D problems, which is defined as [10]:

$$\sigma_{2D} = \lim_{\rho\to\infty} 2\pi\rho \frac{|\mathbf{E}^s|^2}{|\mathbf{E}^i|^2}. \tag{9}$$

This can give an estimate of the error associated with the solution as a residual field $\delta\mathbf{E}^t$ and $\delta\mathbf{H}^t$, due to scattering from a fictitious thin wire, as compared to the original problem of scattering from the actual object. Figure 2 shows the SW of a thin conducting wire of radius a_w. The ordinate of Fig. 2 will be used to access the EW of the solution to determine the radius of the corresponding thin wire.

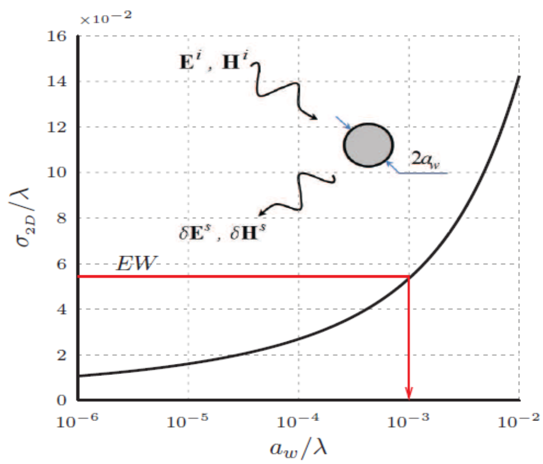

Fig. 2. Scattering width of a conducting wire with radius a_w normalized to the wavelength λ. The arrow shows how the figure is used to visualize the error width.

D. Correlation between the EW and the actual residual error

The correlation between the EW and the actual residual error $|\delta\mathbf{E}^t|$ for the problem of TM^z plane wave scattering from a 2-D circular PEC cylinder having a radius $a = \lambda/2$, is studied (see Fig. 3). In this example, the EFIE formulation of the moment method is adopted and the effect of varying the number of basis functions per wavelength (N_λ) is investigated. Invoking (6), the total exiting power is computed on a circular contour of radius $b = a + \lambda/4$. The exact solution $\mathbf{E}^t|_{exact}$ for this problem can be found analytically using [10]:

$$\mathbf{E}^t|_{exact} = -E_0 \sum_{n=-\infty}^{\infty} j^n \frac{J_n(k_0 a)}{H_n^{(2)}(k_0 a)} H_n^{(2)}(k_0 b) e^{jn\phi}, \tag{10}$$

where J_n and $H_n^{(2)}$ are the Bessel function of the first kind and the Hankel function of the second kind, respectively and k_0 is the free-space wavenumber. The residual error $|\delta\mathbf{E}^t|$ is computed by averaging its values on the circular contour C. Results as shown in Fig. 4, indicate that the EW and $|\delta\mathbf{E}^t|$ have the same asymptotic convergence rate.

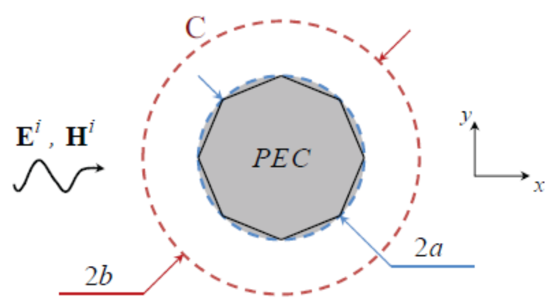

Fig. 3. TM^z plane wave scattering from a 2-D circular (approximated as an octagon) PEC cylinder.

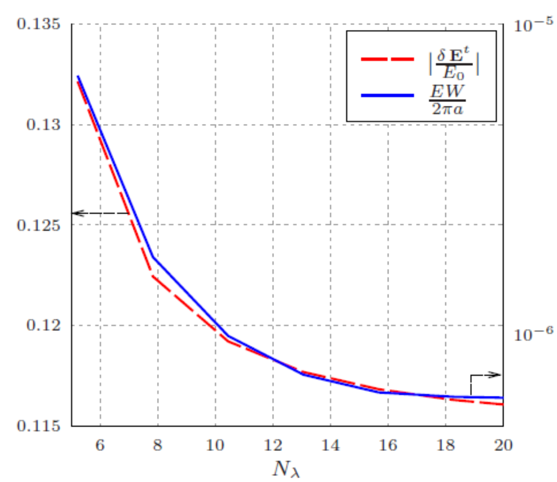

Fig. 4. Correlation between the EW and the actual residual error $|\delta\mathbf{E}^t|$ for the MoM solution of the problem shown in Fig. 3.

III. RESULTS

A. Method of moments

The proposed method is applied to selected numerical methods such as the MoM and the FDFD techniques. First, the example shown in Fig. 5 is considered to compare the EW for the problem of plane wave scattering from a 2-D PEC cylinder with equilateral triangular cross-section using different formulations. The scatterer is enclosed by a cylinder of radius $a = \lambda/2$. Figure 6 (a) shows the computed EW for the case of electric (EFIE) and magnetic field integral equation (MFIE) for TM^z illumination. It can be inferred from Fig. 6, that for this problem the EFIE has superior performance compared to the MFIE and that triangular basis functions give lower EW as compared to the pulses. Figure 6 (b) also shows that the EW is almost independent of b, for $b < b_{critical}$. This critical value depends on the accuracy of the numerical routine used to evaluate the integrals. Increasing this, accuracy results in a higher $b_{critical}$ and vice versa. To explain that, the scattered field intensity is noticed to be proportional to $1/b$ in 2-D problems and therefore the error in calculating $\mathbf{E}^s$ and $\mathbf{H}^s$ is also proportional to $1/b$. At the same time, when b increases, the integration contour C is enlarged with $2\pi(\Delta b)$ and the associated error increases with the same proportionality, provided that the accuracy is high enough. Therefore, the reduction in the error when calculating the scattered fields compensates the increase in the error due to the numerical evaluation of the integrals. This is true up to a critical value, $b_{critical}$ after which the error in evaluating the integrals, i.e.: EW^{min} is not linear anymore with b, as shown in Fig. 6 (c).

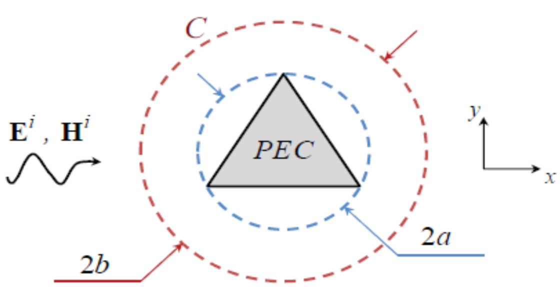

Fig. 5. TM^z plane wave scattering from a 2-D equilateral triangular PEC cylinder.

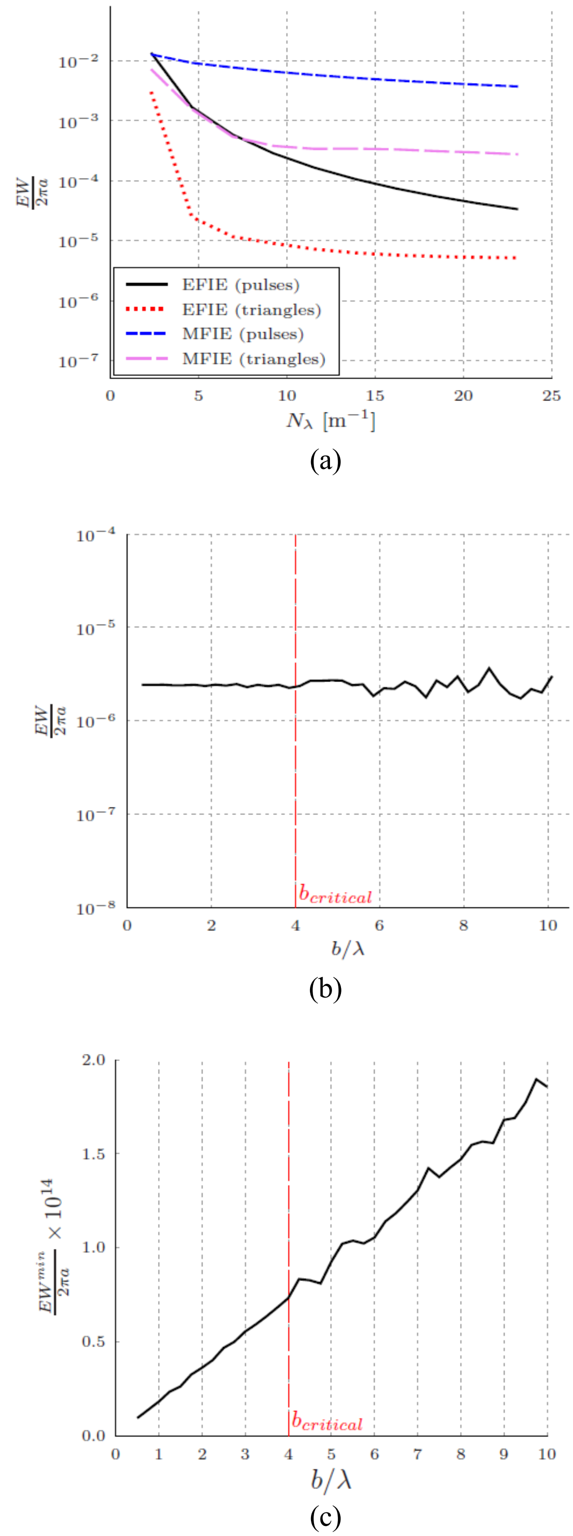

Fig. 6. (a) EW versus N_λ, (b) EW versus b and (c) EW^{min} for the MoM solution of the problem shown in Fig. 5.

An interesting observation regarding the MoM solution is that when the electrical size of the problem greatly increases, the number of unknowns increases likewise. There is a critical value for the number of unknowns at which the MoM matrix becomes ill-conditioned and the error in finding its inverse affects the overall accuracy. This critical value can be determined using the EW. To manifest this phenomenon, the example of Fig. 3 is considered again but the radius of the PEC cylinder is now made electrically huge, i.e.: $a = 5\lambda \gg \lambda$. Using the MoM-EFIE formulation, $N_\lambda|_{critical}$ and the corresponding $\mathrm{EW}_{critical}$ are shown in Fig. 7. Based on the EW/SW analogy and referring to Fig. 2, the thin wire radius corresponding to the error at $N_\lambda|_{critical}$ is 1000.

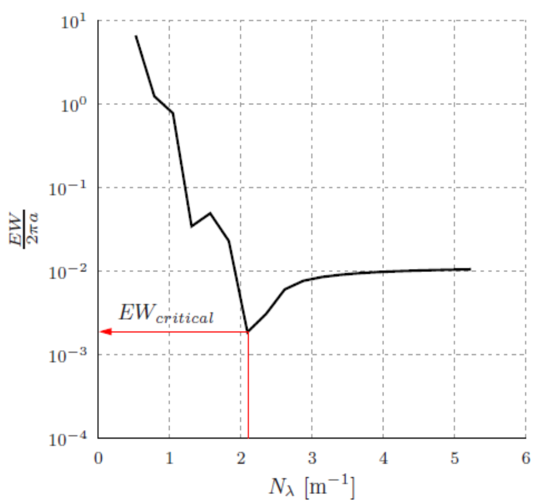

Fig. 7. The error width of the MoM solution using EFIE formulation for the problem shown in Fig. 3.

B. Finite-difference frequency-domain

Considering another numerical method, the error in the FDFD solution of plane wave scattering from a 2-D rectangular dielectric cylinder with a side length l and a dielectric constant ε is investigated. Due to the rectangular grid employed by the FDFD in defining the geometry and field points, it is more convenient for the integration contour to be rectangular with a side length L, as shown in Fig. 8. For $l = 2\lambda$, $L = 4\lambda$ and $\varepsilon = 4$, the EW is depicted in Fig. 9.

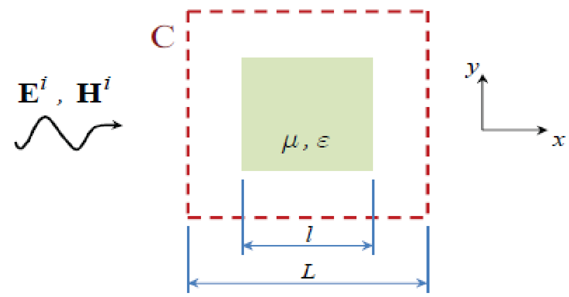

Fig. 8. Plane wave scattering from a 2-D rectangular PEC cylinder.

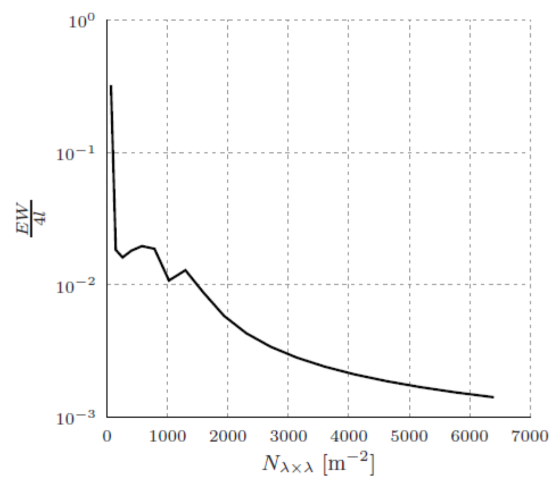

Fig. 9. The error width of the FDFD solution for the problem shown in Fig. 8 under TM^z illumination.

C. Optimization of the mixing factors in the MoM-CFIE

An interesting application to the proposed error estimate is to determine the best choice of the mixing factors used in the CFIE, commonly adopted in the MoM solution to remedy the internal resonance problem. The CFIE formulation is typically obtained as a weighted sum of the EFIE and MFIE with orthogonal weights [11], i.e.:

$$\mathrm{CFIE} = \frac{\beta}{\eta_0}\mathrm{EFIE} + \alpha\ \mathrm{MFIE}, \tag{11}$$

where CFIE, EFIE and MFIE are either the matrix of unknowns or the excitation vector and η_0 is the intrinsic impedance of free-space. In [12], the choice of the factors α and β was random. The EW concept can be employed to study the effect of this choice on the solution accuracy.

This is done by determining the combination that results in a minimum EW at each number of unknowns. In light of this, it was found that having a 90° phase difference between the mixing factors and keeping α constant for the given problem, the value of β is a very sensitive function of N_λ, i.e.:

$$\mathrm{CFIE} = \frac{\beta(N_\lambda)}{\eta_0}\mathrm{EFIE} + j\alpha\,\mathrm{MFIE}. \tag{12}$$

The example in Fig. 5 is investigated again using the proposed formula in (12) and pulse basis functions. The variation of the EW with β for different values of N_λ, is shown in Fig. 10. Results manifest that for each N_λ there exists a certain value of β, which results in a minimum EW; hence, leads to a significant improvement in the solution accuracy compared to the EFIE or MFIE formulations.

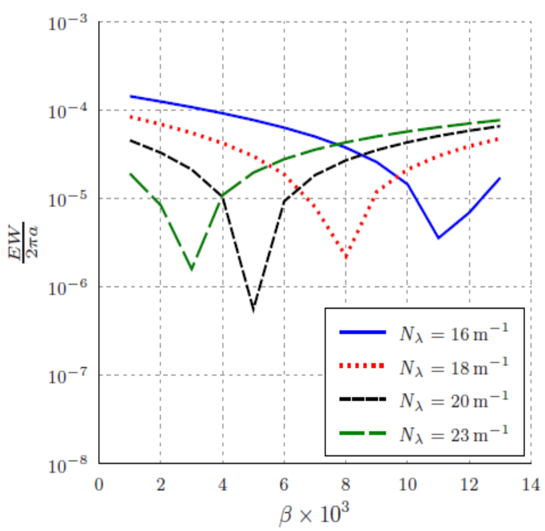

Fig. 10. MoM-CFIE solution using the formula in (12) for the scatterer shown in Fig. 5. The error width is plotted versus β coefficient for different values of N_λ.

IV. CONCLUSION

A general method based on power conservation and independent of the adopted technique is proposed to quantify the error. The definition of the ECS is introduced to compare the solution accuracy for different numerical techniques. For 2-D problems, the EW is used instead of the more general term ECS. The proposed method is applied to the MoM and FDFD solutions of plane wave scattering from 2-D objects. This approach can also be applied to 3-D objects in a straightforward manner. A comparison between the ECS and the RCS of a thin wire for 2-D problems or small sphere for 3-D problems is introduced to visualize the amount of error. An interesting application for the proposed ECS method is finding the critical value for the matrix size in MoM solution after which the accuracy starts to degrade. Another application is to estimate the accuracy of different formulations, as illustrated with the CFIE and to optimize the choice of the mixing factors. Moreover, incorporating the proposed method with the results obtained using commercial software packages as a post-processing step, is on-going with the goal of providing a unified benchmark for the error of these packages.

REFERENCES

[1] J. Liu and J. M. Jin, “A special higher order finite-element method for scattering by deep cavities,” *IEEE Transactions on Antennas and Propagation*, vol. 48, no. 5, pp. 694-703, 2000.

[2] R. Luebbers, D. Steich and K. Kunz, “FDTD calculation of scattering from frequency-dependent materials,” *IEEE Transactions on Antennas and Propagation*, vol. 41, no. 9, pp. 1249-1257, 1993.

[3] E. Lucente, A. Monorchio and R. Mittra, “An iteration-free MoM approach based on excitation independent characteristic basis functions for solving large multiscale electromagnetic scattering problems,” *IEEE Transactions on Antennas and Propagation*, vol. 56, no. 4, pp. 999-1007, 2008.

[4] J. M. Jin and V. V. Liepa, “Application of hybrid finite element method to electromagnetic scattering from coated cylinders,” *IEEE Transactions on Antennas and Propagation*, vol. 36, no. 1, pp. 50-54, 1988.

[5] C. P. Davis and K. F. Warnick, “Error analysis of 2-D MoM for MFIE/EFIE/CFIE based on the circular cylinder,” *IEEE Transactions on Antennas and Propagation*, vol. 53, no. 1, pp. 321-331, 2005.

[6] G. C. Hsiao and R. E. Kleinman, “Mathematical foundations for error estimation in numerical solutions of integral equations in electromagnetics,” *IEEE Transactions on Antennas and Propagation*, vol. 45, no. 3, pp. 316-328, 1997.

[7] F. Wei, J. W. Massey, C. S. Geyik and A. E. Yilmaz, “Error measures for comparing bioelectromagnetic simulators,” *Antennas and Propagation Society International Symposium (APSURSI)*, IEEE, pp. 1-2, 2012.

[8] K. F. Warnick and W. C. Chew, "Error analysis of the moment method," *Antennas and Propagation Magazine*, IEEE, vol. 46, no. 6, pp. 38-53, 2004.
[9] C. P. DAVIS and K. F. Warnick, "The physical meaning of the Sobolev norm in error estimation," *National Radio Science Meeting*, pp. 3377-3380, 2004.
[10] C. A. Balanis and J. Wiley, "Advanced engineering electromagnetics," *Wiley Online Library*, vol. 111, 2012.
[11] W. C. Chew, E. Michielssen, J. Song and J. Jin, "Fast and efficient algorithms in computational electromagnetics," *Artech House, Inc*., 2001.
[12] J. R. Mautz and R. F. Harrington, "H-field, e-field, and combined-field solutions for conducting bodies of revolution," *Archiv Elektronik und Uebertragungstechnik*, vol. 32, pp. 157-164, 1978.

Ahmed M. Kord was born in Damietta, Egypt, in 1990. He received his B.Sc. and M.Sc. degrees in Electronics and Telecommunications Engineering from Cairo University, Cairo, Egypt in 2011 and 2014, respectively. Since 2012, he has been a Teaching Assistant with the Department of Electronics and Telecommunications Engineering, Cairo University, where he is currently teaching undergraduate courses. His research interests include metamaterials, computational electromagnetics, microwave devices and circuits.

Islam A. Eshrah received his B.Sc. and M.Sc. degrees in Electronics and Communications Engineering from Cairo University, Cairo, Egypt in 2000 and 2002, respectively. He received his Ph.D. degree in Electrical Engineering from the University of Mississippi, USA in 2005. From 2000 to 2002, he was a Teaching Assistant in the Department of Electronics and Communications Engineering at Cairo University. From 2002 to 2006, he worked as a Research Assistant then as a visiting scholar at the Department of Electrical Engineering, at the University of Mississippi. From 2007 to 2012 he was an Assistant Professor with the Department of Electronics and Communications Engineering. Since 2012, he has been an Associate Professor at the same department, where he is currently teaching graduate and undergraduate courses. He has more than 20 refereed journal publications and more than 50 publications in national and international conferences. Eshrah is also a co-author of the *Metamaterial Handbook*. His research interests include dielectric resonator and wire antennas, numerical methods in electromagnetics, modeling of microwave structures, smart antenna arrays and metamaterial guided-wave structures.

FPO-Based Shooting and Bouncing Ray Method for Wide-Band RCS Prediction

Y. An, Z. Fan, D. Ding, and R. Chen

Department of Communication Engineering
Nanjing University of Science and Technology, Nanjing, 210094, China
eechenrs@njust.edu.cn

Abstract **─** The fast physical optics (FPO) method for calculating the monostatic radar cross section (RCS) of an object over a range of frequencies is extended to the shooting and bouncing rays (SBR) method where the multi-bounce phenomena of the launched rays is considered. The FPO method is an improved version of the physical optics (PO) method, which is efficient when calculating the monostatic RCS over a wide range of frequencies or/and angles. The SBR method, based on the combination of geometrical optics (GO) and PO methods, can reach a higher accuracy compared with the PO method. However, due to different length of ray tube paths, it is difficult to implement the phase compensation and phase retrieval in the SBR as that in the FPO method. In this paper, a coordinate transformation is introduced in the integral equation, which transforms the original ray tubes model into a new one. The FPO technique can then be taken on the revised model without difficulty. The validity and efficiency of the proposed method are validated though a couple of numerical experiments.

Index Terms - Coordinate transformation, electromagnetic scattering, fast physical optics (FPO), shooting and bouncing rays (SBR), and wide-band RCS.

I. INTRODUCTION

The radar cross section (RCS) is an important characterization of the electromagnetic scattering properties of large objects and it is common practice to use this data in the fields of war monitoring, radar imaging simulation, and target identification. Techniques for computing RCS can be categorized into high-frequency techniques and low-frequency techniques [1]. The low-frequency techniques include the method of moments (MoM) [2], the finite element method (FEM) [3] and other MoM-type methods [4-10]. The high-frequency techniques include the geometrical optics (GO) and physical optics (PO) [11] methods, and more complicated methods, such as ILDCs [12], GO/UTD-PO/PTD [13], and SBR [14]. The high-frequency techniques, usually based on the ray-tracing and edge diffraction, are fast and accuracy acceptable when used to electrically large objects [15]. For example, an aircraft at *L* wave band will up to 130 wavelengths, which will result a large number of unknowns if 0.1 wavelength mesh size is used in the MoM method. This large number of unknowns puts forward high demanding in computer performance. However, the high-frequency techniques express the scattering field in an analytical approach and avoid solving the matrix equations as that in the low-frequency techniques, which reduces the memory and CPU time cost significantly.

A lot of researchers have paid attention to the calculation of wide-band RCS of an object. The asymptotic waveform evaluation (AWE) [16-18] technique and model-based parameter estimation (MBPE) [19] have been developed to decrease the computation burden associated with repeated point-by-point calculations [18]. However, the techniques mentioned above are based on low-frequency techniques, and the objects analyzed are not electrically large. Recently, a fast physical optics (FPO) [20-25] has been developed to fast evaluate wide-band or/and wide-angle monostatic RCS. The algorithm is based on the observation that the scattering pattern of a finite scatterer is an

Submitted On: January 23, 2013
Accepted On: March 8, 2014

essentially band limited function of the aspect angles and frequencies [20, 26]. In the FPO method, the rapid oscillation of the integrand is cancelled by a phase compensation process, the RCS response over a range of frequencies or angles can then be obtained by interpolating the phase-compensated field at much sparser sampling grids. The backscattering echo of a 2-dimensional rectangular cylinder [20] and double-bounce scattering phenomena involving two surfaces [21] have been analyzed by the FPO. However, the method is rather complicated and limited to double-bounce scattering phenomena.

The shooting and bouncing rays (SBR) [14], proposed by H. Ling etc., is a robust and an accurate method in analyzing electrically large objects. In the SBR approach rays representing the incident fields in a GO manner are used to determine the resulting equivalent surface currents and finally the resulting field contributions at the given observation points are derived by PO integration [27]. Besides the first-order scattered fields, the SBR provides more accurate results by including the scattered fields arising from multiple bounces [29]. In [29], a GPU-based SBR that implemented on the graphics processing unit (GPU) is proposed to reduce the computation time. The ray tracing is modified to evaluate the exit point and field quickly. The electromagnetic computing is integrated into the process of central ray tracing, including the evaluation of the reflected and scattered field. The main contribution of this paper is utilizing the GPU to accelerate both ray tracing and electromagnetic computing of the SBR, which is a parallelization of the SBR method under a certain frequency and incident angle. The wide-band and wide-angle monostatic RCS can then be obtained by repeating this process at different frequencies and angles. Whereas the method proposed in [20] is focused on getting wide-band or/and wide-angle monostatic RCS with interpolation technique. According to this method, only a few monostatic RCS need to be calculated directly, the RCS at required frequencies and angles can then be obtained by interpolating these calculated ones.

In this paper, the FPO method for calculating the monostatic RCS of an object over a range of frequencies is extended to the SBR method. Unlike the method in [29], the method proposed in this paper tries to get wide-band RCS by interpolating values calculated at sampling frequencies. The RCS at these sampling frequencies can be obtained by either a CPU-based or a GPU-based SBR method as that in [29]. However, due to different length of ray tube paths, it is difficult to implement the phase compensation and phase retrieval in the SBR as that in the FPO method. To conquer this problem, a coordinate transformation is introduced in the integral equation, which transforms the original ray tubes model into a new one. The FPO technique can then be taken on the revised model. The remainder of this paper is organized as follows. In section II, theory and formulations are discussed. Numerical results are presented and discussed in section III. Section IV concludes this paper. The time factor $e^{j\omega t}$ is assumed and suppressed throughout this paper.

II. THEORY AND FORMULATION

Consider a perfectly electrically conductor (PEC) shown in Fig. 1, a plane wave is incident on this object ($\vec{E}_{in}$ and $\vec{H}_{in}$ denote the electric and magnetic field of the incident wave, respectively). Ro is half of the diagonal line of the cube that contains the object. To facilitate analysis, the object is meshed with small patches (for example, triangular patches), the number of meshed triangles of which is dependent on the frequency and the size of the object. In section A below, the theory of the FPO is briefly discussed. The SBR and its improvement are discussed in section B.

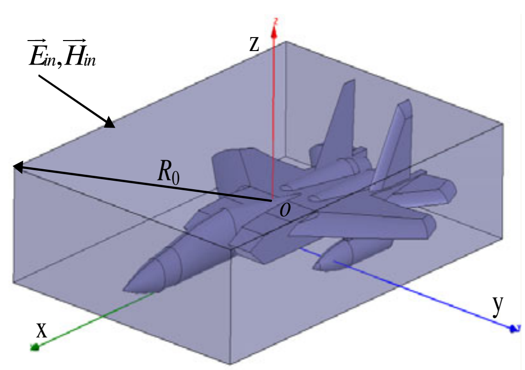

Fig. 1. Scattering model of an object.

A. FPO

As shown in Fig. 1, according to the PO method, the back-scattered field of the object at a fixed frequency can be written as,

$$\vec{E}_s(f) = 2jk\eta\frac{e^{-jkR}}{4\pi R}\sum_{i=1}^{N_t}\int_{s_i}\hat{s}\times[\hat{s}\times(\hat{n}\times\vec{H}_{in})]\cdot e^{2jk\hat{s}\cdot\vec{r}'}ds' \quad (1)$$
$$= 2jk\eta\frac{e^{-jkR}}{4\pi R}\sum_{i=1}^{N_t}\int_{s_i}p\cdot e^{2jk\hat{s}\cdot\vec{r}'}ds',$$

where $\hat{n}$ is a unit outward normal vector at the point $\vec{r}'$, $\hat{s}$ is the unit vector in the direction of observation. k is the wavenumber, η is the intrinsic wave impedance, N_t is the number of triangle patches in the illuminative area, R is the distance between the observation point and the object, and $j=\sqrt{-1}$. In the high frequency region, k is a large number, and function p is a slowly varying function regarding frequencies. In this paper, the integral technique proposed by Gordon [30] is adopted to calculate the integral in equation (1).

When used to wide-band scattering problems (for example, the required frequency band is $[f_{\min}, f_{\max}]$ with frequency interval Δf), one has to repeat the calculation of equation (1) at a sequence of frequency samples, which is time-consuming when used to electrically large object. According to the Nyquist sampling theorem, the sampling interval of the frequency should satisfy $\Delta f' < c/(4R_o)$, where c is the velocity of light. Consequently, the number of frequency samples is,

$$N_f = \Omega_f 4R_o(f_{\max} - f_{\min})/c, \quad (2)$$

where Ω_f is the oversampling ratio satisfying $\Omega_f > 1$. It is observed that the number of frequency samples is proportional to the size of the object R_o. One possible way to reduce the N_f is by dividing the object into several non-overlapped groups as shown in Fig. 2. The N_f^i of the i-th group is obtained by substituting R_o with R_o^i in equation (2). Since $R_o^i < R_o$, the sampling points $N_f^i < N_f$. The back-scattered field of each group at the required frequencies can then be interpolated by these sparser sampling grids. However, the scattered field obtained by direct interpolation is not accurate. To improve the interpolation accuracy, phase compensation is applied to the back-scattered field prior to interpolation, and a phase retrieval algorithm is used after the interpolation stage. The phase compensated field of the n-th group can be written as,

$$\tilde{\vec{E}}_s^n(f) = 2jk\eta\frac{e^{-jkR}}{4\pi R}\sum_{i=1}^{N_t^n}\int_{s_i}p\cdot e^{2jk\hat{s}\cdot(\vec{r}'-\vec{r}_c^n)}ds', \quad (3)$$

where N_t^n is the number of triangle patches in the illuminative area of the n-th group, $\vec{r}_c^n$ is the center coordinate of the n-th group. The rapid oscillation of the integrand is cancelled by the phase compensation process, which makes the interpolation process more accurate. After interpolation, the back-scattered field of each group at the required frequency point can be retrieved by phase restoration, i.e.,

$$\vec{E}_s^n(f) = \tilde{\vec{E}}_s^n(f)e^{2jk\hat{s}\cdot\vec{r}_c^n}. \quad (4)$$

The total back-scattered field $\vec{E}_s(f)$ can then be obtained by aggregation of the back-scattered field of all groups and the monostatic RCS can then be written as,

$$RCS(f) = \lim_{R\to\infty}4\pi R^2\frac{|\vec{E}_s(f)|^2}{|\vec{E}_{in}(f)|^2}. \quad (5)$$

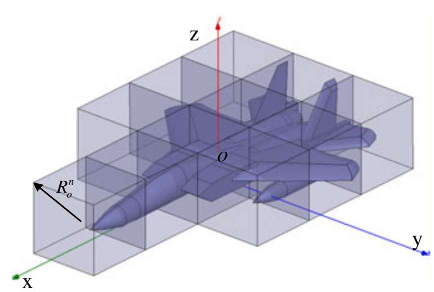

Fig. 2. Schematic drawing of partitioning of the object.

B. SBR and its improvement

The SBR method involves two steps: ray tube tracing and electromagnetic computing at the exit point. First, the incident plane wave is modeled as a dense grid of ray tubes at a virtual aperture, which are shot toward the object. When used to wide-band RCS prediction, the number of ray tubes is set according to the highest frequency to be analyzed. Each ray tube is recursively traced to obtain the exit position and its scattered field. Figure 3 shows a possible path of a ray tracing. It should be noted that the ray tracing process is time-consuming when the object is meshed with large number of triangles and when the number of ray tubes is large. In [28], the angular Z-buffer (AZB), the volumetric space partitioning (SVP) and the depth-limited search method are combined to accelerate the ray tracing process, whereas a stackless kd-tree traversal algorithm is adopted to evaluate the exit position and field quickly in [29]. In this paper, the octree [31-32] technique is used to recursively subdividing the box into eight children to decrease the number of intersection tests. Second, the PO integral is preformed to obtain the scattered field of this ray tube based on the pre-calculated exit positions and field [29]. The scattered field of the object can be written as,

$$\vec{E}_s(f) = jk\eta \frac{e^{jkR}}{4\pi R} \sum_{i=1}^{N_r} \int_{s_i} \hat{s} \times [\hat{s} \times (\hat{n} \times \vec{H}_i) e^{-jkr_i}] e^{jk\hat{s}\cdot\vec{r}\,'} ds', \tag{6}$$

where N_r is the number of ray tubes, $\vec{H}_i$ is the magnetic field of the *i*-th ray tube at the exit point, and r_i is the length of the path of the *i*-th ray tube. It can be seen from equations (6) and (1) that both of the two equations have the same format except for the exponential term e^{-jkr_i}. However, due to different length of ray tube paths r_i, it is difficult to implement the phase compensation and phase retrieval in the SBR as that in the FPO method. Furthermore, as mentioned in section II A, that the phase compensation and phase retrieval is applied group by group, not ray by ray. Consequently, the FPO technique can not be used into SBR directly.

We rewrite the exponential terms in equation (6) as,

$$e^{-jkr_i} e^{jk\hat{s}\cdot\vec{r}\,'} = e^{-jk\hat{s}\cdot\vec{r}_i\,'} e^{jk\hat{s}\cdot\vec{r}\,'} = e^{jk\hat{s}\cdot(\vec{r}\,' - \vec{r}_i\,')}, \tag{7}$$

where $k\hat{s}\cdot\vec{r}_i\,' = kr_i' \cos\alpha$, with α as the angle between $\hat{s}$ and $\vec{r}_i\,'$. In principle, there are various $\vec{r}_i\,'$ that satisfy this condition. In this paper, we choose $\vec{r}_i\,'$ as the direction of $\hat{s}$ as shown in Fig. 3, which leads to $\alpha = 0^0$ and $|\vec{r}_i\,'| = r_i$. Substituting equation (7) into equation (6) we can arrive at,

$$\vec{E}_s(f) = jk\eta \frac{e^{jkR}}{4\pi R} \sum_{i=1}^{N_r} \int_{s_i} \hat{s} \times [\hat{s} \times (\hat{n} \times \vec{H}_i)] e^{jk\hat{s}\cdot(\vec{r}\,' - \vec{r}_i\,')} ds'. \tag{8}$$

Let $\vec{r}\,'' = \vec{r}\,' - \vec{r}_i\,'$ and substitute it into equation (8) we finally get,

$$\vec{E}_s(f) = jk\eta \frac{e^{jkR}}{4\pi R} \sum_{i=1}^{N_r} \int_{s_i} \hat{s} \times [\hat{s} \times (\hat{n} \times \vec{H}_i)] e^{jk\hat{s}\cdot\vec{r}\,''} ds''. \tag{9}$$

The equation $\vec{r}\,'' = \vec{r}\,' - \vec{r}_i\,'$ implies that the final integral can be taken on a new model that moves the exit points in the reverse direction of $\hat{s}$. Comparison between equations (6) and (9) shows that the coordinate transformation extracts the exponential term in the square brackets and combines with the exponential term outside the square brackets. As shown in Fig. 3, the original integral of equation (6) at the exit point (Point C) can be replaced by the integral of equation (9) at point D. In other words, the new model (or integral domain) has taken into account the effect of path of each ray tube, whereas the original integral is taken at the exit point. However, the coordinate transformation does not affect the fields and the medium through the transformation because equation (9) is consistent with equation (6) in essence and there is only a change in variables. To make this clearer, we consider a dihedral corner reflector as shown in Fig. 4 (a), the incident and observation angles are $\theta_i = 45^0$, $\varphi_i = 0^0$, $\theta_s = 45^0$, $\varphi_s = 0^0$. After ray tracing and coordinate transformation, the integral of equation (9) is taking on a new model as shown in Fig. 4 (b). Then the new model can be regrouped without difficulty and take the FPO technique as in section II A to fast get the wide-band RCS prediction.

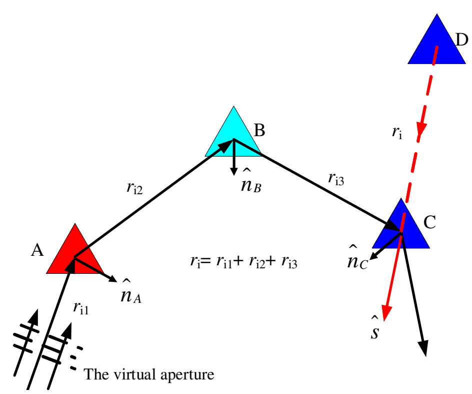

Fig. 3. Schematic drawing of the path of a ray tube.

Points A, B, and C are intersection points during the ray tracing. Point D is obtained by moving point C in the reverse direction of $\hat{s}$ such that the distance between C and D (remarked as r_i) satisfies $r_i = r_{i1} + r_{i2} + r_{i3}$.

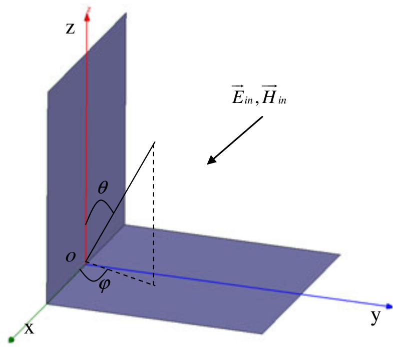

(a)

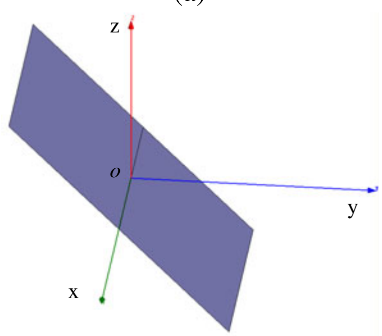

(b)

Fig. 4. Schematic drawing of scattering model of a dihedral corner reflector; (a) the dihedral corner reflector and (b) the new model after ray tracing and coordinate transformation.

III. NUMERICAL RESULTS

In this section, the approach and its efficiency are validated through a couple of numerical experiments. The program is implemented on a personal computer with Intel Dual-core CPU. The CPU and memory sizes are 2.99 GHz and 3.24 GB, respectively. In all examples below, the 4-point Lagrange interpolation technique is used in the FPO with evenly distributed sampling points. As mentioned above, the octree grouping technique is used to accelerate the ray tracing process in the SBR and regrouping is needed on the new model after the ray tracing process. Let l_1 denote the finest group size of the former while l_2 denote the group size of the latter step.

Firstly, we consider a trihedral corner reflector with a side length of 1m, the geometry of the trihedral corner reflector is shown in Fig. 5. The monostatic RCS on the $\theta = 60^0$ plane is calculated. The virtual aperture is also meshed with 0.01λ as that in [29]. The results of the HH-polarization at 3 GHz are shown in Fig. 6, which show a good agreement between the method proposed in this paper and the method in [29]. The total computation time of the proposed method in this paper is about 281 seconds, whereas the GPU-based method in [29] only needs 8.73 seconds. The reason is that the method introduced in this paper mainly deals with wide-band RCS prediction. The result may become unacceptable when used to wide-angle problems because of the drastic change in the path of each ray tube at different angles. So the proposed method in Fig. 6 degenerates to the conventional SBR indeed. However, as mentioned in the introduction, the GPU-based SBR method in [29] can be combined together with the method proposed in this paper to accelerate the computation at sampling frequencies when dealing with wide-band RCS problems.

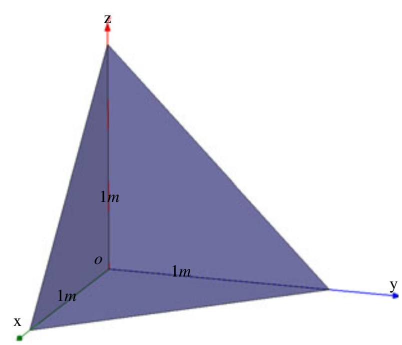

Fig. 5. The geometry of a trihedral corner reflector.

Secondly, we validate accuracy of the proposed method. As shown in Fig. 7, we consider a trihedral corner reflector with a side length of 10 meters. The number of ray tubes is set to be 68,730. The incident angles are $\theta_i = 45^0$, $\varphi_i = 45^0$, respectively. $l_1 = l_2 = 0.4m$. The frequency range of interest is 0.5 GHz − 1.5 GHz, with frequency interval Δf =20 MHz (resulting 51 frequencies points). By using equation (2) with $\Omega_f = 2$ and

$R_o = \sqrt{3} l_2 / 2$, only 10 frequencies points are needed to be calculated. Figure 8 is the monostatic RCS for VV polarization versus the frequency. The result simulated by the commercial software CST [33] is also shown in the figure, which shows a good agreement among these methods.

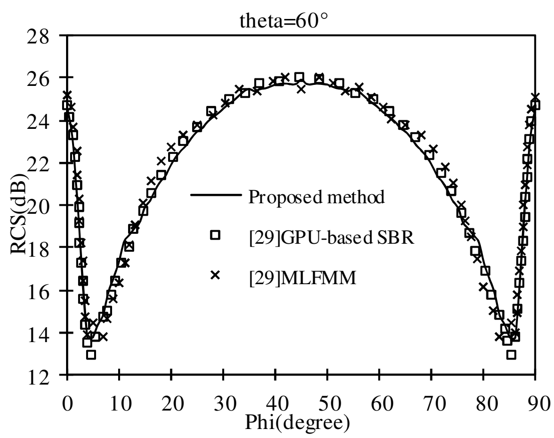

Fig. 6. Comparison of our proposed method and the method in [29] for the trihedral corner reflector.

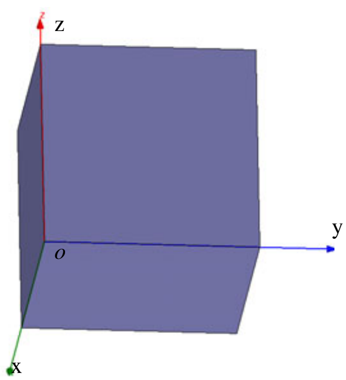

Fig. 7. The geometry of a trihedral corner reflector.

Thirdly, we consider an F15 aircraft as shown in Fig. 1, the size of the F15 aircraft is $4.78m \times 3.35m \times 1.06m$. The incident angles are $\theta_i = 120^0$, $\varphi_i = 0^0$, respectively. The frequency range of interest is 1 GHz – 15 GHz, with frequency interval Δf = 20 MHz (resulting 701 frequencies points and 627,592 ray tubes). $l_1 = l_2 = 0.1m$. Figure 9 is the monostatic RCS for VV polarization versus the frequency with different oversampling rates of the proposed method, which shows a good agreement with the direct SBR method. Table I lists the CPU time and relative error of the proposed method, where the CPU time cost by the ray tracing is not considered (Because the CPU time for the ray tracing are the same for all of the 4 cases). The relative error is given by,

$$relative\ error = \frac{\sum_{i=1}^{frequency\ points} |RCS_{omega} - RCS_{SBR}|_i}{\sum_{i=1}^{frequency\ points} |RCS_{SBR}|_i}, \tag{10}$$

where the RCS calculated by the SBR method is used as the correct solution. It can be seen from the table that the proposed method can reduce the CPU time significantly with reasonable oversampling rates, and the relative error decreases with the oversampling rate increases.

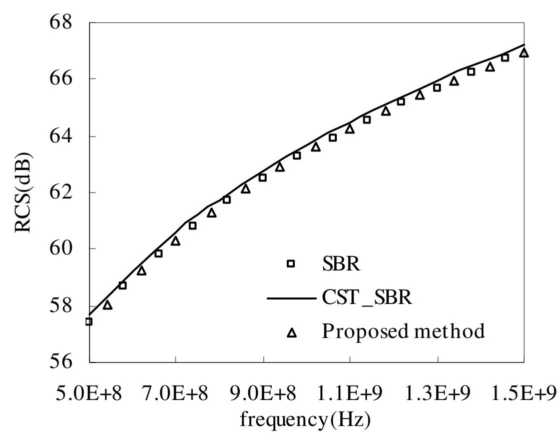

Fig. 8. Monostatic RCS of the trihedral corner reflector versus the frequency computed by the proposed method, the direct SBR method, and commercial software CST. The SBR technique in CST is adopted in the simulation.

Table I: CPU time cost and relative error for different oversampling rates.

	Ω_f	No. of frequency points	CPU time (Sec.)	relative error
SBR	——	701	433	——
Proposed method	$\Omega_f = 2$	34	18	5.6%
	$\Omega_f = 3$	50	26	4.7%
	$\Omega_f = 4$	68	35	4.4%

Finally, we consider a tank model as shown in Fig. 10. The size of the tank is $8.11m \times 2.59m \times 1.82m$. 690,454 ray tubes is used to get an accurate result over the C, X, and

Ku wave band (i.e., 4 GHz – 18 GHz). The frequency interval of interest is Δf =10 MHz. The incident angles are $\theta_i = 60^0$, $\varphi_i = 0^0$. $l_1 = l_2 = 0.1m$ is adopted as that in the third example. Figure 11 shows the monostatic RCS versus the frequency with different oversampling rates of the proposed method, which shows a good agreement with the conventional SBR method. Table II lists the CPU time and error values of the proposed method, from which we can see that the proposed method can reduce the CPU time with a factor of 26 ~44 without losing accuracy compared with the conventional SBR. In terms of relative error, the error values in Table I are higher than those in Table II. The reason is that the monostatic RCS in Fig. 9 is much smaller than that in Fig. 11. The error values can be reduced by a double precision or higher order interpolation technique.

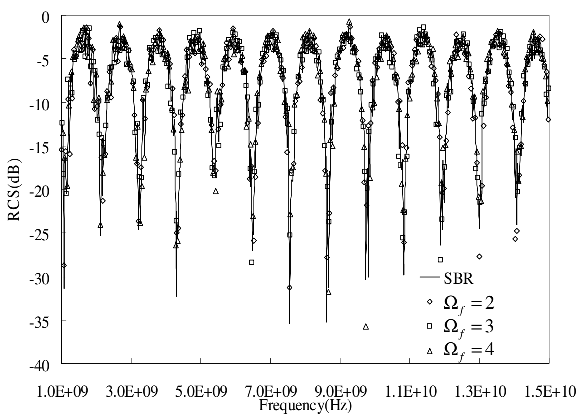

Fig. 9. Monostatic RCS versus frequency computed by the proposed method with different oversampling rates and the SBR method.

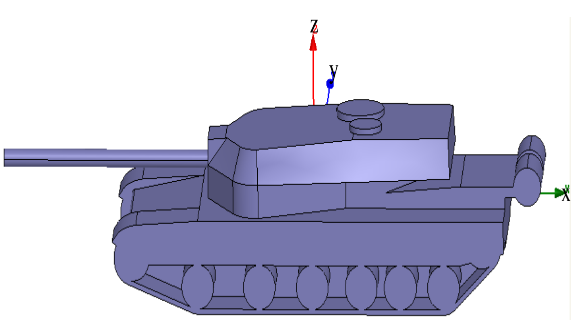

Fig. 10. The geometry of a tank model.

Table II: CPU time cost and relative error for different oversampling rates.

	Ω_f	No. of frequency points	CPU time (Sec.)	relative error
SBR	——	1401	711	——
Proposed method	$\Omega_f=2$	33	16	0.0972%
	$\Omega_f=3$	49	22	0.0867%
	$\Omega_f=4$	65	27	0.0865%

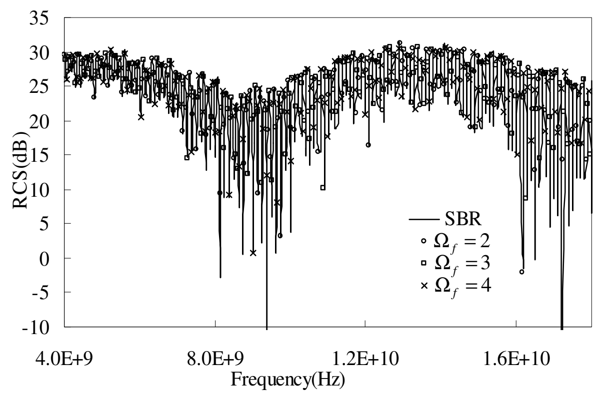

Fig. 11. Monostatic RCS versus frequency computed by the proposed method with different oversampling rates and the SBR method.

IV. CONCLUSION

In this paper, the FPO method for calculating monostatic RCS of an object over a range of frequencies is extended to the SBR method where the multi-bounce phenomena of the launched rays are considered. A coordinate transformation is used to cancel the influence of different length of ray tubes on phase compensation and phase retrieval, which transforms the original integral model into a new one. The FPO technique can then be taken on the revised model without difficulty. The proposed method and its efficiency are validated by numerical experiments, which show that the proposed method can reduce the CPU time significantly. The proposed method is especially suited for generation of synthetic data for radar imaging simulation.

ACKNOWLEDGMENT

This work is partially supported by Natural Science Foundation of 61271076, 61171041, 61371037, Jiangsu Natural Science Foundation of BK2012034, and Ph.D. Programs Foundation of

Ministry of Education of China of 20123219110018. The author would like to thank the reviewers for their comments and suggestions.

REFERENCES

[1] J. Jin, S. Ni, and S. Lee, "Hybridization of SBR and FEM for scattering by large bodies with cracks and cavities," *IEEE Trans. Antennas Propag.*, vol. 43, no. 10, pp.1130-1139, 1995.

[2] R. Harrington, *Field Computation By Moment Methods*, Macmillan, New York, 1968.

[3] J. Jin, *The Finite Element Method In Electromagnetics*, Wiley, New York, 1993.

[4] W. Chew, J. Jin, E. Michielssen, and J. Song, *Fast And Efficient Algorithms In Computational Electromagnetics*, Artech House, Boston, 2001.

[5] E. Michielssen and A. Boag, "A multilevel matrix decomposition algorithm for analyzing scattering from large structures," *IEEE Trans. Antennas Propag.*, vol. 44, no. 8, pp.1086-1093, 1996.

[6] L. Tsang and Q. Li, "Wave scattering with UV multilevel partitioning method for volume scattering by discrete scatters," *Microw. Opt. Technol. Lett.*, vol. 41, no. 5, pp. 354-361, 2004.

[7] E. Bleszynski, M. Bleszynski, and T. Jaroszewicz, "AIM: Adaptive integral method for solving large-scale electromagnetic scattering and radiation problems," *Radio Sci.*, vol. 31, pp. 1225-1251, 1996.

[8] Z. Liu, R. Chen, J. Chen, and Z. Fan, "Using adaptive cross approximation for efficient calculation of monostatic scattering with multiple incident angles," *Applied Computational Electromagnetics Society (ACES) Journal*, vol. 26, no. 4, pp. 325-333, 2011.

[9] H. Fangjing, N. Zaiping, and H. Jun, "An efficient parallel multilevel fast multipole algorithm for large-scale scattering problems," *Applied Computational Electromagnetics Society (ACES) Journal*, vol. 25, no. 4, pp. 381-387, 2010.

[10] M. Pavlovic, B. Mrdakovic, D. Sumic, and B. Kolundzija, "Simulating large RCS problems with MLFMM applied to higher order basis functions implemented in WIPL-D Pro," *25th Annual Review of Progress in Applied Computational Electromagnetics (ACES)*, Monterey, California, pp. 559-564, March, 2009.

[11] A. Raju, Y. Negi, and J. Balakrishnan, "RCS estimation of complex shaped aircraft and RCS reduction using partial RAM coating," *27th Annual Review of Progress in Applied Computational Electromagnetics (ACES)*, Williamsburg, Virginia, pp. 570-575, March, 2011.

[12] K. Mitzner, "Incremental length diffraction coefficients," *Northrop Corporation, Tech. Rep.* AFAL-TR-73-296, 1974.

[13] F. Weinmann, "UTD shooting-and-bouncing extension to a PO/PTD ray tracing algorithm," *Applied Computational Electromagnetics Society (ACES) Journal*, vol. 24, no. 3, pp. 281-293, 2009.

[14] H. Ling, R. Chou, and S. Lee, "Shooting and bouncing rays: Calculating the RCS of an arbitrary shaped cavity," *IEEE Trans. Antennas Propag.*, vol. 37, no. 2, pp.194-205, 1989.

[15] R. Kipp and M. Pavlovic, "Comparison of ray-tracing and MoM RCS solution for large realistic vehicle," *25th Annual Review of Progress in Applied Computational Electromagnetics (ACES)*, Monterey, California, pp. 571-576, March, 2009.

[16] C. Reddy, M. Deshpande, C. Cockrell, and F. Beck, "Fast RCS computation over a frequency band using method of moments in conjunction with asymptotic waveform evaluation technique," *IEEE Trans. Antennas Propag.*, vol. 46, no. 8, pp. 1229-1233, 1998.

[17] Y. Erdemli, J. Gong, C. Reddy, and J. Volakis, "Fast RCS pattern fill using AWE technique," *IEEE Trans. Antennas Propag.*, vol. 46 no. 11, pp. 1752-1753, 1998.

[18] X. Wang, S. Gong, J. Guo, Y. Liu, and P. Zhang, "Fast and accurate wide-band analysis of antennas mounted on conducting platform using AIM and asymptotic waveform evaluation technique," *IEEE Trans. Antennas Propag.*, vol. 59 no. 12, pp. 4624-4633, 2011.

[19] G. Burke, E. Miller, S. Chakrabarthi, and K. Demarest, "Using model-based parameter estimation to increase the efficiency of computing electromagnetic transfer functions," *IEEE Trans. Magn.*, vol. 25, pp. 2807-2809, 1989.

[20] A. Boag, "A fast physical optics (FPO) algorithm for high frequency scattering," *IEEE Trans. Antennas Propag.*, vol. 52, no. 1, pp. 197-204, 2004.

[21] A. Boag and E. Michielssen, "A fast physical optics (FPO) algorithm for double-bounce scattering," *IEEE Trans. Antennas Propag.*, vol. 52, no. 1, pp. 205-212, 2004.

[22] A. Boag and C. Letrou, "Multilevel fast physical optics algorithm for radiation from non-planar apertures," *IEEE Trans. Antennas Propag.*, vol. 53, no. 6, pp. 2064-2072, 2005.

[23] A. Manyas and L. Gurel, "Memory-efficient multilevel physical optics algorithm for fast computation of scattering from three-dimensional complex targets," *Computational Electromagnetics Workshop*, Izmir, Turkey pp. 26-30, 2007.

[24] L. Gurel and A. Manyas, "Multilevel physical optics algorithm for fast solution of scattering

problems involving nonuniform triangulations," *Antennas and Propagation Society International Symposium, IEEE*, Honolulu, Hawaii, pp. 3277-3280. 2007.
[25] M. Stephanson and J. Lee, "Fast physical optics calculation for SAR imaging of complex scatterers," *Antennas and Propagation Society International Symposium, IEEE*, Chicago, Illinois, pp. 1-2. 2012.
[26] O. Bucci and G. Franceschetti, "On the spatial bandwith of scattered," *IEEE Trans. Antennas Propag.*, vol. 35, no. 12, pp. 1445-1455, 1987.
[27] H. Buddendick and T. Eibert, "Acceleration of ray-based radar cross section predictions using monostatic-bistatic equivalence," *IEEE Trans. Antennas Propag.*, vol. 58, no. 2, pp. 531-539, 2010.
[28] F. Catedra, L. Lozano, I. Gonzalez, E. Garcia, and M. Algar, "Efficient techniques for accelerating the ray-tracing for computing the multiple bounce scattering of complex bodies modeled by flat facets," *Applied Computational Electromagnetics Society (ACES) Journal*, vol. 25, no. 5, pp. 395-409, 2010.
[29] Y. Tao, H. Lin, and H. Bao, "GPU-based shooting and bouncing ray method for fast RCS prediction," *IEEE Trans. Antennas Propag.*, vol. 58, no. 2, pp. 494-502, 2010.
[30] W. Gordon, "Far-field approximations to the kirchhoff helmholtz representations of scattered fields," *IEEE Trans. Antennas Propag.*, pp. 590-592, July 1975.
[31] K. Jin, T. Suh, S. Suk, B. Kim, and H. Kim, "Fast ray tracing using a space-division algorithm for RCS prediction," *J. Electromagn. Waves Applicat.*, vol. 20, no. 1, pp. 119-126, 2006.
[32] W. Chew, T. Cui, and J. Song, "A FAFFA-MLFMA algorithm for electromagnetic scattering," *IEEE Trans. Antennas Propag.*, vol. 50, no. 11, pp. 1641-1649, 2002.
[33] CST Microwave Studio 2006B by Computer Simulation Technology [Online]. Available: http://www.cst.com.

Yuyuan An received the B.Sc. degree in Electronic Information Engineering from the School of Electrical Engineering and Optical Technique, Nanjing University of Science and Technology, Nanjing, China, in 2009.

He is currently working towards the Ph.D degree in electromagnetic fields and microwave technology at the School of Electrical Engineering and optical technique, Nanjing University of Science and Technology. Her research interests include antennas, RF-integrated circuits, and computational electromagnetics.

Zhenhong Fan received the M.Sc. and Ph.D degrees in electromagnetic field and microwave technique from Nanjing University of Science and Technology (NJUST), Nanjing, China, in 2003 and 2007, respectively.

During 2006, he was with the Center of wireless Communication in the City University of Hong Kong, Kowloon, as a Research Assistant. He is currently an associate professor with the Electronic Engineering of NJUST. He is the author or coauthor of over 20 technical papers. His current research interests include computational electromagnetics, electromagnetic scattering and radiation.

Dazhi Ding received the B.Sc. and Ph.D degrees in Electromagnetic Field and Microwave Technique from Nanjing University of Science and Technology (NUST), Nanjing, China, in 2002 and 2007, respectively.

During 2005, he was with the Center of Wireless Communication in the City University of Hong Kong, Kowloon, as a research assistant. He is currently an associate professor with the Electronic Engineering of NJUST. He is the author or coauthor of over 30 technical papers. His current research interests include computational electromagnetics, electromagnetic scattering, and radiation.

Rushan Chen received the B.Sc. and M.Sc. degrees from the Department of Radio Engineering, Southeast University, China, in 1987 and 1990, respectively, and the Ph.D degree from the Department of Electronic Engineering, City University of Hong Kong, in 2001.

He joined the Department of Electrical Engineering, Nanjing University of Science and Technology (NJUST) in 1990. Since September 1996, he has been a Visiting Scholar with the Department of Electronic Engineering, City University of Hong Kong, first as Research Associate, then as a Senior Research

Associate, a Research Fellow, and a Senior Research Fellow. From June to September 1999, he was also a Visiting Scholar at Montreal University, Canada. In 1999, he was promoted to Full Professor and Associate Director of the Microwave and Communication Research Center in NJUST, and appointed Head of the Department of Communication Engineering in 2007. He was appointed as the Dean in the School of Communication and Information Engineering, Nanjing Post and Communications University in 2009. In 2011 he was appointed as Vice Dean of the School of Electrical Engineering and Optical Technique, NJUST. His research interests mainly include microwave/ millimeter-wave systems, measurements, antenna, RF-integrated circuits, and computational electromagnetics. He has authored or coauthored more than 200 papers, including over 140 papers in international journals.

Dr. Chen has received 6 prizes. In 2008, he became a Chang-Jiang Professor under the Cheung Kong Scholar Program awarded by the Ministry of Education, China. He was selected as a member of Electronic Science and Technology Group by academic degree commission of the State Council in 2009. He is a Senior Member of the Chinese Institute of Electronics (CIE), Vice-Presidents of Microwave Society of CIE and IEEE MTT/APS/EMC Nanjing Chapter. He serves as the reviewer for many technical journals, and now an Associate Editor for the International Journal of Electronics.

A Miniaturization Band-Pass Filter with Ultra-Narrow Multi-Notch-Band Characteristic for Ultra-Wideband Communication Applications

Yingsong Li [1], Wenxing Li [1], Wenhua Yu [1,2], and Chengyuan Liu [1]

[1] College of Information and Communications Engineering
Harbin Engineering University, Harbin 150001, China
liyingsong82@gmail.com, liwenxing@hrbeu.edu.cn, liuchengyuan@hrbeu.edu.cn

[2] 2COMU, Inc.
4031 University Drive, Suite 100, Fairfax, VA 22030, USA
wenyu@2comu.com

Abstract **─** In this paper, we present a novel approach for designing compact Ultra-Wideband (UWB) band-pass filters with desired multi-notch-band characteristics. The multi-notch-band features are realized by using a ring-stub multi-mode resonator, while the equivalent model is also obtained by using the odd/even excitation resonance condition. The fabricated prototype of the band-pass multi-notch-band filter demonstrates a good behavior as expected. Simulated and experimental results show that the proposed filter with a compact size of 25×10 mm^2, has an impedance bandwidth between 3.0 GHz and 10.6 GHz; while the multiple notch bands are achieved and their center frequencies are located at 3.9 GHz, 5.25 GHz, 5.9 GHz, 6.8 GHz and 8.0 GHz. The proposed filter is suitable for being integrated in UWB radio systems to efficiently enhance the interference immunity from unexpected signals, such as Worldwide Interoperability for Microwave Access (WiMAX), Wireless Local-Area Network (WLAN), 6.8 GHz Radio Rrequency Identification (RFID) communication and X-band satellite communications.

Index Terms - Band-pass filter, multi-notch band characteristics, notch band filter and UWB filter.

I. INTRODUCTION

Since the Federal Communications Commission (FCC) released the frequency band from 3.1 GHz to 10.6 GHz for commercial communication applications in February 2002, the Ultra-Wideband (UWB) radio system has been receiving more attention in both academic and industrial fields [1]. An UWB Band-Pass Filter (BPF) is one of the key passive components to realize an UWB radio system; which has attracted more attention recently. A great number of methods have been proposed in order to design BPFs with large Fractional Bandwidths (FBW) and good performance [2-6]. There have existed the typical structures, including low and high-pass filter configurations [2], Coplanar Waveguide (CPW) geometries [3], right/left-handed structures [4], microstrip cascaded fork-form resonator [5] and defected ground structure [6]. However, there are some drawbacks in these designs, such as out-of-band performance and complicated structure.

On the other hand, there are some existing narrow-band systems which have been used in the communications for a long time. Furthermore, the UWB frequency band overlaps with these existing narrow communication systems, such as WiMAX in 3.4 GHz to 3.69 GHz band, WLAN in 5.2 GHz and 5.8 GHz bands and 6.8 GHz RFID band. Those narrowband radio signals might interfere with UWB systems and vice versa. To mitigate the potential interference, design of compact UWB BPFs with notched band characteristics is one of the most challenging topics. Consequently, a number of methods have been proposed and investigated to design UWB BPFs with notched bands [7-22], such as embedded Complementary Split Ring Resonators (CSRR) [7], Defected

Submitted On: April 27, 2013
Accepted On: April 19, 2014

Ground Structures (DGS) [8,11], mismatch transmission lines [9], short-circuited stubs [10]; which can effectively reject unexpected radio signals. Nevertheless, some of these previously proposed band-notched UWB filters are still large in size [7], incompatible with Monolithic Microwave Integrated Circuits (MMIC) [8], complicated in structures [9] and sophisticated in band rejection characteristic design [7-11].

In this paper, we present a novel approach to designing compact Ultra-Wideband (UWB) band-pass filter with a good multi-notch-band characteristic. The proposed multi-notch-band characteristic is realized by using Ring-Stub Multi-Mode Resonator (RSMMR). The resonance condition of RSMMR is obtained by means of odd and even mode theorem [14]. In comparison with the existing UWB notch-band filter in [7-13], the proposed notched bands can be easily operated simultaneously. Performance of the proposed filter is validated by fabricating the proposed multi-notch-band band-pass UWB filter on a RT/Duorid 6006 substrate, that has a relative dielectric constant of 6.15 and a thickness of 0.635 mm.

II. FILTER DESIGN

In this section, the design procedure and synthesis method of the proposed compact UWB BPF with multi-notch bands are described on the basis of loading stub technique. Generally speaking, the proposed filter essentially exploits Multi-Mode Resonator (MMR) structures to realize the sharp and adjustable multi-notch-band.

The schematic diagram of the proposed UWB BPF with multi-notch-band characteristics is shown in Fig. 1. The proposed UWB BPF is a modification structure in [22], in which the multi-mode resonator structures are coupled to the middle ring resonator section, to achieve the required multi-notch bands. The equivalent transmission line network of the proposed filter is illustrated in Fig. 2. The interdigital coupled line is equivalent to a combination of the two signal transmission lines on two sides and a J-inverter susceptance. The multi-mode resonator coupled to the middle section of the ring resonator can be analyzed by a shunt series resonant branch, as shown in Fig. 2. Furthermore, in Fig. 1, the multi-mode resonator structure can be equivalent to an LC resonator network whose parameters are L_i and C_i with $1 \leq i \leq 5$; which are shown in Fig. 2. Therefore, each resonator can be regarded as an LC resonator, which is related to the corresponding notch band. Here, the L and C can be obtained from resonator theory.

Two capacitive-ended interdigital coupled into the I/O lines possess a wide-stop-band performance [22]. In this paper, we use the middle ring resonator to realize the multi-notch bands. The design idea and procedure of the multi-notch bands are described in Fig. 3. First, we improve the prototype filter proposed in [22] to cast a ring structure denoted as a simplified prototype filter. Then, a transition filter-1 is designed based on the simplified prototype filter by inserting a general stub into the ring resonator to produce a notch-band characteristic. As for filter-1, the inserted general stub is acted as a resonator, which is designed to provide a notch band. As a result, there is no coupling current at the output of filter-1. Therefore, the filter-1 can effectively reject the unwanted signal at corresponding frequency band. To make it suitable for dual-notch-band applications, another general stub is employed and inserted into the ring resonator based on the transition filter-1 to design a dual-notch-band filter, which is referred to as transition filter-2. The transition filter-2 can be treated as a ring resonator with two general stubs inserted into the simplified prototype filter. To render the proposed filter more useful in practice, a ring resonator with two stubs is employed to construct a tri-notch filter, referred to as transition filter-3. By considering the design procedure of the notch band filters aforementioned, an UWB band-pass filter with multi-notch bands is proposed by integrating three stubs, a ring resonator and a Stepped Impedance Resonator (SIR) into the simplified prototype filter; which is denoted as the final filter, as shown in Fig. 3. To give an insight into the performance of the proposed multi-notch-band filter, the proposed transition filters together with stubs and ring resonator are analyzed. Next, we investigate the characteristics of the single notch band to analyze the proposed transition filter-1. The geometry of the proposed transition filter-1 is illustrated in Fig. 4 and the equivalent circuits of the ring resonator are shown in Fig. 5.

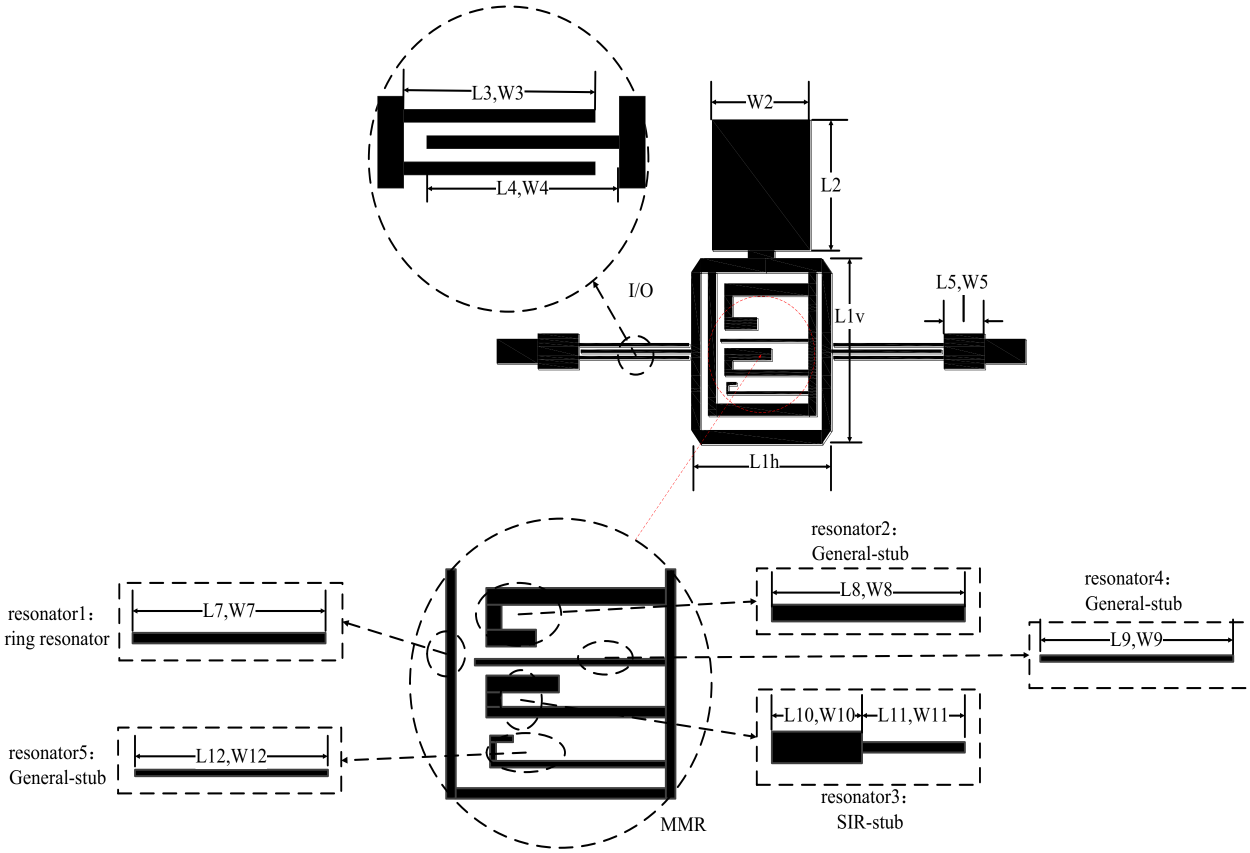

Fig. 1. Configuration and dimensions of the proposed filter.

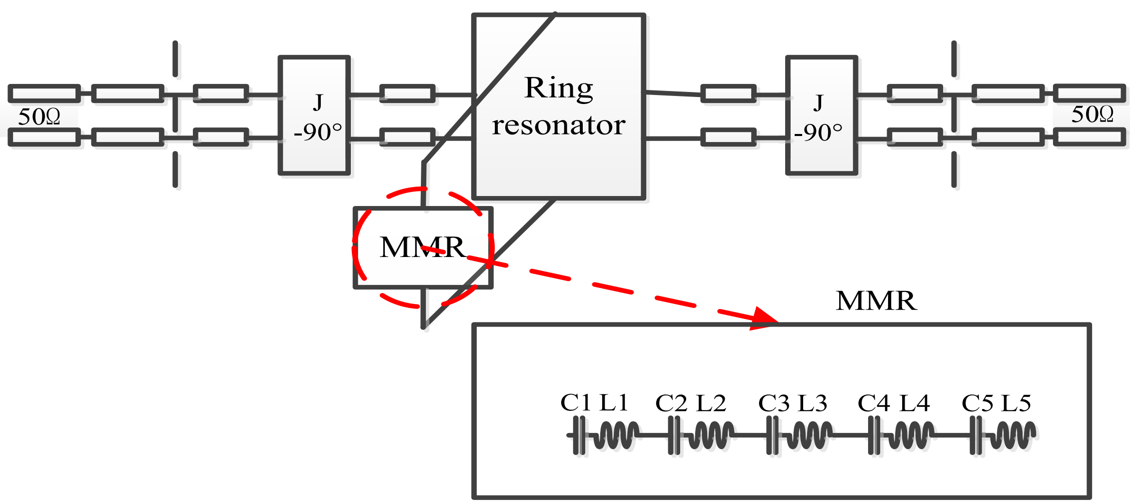

Fig. 2. Equivalent circuit network of the proposed filter.

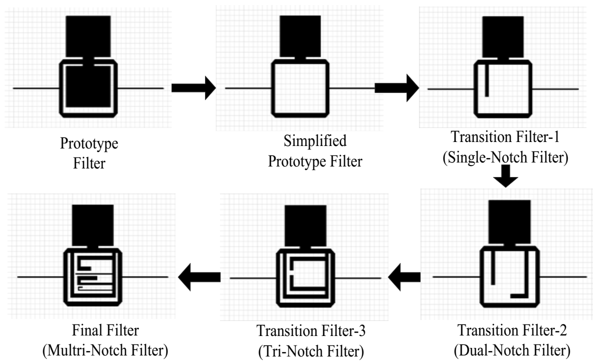

Fig. 3. Design procedure of the proposed UWB filter.

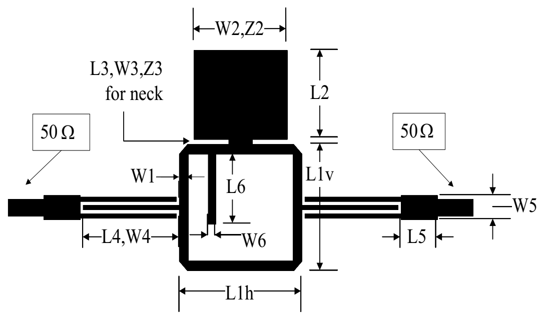

Fig. 4. Geometry of the transition filter-1.

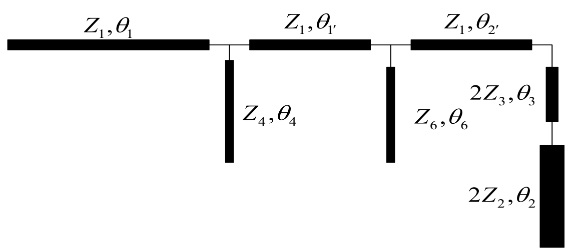

(a) Even-mode

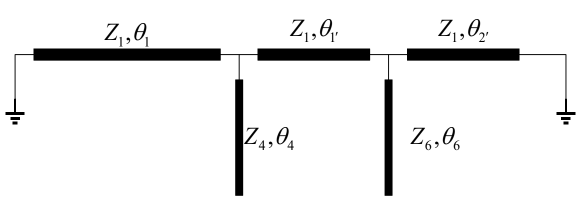

(b) Odd-mode

Fig. 5. Equivalent circuits of the ring resonator in Fig. 4.

The middle ring resonator of transition filter-1 can be analyzed based on the even and odd mode methods. Even-mode and odd-mode equivalent circuits for the ring resonator fed by the interdigital coupled lines in Fig. 4, are shown in Figs. 5 (a) and (b). On the basis of the odd-mode equivalent circuit, the odd-mode forms a pass band only, while the even-mode is designed for not only the pass-band but also the notch-band. In this paper, it is desirable to design an UWB BPF with a sharp and tunable notch-band. Thus, we will describe how to realize a notch band using the stub technique mentioned above. As the even-mode can be designed for both the pass-band and notch-band applications, we will only analyze the resonance condition about the even-mode. By considering the analysis procedure in [14, 23], the even-mode resonance condition proposed herein can be achieved and expressed by the equation below for $Y_{in} = 0$. For the even-modes:

$$Y_{in} = \frac{\tan\theta_1 + \left(K''\right)^{-1}\tan\theta_4 + \dfrac{(\tan\theta_1' + R)}{1-\tan\theta_1' R}}{1-\tan\theta_1[(K'')^{-1}\tan\theta_4 + (\dfrac{(\tan\theta_1' + R)}{1-\tan\theta_1' R})]} = 0, \quad (1)$$

where,

$$R = (K''')^{-1}\tan\theta_5 + \frac{\tan\theta_2' + \dfrac{1}{2}[\dfrac{(K')^{-1}\tan\theta_3 + K^{-1}}{1-K'(K)^{-1}\tan\theta_3\tan\theta_2}]}{1-\dfrac{1}{2}\tan\theta_2'[\dfrac{(K')^{-1}\tan\theta_3 + K^{-1}}{1-K'(K)^{-1}\tan\theta_3\tan\theta_2}]}. \quad (2)$$

In the equations above, the K, K', K'' and K''' can be expressed as:

$$K = \frac{Z_2}{Z_1}, K' = \frac{Z_3}{Z_1}, K'' = \frac{Z_4}{Z_1}, K''' = \frac{Z_5}{Z_1}. \quad (3)$$

The simulation parameters are listed as follows (unit: mm): L1v=5.12, L1h=5.92, L2=4.25, L3=0.25, L4=5.39, L5=2.0, W1=0.46, W2=5.2, W3=1.3, W4=0.11 and W5=1.15. In the next step, we use these parameters to simplify the even-mode resonance condition. Based on the parameters above, we can get $\theta_6 \approx 70°$ and then the length of the stub is close to $7\lambda_{notch}/36$, where λ_{notch} corresponding to the center frequency of the notch can be expressed as:

$$\lambda_{notch} = \frac{C}{f_{notch}\sqrt{\varepsilon_{eff}}}, \quad (4)$$

where, f_{notch} is the center frequency of the notch band, ε_{eff} is the effective dielectric constant and

C is the speed of light in free space. The effective dielectric constant ε_{eff} can be given using the equation (5) below:

$$\varepsilon_{eff} = \frac{\varepsilon_r + 1}{2} + \frac{\varepsilon_r - 1}{2}\left[(1 + 12\frac{h}{w})^{-1/2} + 0.04(1 - \frac{w}{h})^2\right]. \quad (5)$$

To understand the performance of the proposed transition filter-1, the transmission coefficients obtained by using IE3D are plotted in Fig. 6.

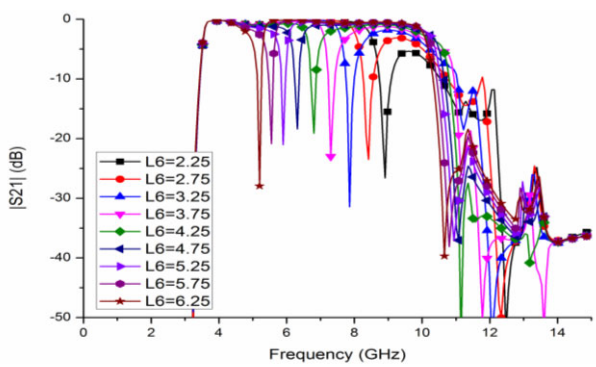

Fig. 6. Transmitted coefficient of the filter-1 for different L6 values.

Figure 6 shows the transmission characteristic of the proposed transition filter-1. The notched band moves toward the lower frequency when increasing the length of L6 and L6=4.25 mm is selected for the optimum design. In this case, we can design the notch band to use at 6.8 GHz band. To further study the nature of the performance of this filter, the current density distribution on the proposed transition filter-1at 6 GHz in the pass-band, is shown in Fig. 7, meanwhile the notch band at 6.8 GHz is obtained.

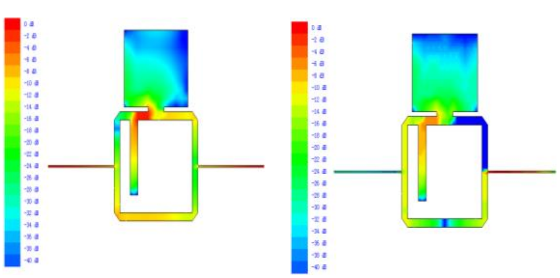

(a) 6 GHz (b) 6.8 GHz

Fig. 7. Current density distribution on the proposed transition filter-1.

It can be seen from Fig. 7, that the resonator neither resonates nor effects on the overall performance at 6 GHz in the pass-band, while the maximum current density distribution is on the stub that produces the 6.8 GHz notch band. Figure 7 (b) clearly shows that the resonator at the notched frequency is acting as a short circuit and no coupling exists on the stub at the output port. As mentioned above, the notched band can be easily controlled by adjusting the stub dimensions. In particular, the length of the stub decides the center frequency of the notch-band and the frequency bandwidth of the notch-band is determined by the stub width. Next, we will discuss the transition filter-2.

The theoretical design and synthesis of a compact UWB BPF with dual-notch-band features generated by using two inserted stubs, is shown in Fig. 8. Technically, the proposed filter design essentially exploits the open stub structures to realize dual sharp and adjustable notch-band characteristics. The corresponding lumped equivalent circuits and the equivalent circuit network of the proposed transition filter-2, are shown in Fig. 9.

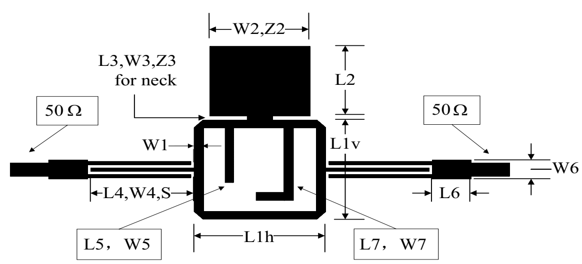

Fig. 8. Geometry of proposed transition filter-2.

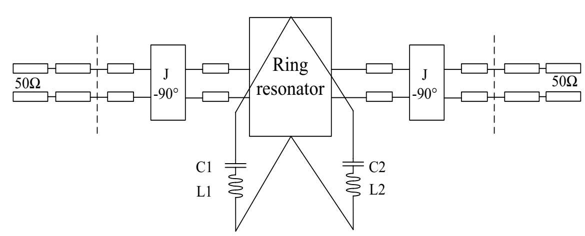

Fig. 9. Equivalent circuit network of proposed transition filter-2.

The middle ring resonator can be analyzed in terms of even and odd modes. Even-one, even-two and odd-mode equivalent circuits for the ring resonator fed by the interdigital-coupled lines in Fig. 8, are shown in Figs. 10 (a), (b) and (c), respectively. From the odd-mode equivalent circuits, we can see that the odd-mode only designs for the pass band. On the other hand, the even-mode designs not only for the pass-band but also for the notch-band. In this paper, we design an UWB pass-band filter with two sharp and adjustable notch-bands. We only analyze the resonance condition for these even-modes and the even-mode resonance condition can be achieved for $Y_{in} = 0$.

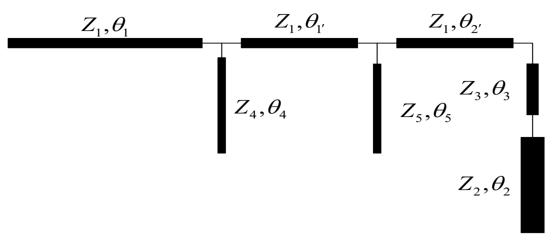

(a) Even-mode-one

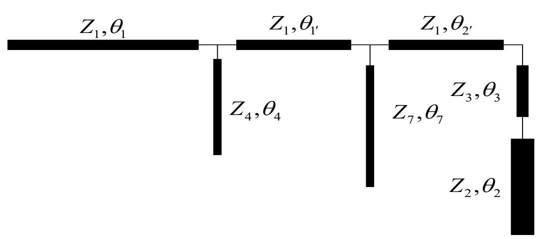

(b) Even-mode-two

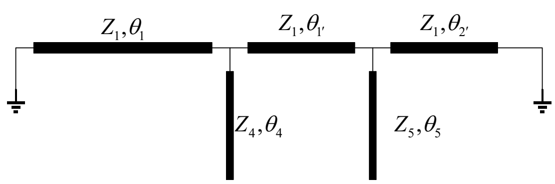

(c) Odd-mode

Fig. 10. Equivalent circuits for the ring resonator in Fig. 8; (a) even-mode one, (b) even-mode two and (c) odd mode.

The input admittance for one or two even-modes is expressed as:

$$Y_{in} = \frac{\tan\theta_1 + (K'')^{-1}\tan\theta_4 + \dfrac{(\tan\theta_1' + R)}{1-\tan\theta_1' R}}{1-\tan\theta_1[(K'')^{-1}\tan\theta_4 + (\dfrac{(\tan\theta_1' + R)}{1-\tan\theta_1' R})]} = 0, \qquad (6)$$

where,

$$R = (K''')^{-1}\tan\theta_5 + \frac{\tan\theta_2' + \dfrac{1}{2}[\dfrac{(K')^{-1}\tan\theta_3 + K^{-1}}{1-K'(K)^{-1}\tan\theta_3\tan\theta_2}]}{1-\dfrac{1}{2}\tan\theta_2'[\dfrac{(K')^{-1}\tan\theta_3 + K^{-1}}{1-K'(K)^{-1}\tan\theta_3\tan\theta_2}]} \qquad (7)$$

In the equation above, K, K', K'' and K''' can be expressed as:

$$K = \frac{Z_2}{Z_1},\ K' = \frac{Z_3}{Z_1},\ K'' = \frac{Z_4}{Z_1},\ K''' = \frac{Z_5}{Z_1} \text{ or } \frac{Z_7}{Z_1}.$$

In this filter, the design parameters are listed below (unit: mm): L1v=5.12, L1h=5.92, L2=4.25, L3=0.25, L4=5.39, W1=0.46, W2=5.2, W3=1.3, W4=0.11 and W5=1.15. Next, we use these parameters to simplify the even-mode resonance condition. Based on these parameters, we can get $\theta_{5(7)} \approx 70°$ and then the length of the stub is close to $7\lambda_{notch}/36$. To understand the performance of the notch bands, the transmitted coefficients of the transition filter-2 are plotted in Fig. 11.

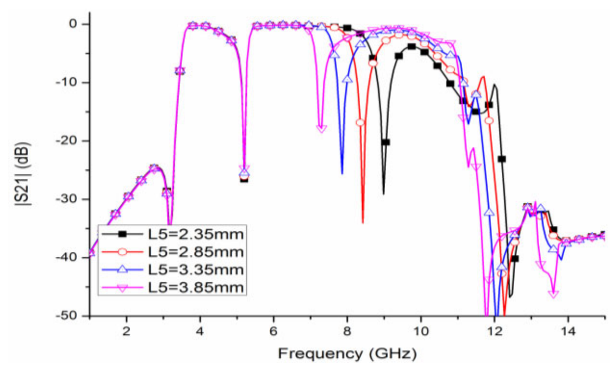

(a) Transmission coefficients with varying L5

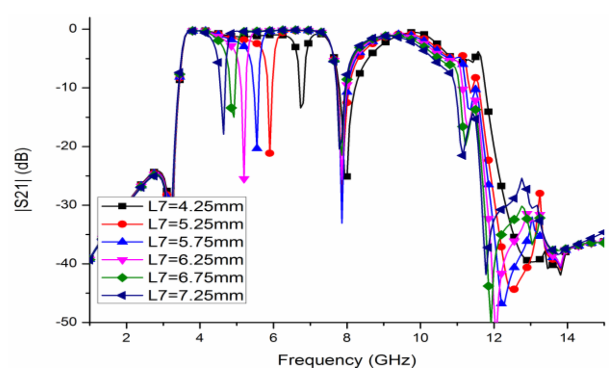

(b) Transmission coefficients with varying L7

Fig. 11. Transmitted coefficient of the transition filter-2.

Figure 11 (a) shows the transmission property of the mentioned transition filter-2 with different

L5. By increasing L5, the notched band moves toward the lower frequency. The higher notch band can be tuned from 7 GHz to 9.2 GHz. Figure 11 (b) shows the transmission property of the transition filter-2 for different L7. It is found that the notched band moves toward the lower frequency with the increment of L7 and the notch band can be tuned from 4 GHz to 7 GHz. In this paper, L5=3.35 mm and L7=6.25 mm are selected to investigate the transition filter-2. In this case, the two notch bands are located at 4.9 GHz and 7.8 GHz. To investigate the operation property of the transition filter-2, the current density distribution on the proposed middle ring resonator in both the pass-band and notch-band are illustrated in Fig. 12.

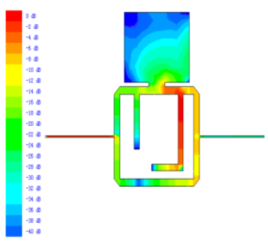
(a) 7.8 GHz

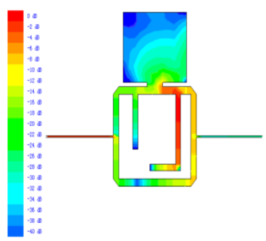
(b) 4.9 GHz

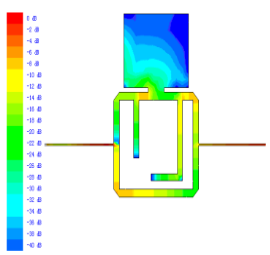
(c) 6 GHz

Fig. 12. Current density distribution on the transition filter-2.

It can be seen from Fig. 12 that the current density distributions are on the transition filter-2 at 6 GHz in the pass-band. Thus, the resonator neither resonates nor affects the overall performance. At the notched frequencies 4.9 GHz and 7.8 GHz, the resonator has a focus of current density on the stubs. At the input port, the current is high while the current at the output port is low. Thus, the signal is prevented by the notch characteristics. Figures 12 (a) and (b) clearly show that the resonator at the notched frequency is acting as a short circuit and no coupling exists over the stub at the output port. As mentioned above, the frequency of the notched band can be easily controlled by adjusting the stub dimensions. In particular, the stub length decides the center frequency of the notch band and the stub width decides the bandwidth of the notch-band. For the geometry shown in Fig. 13, the proposed UWB filter with tri-notch-band characteristics, referred to as transition filter-3, is investigated in [14]. The transition filter-3 is composed of two interdigital hairpin resonator units, middle ring-stub multi-mode resonator and two 50-Ω SIR fed structures. Several folded stubs are inserted to the middle ring resonator section to achieve the tri-notch-bands.

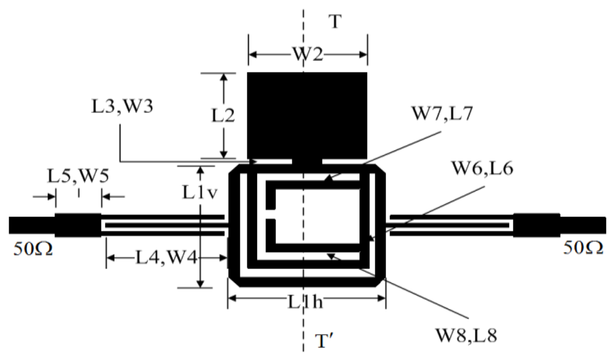

Fig. 13. Geometry of the proposed transition filter type three.

Based on the analysis and the simulated results mentioned above, an UWB filter with multi-notch-band characteristic is proposed, as shown in Fig. 1. To analyze this filter in detail, we decompose the filter to 5 resonators. Firstly, we embedded the resonator-1 and resonator-2 to the simplified prototype filter to create the dual-notch-band characteristic. The first notch-band and the second notch-band are realized by using the resonator-1 and the resonator-2, respectively. The notch characteristics of this filter are obtained by using IE3D, as shown in Fig. 14 (a). We can see from Fig. 14 (a), that with increase of the length of L8, the center frequency of the second notch band moves to the lower frequency, while the center frequency of the first notch band changes slightly. Thus, the second notch band can be tuned by adjusting the length of L8.

Secondly, the resonator-1, resonator-2 and resonator-3 are inserted into the simplified prototype filter to create tri-notch-band characteristic. At the beginning of this design, a general stub resonator is used for designing resonator-3. The notch characteristics of this filter are shown in Fig. 14 (b). With increasing the length of L10 + L11, the center frequency of the third notch band moves to the lower frequency. In addition, the center frequency of the first notch band also shifts to the lower side. For getting a method to adjust to the third notch-band that has no effects on the first and the second notch bands, we use a Stepped Impedance Resonator (SIR) stub instead of the general stub resonator. The SIR-stub has another key parameter to adjust the notch-band. The characteristics of the SIR-stub are shown in Fig. 14 (c). With the increase of the width of W11, the center frequency of the third notch band moves to the lower frequency and the other two notch-bands remain unchanged. These three notch-bands can be effectively adjusted.

Thirdly, we insert another stub to the designed tri-notch-band filter using resonator 1, resonator 2, resonator 3 and resonator 4, to create four-notch-band characteristics. The fourth notch-band is generated by the resonator-4. The notch band characteristic is simulated by using IE3D and the simulated results are shown in Fig. 14 (d). With the increase of the length of L9, the central frequency of the fourth notch band moves towards the lower direction. At the same time, the central frequencies of the other notch bands are changed slightly. So we can control the fourth notch band by adjusting the dimension of L9.

Finally, another resonator is inserted to the four-notch-band filter to create the final filter, which is obtained by using the resonator-5. The notch characteristics of the constructed filter are simulated by using IE3D and the simulated results are shown in Fig. 14 (e). With the increase of the length of L12, the central frequency of the fifth notch band moves towards the lower frequency, while the central frequencies of the other notch bands keep nearly constant. Thus, we can control the fifth notch band by adjusting the dimension of L12. According to the analytical and the simulated results above, the designed multi-notch-band characteristics can be simultaneously obtained by choosing the proper dimensions of the middle ring-stub multi-mode resonator, the stubs and the SIR.

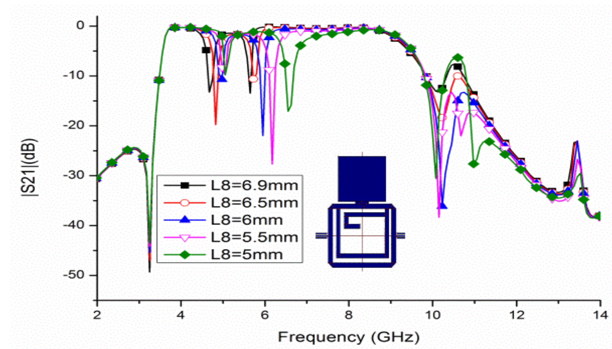

(a) L8

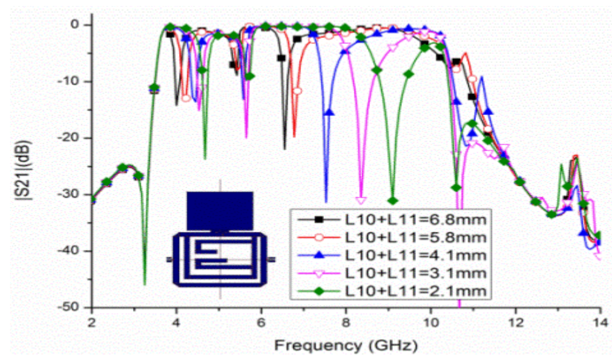

(b) L10 + L11

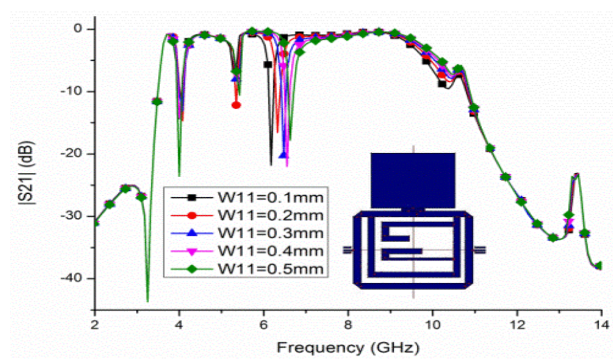

(c) W11

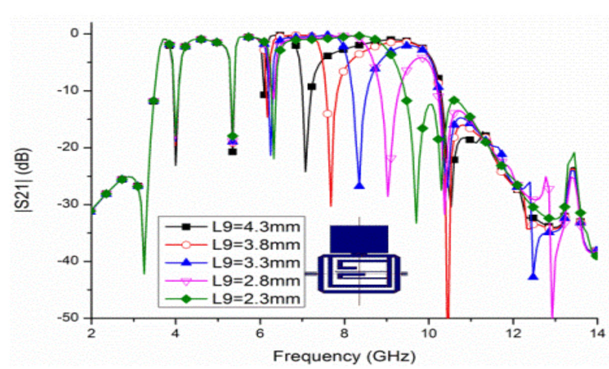

(d) L9

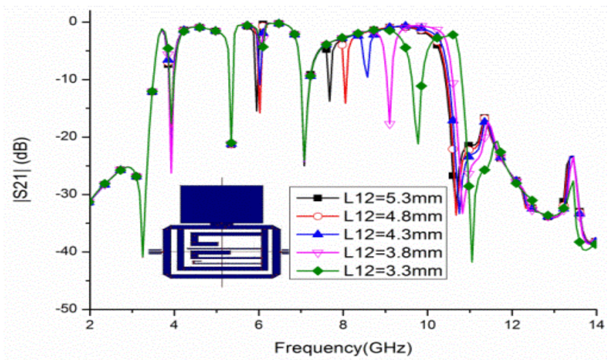

(e) L12

Fig. 14. Transmitted coefficient variation of the proposed filter.

To understand the filter property further, the current density distribution on the proposed final filter is investigated at several frequencies, as shown in Fig. 15; in which Figs. 15 (a) and (b) show the current density distribution on the multi-notch-band UWB filter at 4.5 GHz and 9 GHz in the pass-band. It can be seen that the current density distributions on the input and output port are significant, while the current density distribution on the multi-mode resonator is smaller at 4.5 GHz and 9 GHz in the pass-band; implying that the signal can be transformed from the input port to the output port in the pass-band and the multi-mode resonator has no effects on the pass band. Figures 15 (c)-(g) show the current density distributions on the proposed filter at the five notch bands. It is observed that the current density distributions on the input port are strong, while they are smaller on the output port and the current density distribution on the multi-mode resonator is very large at the notch-band frequency; implying that the signal cannot be transformed from the input port to the output port on the notch-band. These signals are rejected by the multi-mode resonator. Thus, the five notched bands can be obtained at 3.9 GHz, 5.25 GHz, 5.9 GHz, 6.8 GHz and 8 GHz. Figures 15 (h) and (i) illustrate the current density distributions on the proposed multi-notch-band UWB filter on the stop band. It can be seen that the current density distributions at 2.5 GHz and 12 GHz are mainly concentrated on the input port. The current density distributions are smaller on the multi-mode resonator in the stop-band, which means that the signals cannot be transformed from the input port to the output port in the stop-band. These signals are reflected by the interdigital coupled lines.

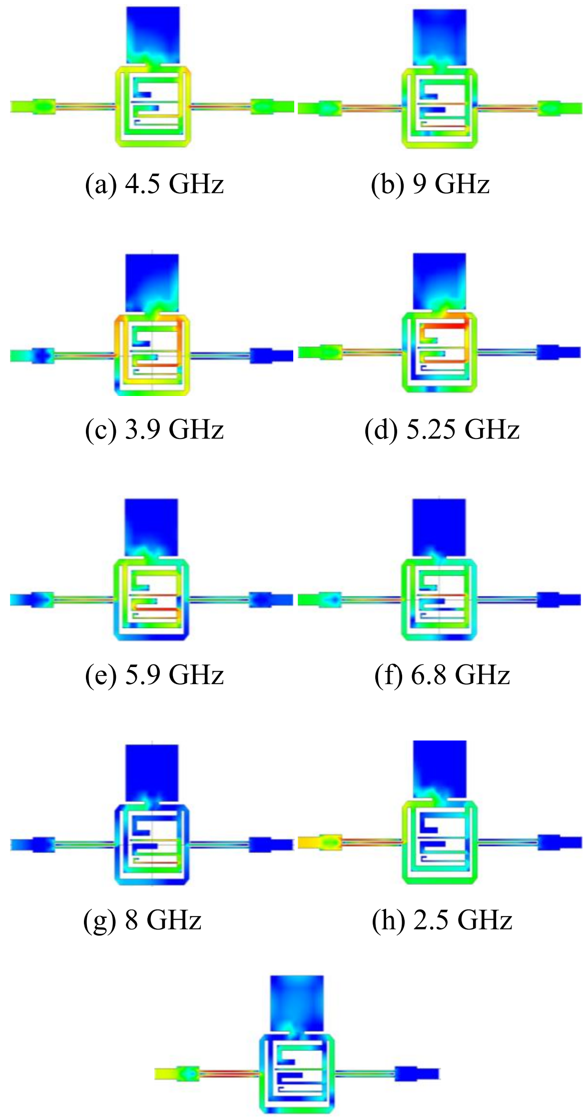

(a) 4.5 GHz (b) 9 GHz

(c) 3.9 GHz (d) 5.25 GHz

(e) 5.9 GHz (f) 6.8 GHz

(g) 8 GHz (h) 2.5 GHz

(i) 12 GHz

Fig. 15. Current density distributions on the multi-notch band UWB filter (left: input port; right: output port).

III. RESULTS AND DISCUSSIONS

To evaluate the performance of the multi-notch band UWB filter, the parameters of the designed filter are optimized numerically through IE3D. Optimal parameters of the five-notched band UWB filter are listed in Table 1. To verify the effectiveness of the proposed filter, the proposed filter is fabricated, which is shown in

Fig. 16. The filtering performance was measured by using Anristu 37347D vector network analyzer. Figure 17 demonstrates the frequency responses of the proposed filter. The measured results agree well with the simulated results. The discrepancies between the simulated and measured results may be caused by the fabrication errors.

Table 1: Dimensions of the proposed tri-notch band UWB filter

Parameter	Size (mm)	Parameter	Size (mm)
L1v	5.12	W1	0.46
L1h	5.92	W2	4.4
L2	4.25	W3	0.11
L3	5.4	W4	0.11
L4	5.4	W5	1.5
L5	2	W6	0.4
L6	0.25	W7	0.4
L7	13.8	W8	0.4
L8	6.5	W9	0.1
L9	4.3	W10	0.4
L10	1	W11	0.2
L11	3.1	W12	0.1
L12	4.8		

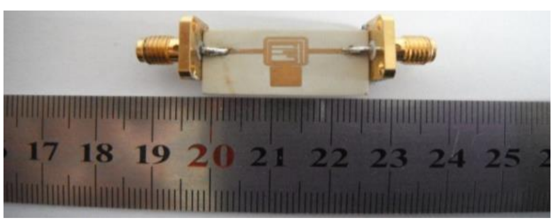

Fig. 16. Prototype of the proposed multi-notch band UWB filter.

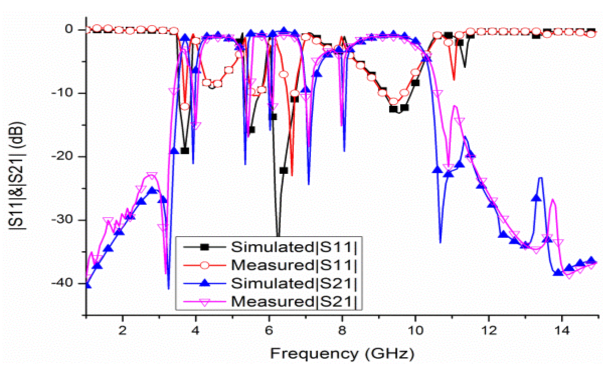

Fig. 17. Comparison between the simulated and measured results of the fabricated filter.

We can see that the fabricated filter has a measured pass-band from 3.1 GHz to 10.7 GHz with five notch bands, while the center frequencies of the notched bands are located at 3.86 GHz, 5.2 GHz, 5.9 GHz, 6.82 GHz and 7.95 GHz. The group delays shown in Fig. 18 are 0.2 ns and 0.6 ns at the six pass-bands, respectively. It is worth noting that the ring-stub multi-mode resonator can generate five notched bands at the desired frequencies with no significant influence on the wide pass-band performance. Moreover, the proposed UWB BPF has a good five-notch-band characteristic for implementing the functions of UWB radio system.

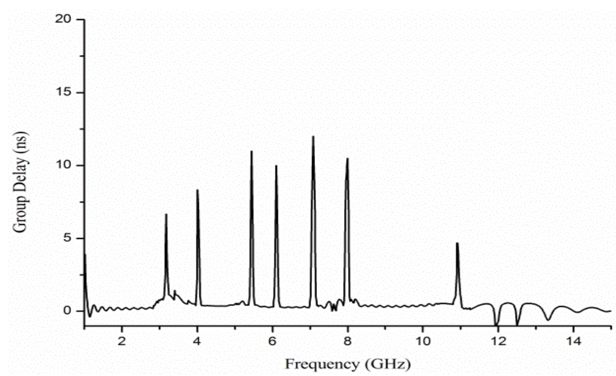

Fig. 18. Group delay of the fabricated filter.

IV. CONCLUSIONS

In this paper, a compact UWB band-pass filter with five ultra-narrow notch-band characteristic has been proposed and has been verified experimentally and numerically. The design procedures are described in details and investigated by using IE3D. By inserting a ring-stub multi-mode resonator with various stubs into an original UWB BPF, the multi-notch-band functions are obtained to reject undesired signals, such as WiMAX (3.5 GHz band), WLAN (5.2 GHz and 5.8 GHz bands), 6.8 GHz RFID and X-band (7.25 GHz to 8.0 GHz) for satellite communication applications. Simulated and measured results have demonstrated that the ring-stub multi-mode resonator can give five narrow notched bands at the undesired radio signals with no significant influence on the wide pass-band performance. The proposed filter is promising for use in UWB systems due to its simple structure, compact size and excellent performance.

ACKNOWLEDGMENT

This work was partially supported by National Defense "973" Basic Research Development Program of China (No. 6131380101). This paper is also supported by Pre-Research Fund of the 12th Five-Year Plan (No.4010403020102) and Fundamental Research Funds for the Central Universities (HEUCFT1304). The authors are also thankful to Hebei VSTE Science and Technology Co., Ltd., for providing the measuring facility.

REFERENCES

[1] "Revision of Part 15, the commission's rules regarding to ultra-wideband transmission system," *First Note and Order Federal Communication Commission, ET-Docket, FCC*, pp. 98-153, 2002.

[2] C. Hsu, F. Hsu and J. Kuo, "Microstrip bandpass filters for ultra-wideband (UWB) wireless communications," *IEEE MTT-S International Microwave Symposium Digest*, pp. 679-682, 2005.

[3] H. Wang, L. Zhu and W. Menzel, "Ultra-wideband bandpass filter with hybrid microstrip/CPW structure," *IEEE Microwave Wireless Compon. Lett*., vol. 15, pp. 844-846, 2005.

[4] J. Huang and Q. Chu, "Compact UWB band-pass filter utilizing modified composite right/left-handed structure with cross coupling," *Progress In Electromagnetics Research*, vol. 107, pp. 179-186, 2010.

[5] H. Chen and Y. Zhang, "A novel and compact UWB band pass filter using microstrip fork-form resonators," *Progress In Electromagnetics Research*, vol. 77, pp. 273-280, 2007.

[6] L. Yang, Y. Hongchun, W. Yawei and X. Shaoqiu, "Ultra-wideband bandpass filter based on parallel-coupled microstrip lines and defected ground structure," *Applied Computational Electromagnetics Society Journal*, vol. 28, no. 1, pp. 21-26, January 2013.

[7] L. Qiang, Y. Zhao, Q. Sun, W. Zhao and B. Liu, "A compact UWB band pass filter based on complementary split-ring resonators," *Progress In Electromagnetics Research C*, vol. 11, pp. 237-243, 2009.

[8] M. Naghshvarian Jahromi and M. Tayarani, "Miniature planar UWB band pass filters with circular slots in ground," *Progress In Electromagnetics Research Letters*, vol. 3, pp. 87-93, 2008.

[9] B. Yao, Y. Zhou, Q. Cao and Y. Chen, "Compact UWB band pass filter with improved upper-stopband performance," *IEEE Microwave and wireless components Lett*., vol. 19, pp. 27-29, 2009.

[10] H. Shaman and J. Hong, "Ultra-wideband (UWB) band pass filter with embedded band notch structures," *IEEE Microw. Wireless Compon Lett*., vol. 17, pp. 193-195, 2007.

[11] L. Chen, Y. Shang and Y. Zhang, "Design of a UWB bandpass filter with a notched band and wide stopband," *Microwave Journal*, vol. 52, pp. 96-105, 2009.

[12] S. Gao, S. Xiao and J. L. Li, "Compact ultra-wideband (UWB) bandpass filter with dual notched bands," *Applied Computational Electromagnetics Society Journal*, vol. 27, no. 10, pp. 795-800, October 2012.

[13] C. Liu, Y. Li and J. Zhang, "A novel UWB filter with WLAN and RFID stop-band rejection characteristic using tri-stage radial loaded stub resonators," *Applied Computational Electromagnetics Society Journal*, vol. 27, no. 9, pp. 749-758, September. 2012.

[14] Y. Li, W. Li, C. Liu and Q. Ye, "A Compact UWB band-pass filter with ultra-narrow tri-notch-band characteristic," *Submitted to Applied Computational Electromagnetics Society (ACES) Journal*.

[15] C. Liu, T. Jiang and Y. Li, "A novel UWB filter with notch-band characteristic using radial-UIR/SIR loaded stub resonators," *Journal of Electromagnetic Waves and Application*, vol. 25, pp. 233-245, 2011.

[16] T. Jiang, C. Liu, Y. Li and M. Zhu, "Research on a novel microstrip UWB notch-band BPF," *Asia Pacific Microwave Conference*, pp. 261-264, 2009.

[17] P. Hsiao and R. Weng, "Compact tri-layer ultra-wideband bandpass filter with dual notch bands," *Progress In Electromagnetics Research*, vol. 106, pp. 49-60, 2010.

[18] P. Hsiao and R. Weng, "Compact open-loop UWB filter with notched band," *Progress In Electromagnetics Research Letters*, vol. 7, pp. 149-159, 2009.

[19] Y. Wu, C. Liao and X. Xiong, "A dual-wideband band pass filter based on E-shaped microstrip SIR with improved upperstop band performance," *Progress In Electromagnetics Research*, vol. 108, pp. 141-153, 2010.

[20] J. Huang, Q. Chu and C. Liu, "Compact UWB filter based on surface-coupled structure with dual notch bands," *Progress In Electromagnetics Research*, vol. 106, pp. 311-319, 2010.

[21] S. Pirani, J. Nourinia and C. Ghobadi, "Band-notched UWB BPF design using parasitic coupled line," *IEEE Microwave and wireless components Lett*., vol. 20, pp. 444-446, 2010.

[22] C. Kim and K. Chang, "Ultra-wideband (UWB) ring resonator band-pass filter with a notched

band," *IEEE Microwave and Wireless Components Letters*, vol. 21, no. 4, pp. 206-208, 2011.

[23] C. Kim and K. Chang, "Ring resonator band pass filter with switchable bandwidth using stepped-impedance stubs," *IEEE Transactions on Microwave Theory and Techniques*, vol. 58, no. 12, pp. 3936-3944, 2010.

Yingsong Li received his B.S. degree in Electrical and Information Engineering and his M.S. degree in Electromagnetic Field and Microwave Technology from Harbin Engineering University, in 2006 and 2011, respectively. Now he is a Ph.D. candidate at Harbin Engineering University, China. He is a student member of the Chinese Institute of Electronics (CIA), IEEE and IEICE. His recent research interests are mainly in microwave theory, small antenna technologies and computational electromagnetic.

Wenxing Li received his B.S. and M.S. degrees from Harbin Engineering University, Harbin, Heilongjiang, China in 1982 and 1985, respectively. He is currently a full professor at College of Information and Communication Engineering, Harbin Engineering University, China. He is also the head of Research Centre of EM Engineering & RF Technology. He visited the Department of Electrical Engineering of the Pennsylvania State University, USA from June to August, 2010. He also visited the Oriental Institute of Technology, Taiwan from August to October, 2010. He is also the organizer of the 30th Progress in Electromagnetics Research Symposium (PIERS), the IEEE International Workshop on Electromagnetics (iWEM), the TPC of 2012 Asia-Pacific Symposium on Electromagnetic Compatibility (APEMC 2012) and the 2012 Global Symposium on Millimeter Waves (GSMM 2012). His recent research interests are mainly in computational electromagnetic, microwave engineering, modern antenna design and microwave and millimeter wave circuits.

Chengyuan Liu received his B.S. degree in Electrical and Information Engineering and his M.S. degree in Electromagnetic Field and Microwave Technology from Harbin Engineering University, 2006 and 2011, respectively. Now he is a Ph.D. candidate at Harbin Engineering University, China. He serves as receivers for the Journal of Electromagnetic Waves and Applications, Journal of Microwaves, Optoelectronics and Electromagnetic Applications, Progress in Electromagnetics Research Series and Journal of Electromagnetic Waves and Applications. His research interests are mainly in microwave theory, UWB antenna and UWB filters.

Wenhua Yu joined the Department of Electrical Engineering of the Pennsylvania State University and has been a Group Leader of the electromagnetic communication lab since 1996. He received his Ph.D. in Electrical Engineering from the Southwest Jiaotong University in 1994. He worked at Beijing Institute of Technology as a Postdoctoral Research Associate from February 1995 to August 1996. He has published one book on CFDTD software and two FDTD books: Conformal Finite-Difference Time-Domain Maxwell's Equations Solver: Software and User's Guide (Artech House, 2003), Parallel Finite-Difference Time-Domain (CUC Press of China, 2005, in Chinese) and Parallel Finite-Difference Time-Domain Method (Artech House, 2006). He has published over 100 technical papers and four book chapters. He developed and created the Computer and Communication Unlimited Company (http://www.2comu.com) and serves as its President. He is a Senior Member of the IEEE. He was included in Who's Who in America, Who's Who in Science and Engineering, and Who's Who in Education. He is also a visiting professor and Ph.D. Advisor of the Communication University of China. Yu's research interests include computational electromagnetic, numerical techniques, parallel computational techniques and the theory and design of parallel computing systems.

A Hybrid MoM-PO Method Combining ACA Technique for Electromagnetic Scattering from Target above a Rough Surface

J. Chen[1,2], M. Zhu[2], M. Wang[3], S. Li[2], and X. Li[2]

[1] Institute of Aviation Equipment,
Naval Academy of Armament, Shanghai, 200436, P. R. China
cjl21806780@163.com

[2] Department of Electronic and Information Engineering,
Naval Aeronautical Engineering Institute, Yantai, 264001, P. R. China

[3] Department of Ordnance Science and Technology,
Naval Aeronautical Engineering Institute, Yantai, 264001, P. R. China

Abstract **─** In this paper, an efficient hybrid method of moments (MoM)-physical optics (PO) method combining adaptive cross approximation (ACA) technique is applied to calculate the electromagnetic scattering from three-dimensional (3-D) target and rough surface composite model. The current on the rough surface is obtained through the PO approximation, while the current on the target surface is obtained through the MoM. Furthermore, an ACA technique is used to accelerate the coupling interaction between the target and the rough surface. Numerical results demonstrate that the memory and time cost can be substantially reduced without losing precision by applying the hybrid method, and which can be used to analyze large scale target/rough surface scattering problems.

Index Terms **–** Adaptive cross approximation (ACA), electromagnetic scattering, and MoM-PO, rough surface.

I. INTRODUCTION

The electromagnetic scattering calculation of target and rough surface composite model has been applied in the fields of radar surveillance, microwave remote sensing, target recognition and target tracking extensively [1-6]. The solutions of the composite scattering problems are complicated but practical.

Some numerical methods have been developed for three-dimensional (3-D) target/rough surface scattering problems, e.g., the finite-difference time-domain (FDTD) algorithm [7-8], a hybrid Kirchhoff approximation (KA)-method of moments (MoM) algorithm [9], multilevel UV method [10-11], the MoM using higher order basis functions [12], the hybrid MoM-physical optics (PO) method [13], most of which are based on the MoM.

The conventional MoM yields a dense complex linear system, which is a serious handicap especially for electrically large scattering problems. Some hybrid methods such as MoM-PO [13-14] are applied to reduce the computation time and memory requirement substantially, while the results are in reasonable agreement with those based on an application of the MoM alone.

In [15], an adaptive cross approximation (ACA) algorithm is used to accelerate MoM computations of electromagnetic compatibility (EMC) problems. It takes advantage of the rank-deficient character of the coupling matrix blocks representing well-separated MoM interactions [16-18]. The ACA algorithm has several important advantages over the multilevel fast multipole algorithm (MLFMA) [19-25]. The beauty of the ACA algorithm is its purely algebraic characteristic. Thus, the development and implementation of ACA algorithm do not depend on the complete knowledge of the integral

Submitted On: April 14, 2013
Accepted On: March 8, 2014

equation kernel, basis functions or the integral equation formulation itself. Moreover, due to its algebraic characteristic, ACA can be modular and very easily integrated into various MoM codes.

In this paper, an efficient hybrid MoM-PO method combining ACA technique is applied to calculate the electromagnetic scattering from 3-D target and rough surface composite model. Both the target and rough surface are assumed to be perfect electric conductor (PEC). Numerical results demonstrate that the memory and time cost can be substantially reduced without losing precision by applying the hybrid method, and which can be used to analyze large scale target/rough surface scattering problems.

II. FORMULATIONS

A. MoM-PO formulation

According to Fig. 1, the surface of the scattering body is split into a MoM-region and a PO-region, which correspond to a target and a rough surface, respectively. In principle, this subdivision can be performed in an arbitrary manner. We divide the scattering body in the manner aiming at making a tradeoff between solution accuracy and efficiency.

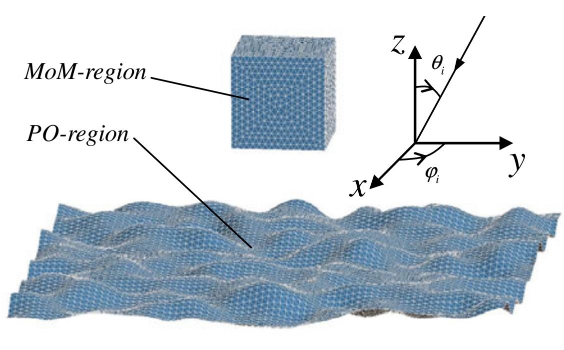

Fig. 1. Composite scattering model of target above a rough surface.

The surface currents of MoM-region and PO-region can be expanded by RWG basis function, written as,

$$\mathbf{J}^{\mathrm{MoM}} = \sum_{n=1}^{N^{MoM}} \alpha_n \mathbf{f}_n \tag{1}$$

$$\mathbf{J}^{\mathrm{PO}} = \sum_{k=1}^{N^{PO}} \beta_k \mathbf{f}_k \,, \tag{2}$$

where N^{MoM} and N^{PO} denote the number of unknowns in MoM-region and PO-region respectively, α_n and β_k are expansion coefficients of $\mathbf{f}_n$ and $\mathbf{f}_k$, both of which are RWG basis functions [26].

In the hybrid MoM-PO method, the relationship between the current in PO-region, the incident field, the current in MoM-region could be expressed as,

$$\mathbf{J}^{\mathrm{PO}}(\mathbf{r}) = 2\hat{\mathbf{n}}\times\mathbf{H}^{inc}(\mathbf{r}) + \sum_{n=1}^{N^{MoM}} 2\alpha_n \hat{\mathbf{n}}\times L^H \mathbf{f}_n \tag{3}$$

where $\mathbf{H}^{inc}(\mathbf{r})$ denotes the incident magnetic field, L^H is the magnetic field integral operator and $L^H\mathbf{f}_\mathbf{n} = \nabla\times\iint_{S'} \mathbf{f}_\mathbf{n}(\mathbf{r}')\cdot g(\mathbf{r},\mathbf{r}')dS'$, here $g(\mathbf{r},\mathbf{r}') = e^{-jk|\mathbf{r}-\mathbf{r}'|}/4\pi|\mathbf{r}-\mathbf{r}'|$, the Green's function of free space, $\mathbf{r}'$ and $\mathbf{r}$ denote the locations of source and observation point, respectively, $\hat{\mathbf{n}}$ denotes the unit outward normal vector of the conductor surface.

In order to get the expansion coefficient β_k , the two unit vectors $\hat{\mathbf{t}}_k^{\pm}$ are introduced in the middle of the kth edge. The $\hat{\mathbf{t}}_k^{\pm}$ are respectively lying in the plane of the triangles $\mathrm{T}_k^{\pm}$ defined by the kth edge, and perpendicular to the kth edge. As shown in Fig. 2, $\mathbf{f}_k(\mathbf{r}_k)\cdot\hat{\mathbf{t}}_k^{\pm} = 1$ is valid when the point $\mathbf{r}_k$ is in the middle of the kth edge.

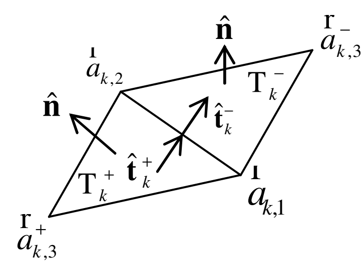

Fig. 2. The kth edge with two adjacent triangles T_k^+ and T_k^-.

Multiplying both sides of equation (2) with $\frac{1}{2}(\hat{\mathbf{t}}_k^+ + \hat{\mathbf{t}}_k^-)$ and inserting equation (3) in the resulting equation lead to,

$$\beta_k = \tau_k + \sum_{n=1}^{N^{MoM}} \alpha_n \cdot \tau_{n,k} \,, \tag{4}$$

where $\tau_k = (\hat{\mathbf{t}}_k^- + \hat{\mathbf{t}}_k^+) \cdot (\hat{\mathbf{n}} \times \mathbf{H}^{inc}(\mathbf{r}))$ and $\tau_{n,k} = (\hat{\mathbf{t}}_k^- + \hat{\mathbf{t}}_k^+) \cdot (\hat{\mathbf{n}} \times L^H \mathbf{f}_n)$.

For the MoM-region, the electric field integral equation (EFIE) could be written as,

$$(L^E \mathbf{J}^{\mathrm{MoM}})_{\tan} + (L^E \mathbf{J}^{\mathrm{PO}})_{\tan} = -\mathbf{E}_{\tan}^{inc} \quad (5)$$

where L^E is electric field integral operator and $L^E \mathbf{J} = jk_0 \eta_0 \iint_{S'} \left(\bar{\mathbf{I}} + \frac{\nabla\nabla}{k_0^2} \right) g(\mathbf{r}, \mathbf{r}') \cdot \mathbf{J} dS'$, here k_0 and η_0 are the wave number and the wave impedance of free space, $\mathbf{E}^{inc}$ is the incident electric field.

Finally, inserting equations (1), (2), and (4) into equation (5) results in,

$$\sum_{n=1}^{N^{MoM}} \alpha_n \left[L^E \mathbf{f}_n + \sum_{k=1}^{N^{PO}} \tau_{n,k} \cdot L^E \mathbf{f}_k \right]_{\tan} = -\mathbf{E}_{\tan}^{inc} - \sum_{k=1}^{N^{PO}} \tau_k \cdot (L^E \mathbf{f}_k)_{\tan} \quad . \quad (6)$$

Testing equation (6) with RWG basis functions in MoM-region, we can achieve the matrix equation expressed as,

$$(Z^{MoM} + Z^{MoM,PO} \cdot \tau') I^{MoM} = V - Z^{MoM,PO} \cdot \tau \quad (7)$$

where the Z^{MoM}, $Z^{MoM,PO}$, τ' are $N^{MoM} \times N^{MoM}$, $N^{MoM} \times N^{PO}$, $N^{PO} \times N^{MoM}$ complex matrix respectively, I^{MoM} and V are vectors of size N^{MoM}, τ is vector of size N^{PO}. The matrix elements are written as,

$$Z_{mn}^{MoM} = \left\langle \mathbf{f}_m, L^E \mathbf{f}_n \right\rangle \quad (8)$$

$$I_n^{MoM} = a_n, \quad (9)$$

$$V_m = -\left\langle \mathbf{f}_m, \mathbf{E}_{\tan}^{inc} \right\rangle, \quad (10)$$

$$Z_{mk}^{MoM,PO} = \left\langle \mathbf{f}_m, L^E \mathbf{f}_k \right\rangle, \quad (11)$$

$$\tau'_{kn} = (\hat{\mathbf{t}}_k^+ + \hat{\mathbf{t}}_k^-) g (\hat{\mathbf{n}} \times L^H \mathbf{f}_n), \quad (12)$$

$$\tau_k = (\hat{\mathbf{t}}_k^+ + \hat{\mathbf{t}}_k^-) g (\hat{\mathbf{n}} \times \mathbf{H}^{inc}(\mathbf{r})). \quad (13)$$

B. The application of ACA algorithm in MoM-PO

For the composite scattering problems of target above rough surface, the matrix $Z^{MM,PO}$ and τ' for interaction between MoM-region and PO-region have rank-deficient characters because the distance between source point and observation point is relatively far. The ACA algorithm fast achieves the low-rank decomposition form by using the rank-deficient character of matrix [15, 17]. The basic principle of ACA algorithm is as follow. The low-rank representation of a matrix could be got by the elements of partial rows and columns but not all the matrix elements. It means that by selecting right rows and columns, we can get the singular value decomposition form of the matrix approximately, so as to achieve the purpose of improving the computational efficiency.

Let the $m \times n$ rectangular matrix $Z^{m\times n}$ represent the interaction between two well-separated cubes. The ACA algorithm aims to approximate $Z^{m\times n}$ by $\tilde{Z}^{m\times n}$ in the following form,

$$\tilde{Z}^{m\times n} = U^{m\times r} V^{r\times n} = \sum_{i=1}^{r} u_i^{m\times 1} v_i^{1\times n} \quad (14)$$

where r is the effective rank of the matrix $Z^{m\times n}$. The goal of ACA is to achieve,

$$\| R^{m\times n} \|_F = \| Z^{m\times n} - \tilde{Z}^{m\times n} \|_F \le \varepsilon_{ACA} \| Z^{m\times n} \|_F \quad (15)$$

for a given tolerance ε_{ACA}, where R is termed as the error matrix, $\|\square\|_F$ denotes the matrix Frobenius norm. If $r \ll \min(m,n)$, the memory requirement will be reduced significantly from $m\times n$ to $(m+n)\times r$.

Selecting the value of the ε_{ACA} is very important. If the ε_{ACA} is too small, the computational cost will be high, while if the ε_{ACA} is too big, the computational accuracy will be low. Therefore, it is necessary to make a tradeoff. The more details of the ACA algorithm can be found in [15].

III. NUMERICAL EXAMPLES

In this section, several numerical examples are presented to illustrate the validity and efficiency of the proposed method. In these examples, the composite models are illuminated by tapered wave [27], which is employed to avoid rough surface edge scattering effects. The tapered wave is expressed as,

$$\mathbf{E}^{inc}(x,y,z) = \exp\left[-jk_0 (z\cos\theta_i + x\sin\theta_i\cos\phi_i + y\sin\theta_i\sin\phi_i)(1+\omega) \right] \exp(-t_x - t_y) \quad (16)$$

where

$$t_x = \frac{(x\cos\theta_i\cos\phi_i + y\cos\theta_i\sin\phi_i + z\sin\theta_i)^2}{g^2\cos^2\theta_i}, \quad (17)$$

$$t_y = \frac{(-x\sin\phi_i + y\cos\phi_i)^2}{g^2} \quad , \tag{18}$$

$$\omega = \frac{1}{k^2}\left(\frac{2t_x - 1}{g^2\cos^2\theta_i} + \frac{2t_y - 1}{g^2}\right) . \tag{19}$$

Here, θ_i and ϕ_i are the elevation angle and azimuth angle of the incident wave, while g is the parameter to control the width of the tapered wave. All the computations are performed on a PC with Intel Dual-core 3.1 GHz CPU and 8 GB RAM in double precision. The terminating tolerances of the ACA is set as $\varepsilon_{ACA} = 0.001$.

The relative residual error at the kth iteration is used for monitoring the convergence of the proposed method, which is defined as,

$$\varepsilon(V,k) = \frac{\| V - ZI^{(k)} \|_2}{\| V \|_2} \tag{20}$$

where $\|\square\|_2$ denotes the 2-norm of the complex vector. The iteration stops when the $\varepsilon(V, k)$ is less than 0.001.

As the first example, the composite scattering model of a PEC sphere above a PM spectrum rough surface is considered to test the validity of the proposed method. The mesh sizes of the sphere and the rough surface are set as 0.1λ and 0.15λ, respectively. The radius of the sphere is 0.5λ and the rough surface size is $24\lambda \times 24\lambda$, whose corresponding numbers of the unknowns are 930 and 76480. The height of the sphere center from rough surface is 2.0λ. The width of the tapered wave is 6.0λ. The incident wave is from Theta = 30° and Phi = 0°. A total number of 77410 unknowns are involved in this example. Figure 3 shows the RCS results (VV-Polarization) at Phi=0° computed by the proposed method and the conventional MoM-PO. It can be seen that both results are in good agreement. The computational cost of the first example is shown in Table I. By applying the proposed hybrid method, the memory requirement and the total CPU time are dramatically reduced compared to the conventional MoM-PO without losing precision.

Table I: Computational cost of the first example.

	Memory Requirement (GB)	CPU Time (s)
MoM-PO	1.165	1091
MoM-PO-ACA	0.171	885

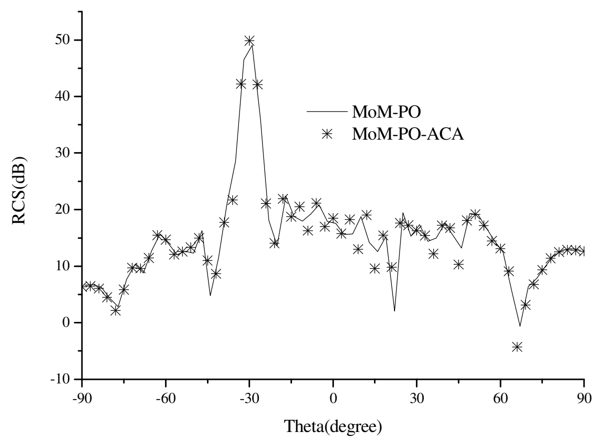

Fig. 3. Bistatic RCS of a PEC sphere above a PM spectrum rough surface.

The second example is a composite model of a missile above a Gaussian rough surface. This missile is a lying cylinder. The sizes of the missile and rough surface are $10.5\lambda\times2.0\lambda\times2.0\lambda$ and $20\lambda\times20\lambda$, respectively, and their distance is 10λ. The mesh sizes of the missile and the rough surface are set as 0.2λ and 0.125λ, and the corresponding numbers of the unknowns are 5760 and 76480. The width of the tapered wave is 5.0λ. The incident wave is from Theta=30° and Phi=0°. The root-mean-square height and correlation length of the rough surface are 0.1λ and $l_x = l_y = 1.0\lambda$, respectively. Figure 4 shows the RCS results (VV-Polarization) at Phi=0° computed by the proposed method, which agree well with the results computed by the conventional MoM-PO. Table II shows that the computational cost can be reduced significantly compared to the conventional MoM-PO.

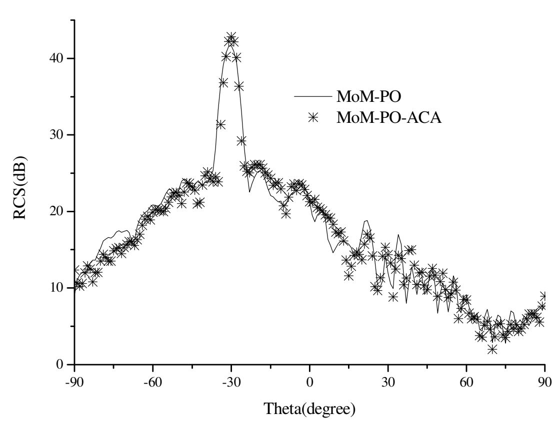

Fig. 4. Bistatic RCS of a missile above a Gaussian rough surface.

Table II: Computational cost of the second example.

	Memory Requirement(GB)	CPU Time
MoM-PO	6.817	>3 days
MoM-PO-ACA	0.74	1.5 hours

IV. NUMERICAL EXAMPLES

In this paper, a hybrid MoM-PO method combining ACA algorithm is applied to solving scattering from composite model of target and rough surface. Numerical examples have demonstrated that the memory requirement and CPU time can be significantly reduced without losing precision by applying the proposed method, and which can be used to analyze large scale target/rough surface scattering problems.

REFERENCES

[1] J. Johnson, “A numerical study of scattering from an object above a rough surface,” *IEEE Trans. Antennas Propag.*, vol. 50, no. 10, pp. 1361-1367, Oct. 2002.

[2] Y. Jin and Z. Li, “Numerical simulation of radar surveillance for the ship target and oceanic clutters in two-dimensional model,” *Radio Sci.*, vol. 38, no. 3, pp. 1045-1050, June 2003.

[3] P. Liu and Y. Jin, “Numerical simulation of bistatic scattering from a target at low altitude above rough sea surface under an EM-wave incidence at low grazing angle by using the finite element method,” *IEEE Trans. Antennas Propag.*, vol. 52, no. 5, pp. 1205-1210, May 2004.

[4] H. Ye and Y. Jin, “Fast iterative approach to difference scattering from the target above a rough surface,” *IEEE Trans. Geosci. Remote Sens.*, vol. 44, no. 1, pp. 108-115, Jan. 2006.

[5] Y. Jin and H. Ye, “Bistatic scattering from a 3D target above randomly rough surface,” *IEEE Int. Geosci. Remote Sens. Symp.*, pp. 57-60, 2007.

[6] H. Ye and Y. Jin, “A hybrid analytic-numerical algorithm of scattering from an object above a rough surface,” *IEEE Trans. Geosci. Remote Sens.*, vol. 45, no. 5, pp. 1174-1180, May 2007.

[7] L. Kuang and Y. Jin, “Bistatic scattering from a three-dimensional object over a randomly rough surface using the FDTD algorithm,” *IEEE Trans. Antennas Propag.*, vol. 55, no. 8, pp. 2302-2312, Aug. 2007.

[8] J. Li, L. Guo, and H. Zeng, “FDTD investigation on electromagnetic scattering from two-dimensional layered rough surfaces,” *Applied Computational Electromagnetics Society (ACES) Journal*, vol. 25, no. 5, pp. 450-457, May 2010.

[9] H. Ye and Y. Jin, “A hybrid KA-MoM algorithm for computation of scattering from a 3-D PEC target above a dielectric rough surface,” *Radio Sci.*, vol. 43, no. 3, pp. 56-70, June 2008.

[10] F. Deng, S. He, H. Chen, W. Hu, W. YU, and G. Zhu, “Numerical simulation of vector wave scattering from the target and rough surface composite model with 3-D multilevel UV method,” *IEEE Trans. Antennas Propag.*, vol. 58, no. 5, pp. 1625-1634, May 2010.

[11] C. Li, S. He, G. Zhu, Z. Zhang, F. Deng, B. Xiao, “A hybrid 3DMLUV-ACA method for scattering from a 3-D PEC object above a 2-D Gaussian dielectric rough surface,” *Applied Computational Electromagnetics Society (ACES) Journal*, vol. 27, no. 12, pp. 956-963, Dec. 2012.

[12] Y. An, R. Chen, P. Xu, Z. Liu, and L. Zha, “Analysis of composite scattering from a target above/below a dielectric rough surface using higher order basis functions,” *Applied Computational Electromagnetics Society (ACES) Journal*, vol. 27, no. 7, pp. 541-549, July 2012.

[13] U. Jakobus and F. Landstorfer, “Improved PO-MM hybrid formulation for scattering from three-dimensional perfectly conducting bodies of arbitrary shape,” *IEEE Trans. Antennas Propag.*, vol. 43, no. 2, pp. 162-169, Feb. 1995.

[14] H. Chen, G. Zhu, J. Luo, and F. Yuan, “A modified MoM-PO method for analyzing wire antennas near to coated PEC plates,” *IEEE Trans. Antennas and Propag.*, vol. 56, no. 6, pp. 1818-1822, June 2008.

[15] K. Zhao, M. Vouvakis, and J. Lee, “The adaptive cross approximation algorithm for accelerated method of moments computations of EMC problems,” *IEEE Trans. Electromagn. Compat.*, vol. 47, no. 4, pp. 763-773, Nov. 2005.

[16] M. Bebendorf, “Approximation of boundary element matrices,” *Numer. Math.*, vol. 86, no. 4, pp. 565-589, June 2000.

[17] S. Kurz, O. Rain, and S. Rjasanow, “The adaptive cross-approximation technique for the 3D boundary-element method,” *IEEE Trans. Magn.*, vol. 38, no. 2, pp. 421-424, Mar. 2002.

[18] M. Bebendorf and S. Rjasanow, “Adaptive low-rank approximation of collocation matrices,” *Computing*, vol. 70, no. 1, pp. 1-24, Mar. 2003.

[19] C. Lu and W. Chew, “A multilevel algorithm for solving boundary integral equations of wave scattering,” *Micro. Opt. Tech. Lett.*, vol. 7, no. 10, pp. 466-470, July 1994.

[20] J. Song, C. Lu, and W. Chew, “Multilevel fast multipole algorithm for electromagnetic scattering by large complex objects,” *IEEE Trans. Antennas Propag.*, vol. 45, no. 10, pp. 1488-1493, Oct. 1997.

[21] J. Chen, S. Li, and M. Wang, “Targets identification method based on electromagnetic

scattering analysis," *2011 IEEE CIE International Conference on Radar*, vol. 2, pp. 1647-1651, Oct. 2011.

[22] J. Chen, S. Li, and Y. Song, "Analysis of electromagnetic scattering problems by means of a VSIE-ODDM-MLFMA method," *Applied Computational Electromagnetics Society (ACES) Journal*, vol. 27, no. 8, pp. 660-667, Aug. 2012.

[23] J. Chen, M. Wang, S. Li, M. Zhu, J. Yu, and X. Li, "An IE-ODDM scheme combined with efficient direct solver for 3D scattering problems" *Micro. Opt. Tech. Lett.*, vol. 55, no. 9, pp. 2027-2033, Sep. 2013.

[24] M. Li, H. Chen, C. Li, R. Chen, and C. Ong, "Hybrid UV/MLFMA analysis of scattering by PEC targets above a lossy half-space," *Applied Computational Electromagnetics Society (ACES) Journal*, vol. 26, no. 1, pp. 17-25, Jan. 2011.

[25] H. Zhao, J. Hu, and Z. Nie, "Parallelization of MLFMA with composite load partition criteria and asynchronous communication," *Applied Computational Electromagnetics Society (ACES) Journal*, vol. 25, no. 2, pp. 167-173, Feb. 2010.

[26] S. Rao, D. Wilton, and A. Glisson, "Electromagnetic scattering by surface of arbitrary shape," *IEEE Trans. Antennas Propag.*, vol. 30, no. 3, pp. 409-418, May 1982.

[27] H. Ye and Y. Jin, "Parameterization of the tapered incident wave for numerical simulation of electromagnetic scattering from rough surface," *IEEE Trans. Antennas Propag.*, vol. 53, no. 3, pp. 1234-1237, Mar. 2005.

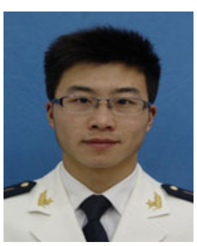

Jialin Chen was born in Leshan, Sichuan, the People's Republic of China in 1986. He received his B.Sc. degree in radar engineering, M.Sc. degree in electromagnetic field and microwave technique and Ph.D. degree in information and communication engineering from Department of Electronic and Information Engineering, Naval Aeronautical Engineering Institute, Yantai, China, in 2007, 2009 and 2013, respectively. He is currently working as engineer at Naval Academy of Armament. His current research interests include computational electromagnetics, antennas, electromagnetic scattering and propagation, and radar target recognition.

Mingbo Zhu was born in Shandong, P. R. China in 1971. He received his Ph.D. degree from National University of Defence Technology in 1999. He is currently working as Associate Professor at Naval Aeronautical Engineering Institute. His research interests mainly include microwave remote sensing, electromagnetic scattering and radiation, radar target recognition.

Min Wang was born in Dongyang, Zhejiang, the People's Republic of China. He is currently working toward the Ph.D. degree at Naval Aeronautical Engineering Institute. His current research interests include electromagnetic launch, computational electromagnetics, electromagnetic scattering and propagation, and radar target recognition.

Shangsheng Li was born in Shandong, P. R. China in 1965. He received his B.Sc. degrees from Southeast University and M.Sc. degree from Nanjing University of Aeronautics and Astronautics, in 1987 and 1996, respectively. Now he is a Professor of Naval Aeronautical Engineering Institute. His research interests mainly include microwave/millimeter-wave systems, antenna, and computational electromagnetics.

Xiangping Li was born in Shandong, P. R. China in 1963. He is currently working as Professor at Naval Aeronautical Engineering Institute. His research interests mainly include radar target recognition, radar target tracking, computational electromagnetics, and microwave/millimeter-wave systems.

Null Broadening and Sidelobe Control Algorithm via Multi-Parametric Quadratic Programming for Robust Adaptive Beamforming

Fulai Liu [1], Guozhu Sun [2], Jinkuan Wang [1] and Ruiyan Du [1]

[1] Engineering Optimization & Smart Antenna Institute
Northeastern University at Qinhuangdao, 066004, China
fulailiu@126.com, ruiyandu@126.com

[2] Department of Neurosurgery
The Second Hospital of Hebei Medical University, Shijiazhuang 050000, China
sungzh705@sohu.com

Abstract **─** Adaptive beamforming algorithm can automatically optimize the array pattern by adjusting the elemental control weights until a prescribed objective function is satisfied. Unfortunately, it is possible that the mismatch occurs between adaptive weights and data, due to the perturbation of the interference location when the antenna platform vibrates or interference moves quickly. Besides, the traditional beamformers may have unacceptably high sidelobes when few samples are available. To solve these problems, an effective robust adaptive beamforming method is presented. In the proposed method, firstly, a tapered covariance matrix is constructed to broaden the width of nulls for interference signal sources. Secondly, multiple additional quadratic inequality constraints outside the mainlobe beampattern area are used to guarantee that the sidelobe level is strictly lower than the prescribed threshold value. Finally, the beamforming optimization problem is formulated as a multi-parametric quadratic programming problem, such that the optimal weight vector can be easily obtained by real-valued computation. Simulation results are shown to demonstrate the efficiency of the proposed approach.

Index Terms **─** Covariance Matrix Taper (CMT), multi-parametric Quadratic Programming (mp-QP), null broadening, robust adaptive beamforming and sidelobe control.

I. INTRODUCTION

Adaptive beamforming has been found in numerous applications from radar, sonar, wireless communications, seismology and microphone arrays. One of the most popular approaches to adaptive beamforming is the so-called Minimum Variance Distortionless Response (MVDR) processor, which minimizes the array output power while maintaining a distortionless mainlobe response toward the desired signal [1]. However, most of the conventional adaptive beamformers, such as MVDR, etc., may have unacceptably low and narrow null level in the interference direction or high sidelobes in the case of low sample support. In adaptive array systems, these may lead to significant performance degradation in the case of unexpected interference signals.

Several approaches of null broadening technique have been proposed. For example, the null broadening technique originally [2-3] is developed for robust beamforming. It is generalized by the concept of a "Covariance Matrix Taper (CMT)" [4]. A multi-parametric quadratic programming method is presented to control the null level of adaptive antenna array [5]. In the proposed method, the optimal weight vector can be easily obtained by real-valued computation. Unfortunately the sidelobe level is not controlled efficiently. A null broadening technique based on reduced rank conjugate gradient algorithm is proposed in [6]. It can obtain better performance

Submitted On: January 22, 2013
Accepted On: April 5, 2014

even if few samples are available. The space-time averaging techniques and rotation techniques of the steering vectors are utilized in [7] to improve the performance of null level, so that it can provide increased robustness against the mismatch problem, as well as control over the sidelobe level. A robust beamforming control method based on semidefinite programming is presented to broaden null of adaptive antenna array [8]. The presented method can provide an improved robustness against the interference angle shaking and suppress the interference signals. An effective approach based on genetic algorithm is presented in [9]. In order to minimize the total output power and place nulls in the jammers, the presented approach exploits genetic algorithm to adjust some of the least significant bits of the beam steering phase shifters and amplitude weights. In [10], particle swarm optimization technique is used to obtain optimal null levels for the symmetric linear antenna array. By the linearization of the transmit model with Taylor expansion, a fast broad null beamforming technology [11] is presented and the application of the broad null transmitting beamforming technology for the radar in anti-ARM battle is studied. A null steering beamforming algorithm is proposed to cancel unwanted signals by steering nulls of the pattern in the direction of high interference without affecting the main beam [12].

To control sidelobe, several approaches have been proposed [13-16]. A modified MVDR beamformer is presented by multiple additional quadratic inequality constraints outside the mainlobe beampattern area [13]. These constraints can guarantee that the beampattern sidelobe level remains lower than a certain prescribed value. An improved adaptive beamforming technique [14] is proposed by an adaptive dispersion invasive weed optimization. It can not only provide sufficient steering ability regarding the mainlobe and the nulls, but also work faster than the particle swarm optimization. An iterative beamforming method is proposed for sensor array with arbitrary geometry and element directivity [15]. By solving the linearly constrained least squares problem, it can effectively control the sidelobe level. Making use of multi-linear constrained minimum variance repetitiously, a low sidelobe beamforming method is presented in [16]. By searching the previously formed beampattern, the location of the highest sidelobe is found and the corresponding direction vector is added to the constrained conditions of multi-linear constrained minimum variance algorithm to receive the new weight value.

In this paper, an effective adaptive beamforming method is proposed to resolve null broadening and sidelobe control problem. Firstly, an approximation of sinc function is used to broaden null. It can be regarded as adding the coherent signals to each signal source but with two different directions, and it can place nulls in a certain range of angles instead of certain points. Secondly, multiple quadratic inequality constraints outside the mainlobe beampattern area are used to control sidelobe. These constraints can guarantee that the beampattern sidelobe level remains lower than a certain prescribed value. Thirdly, the beamforming control problem is formulated as a multi-parametric Quadratic Programming (mp-QP) problem, such that the optimal weight vector can be obtained by real-valued computation.

This paper is organized as follows. section 2 briefly introduces the signal model and presents the MVDR solution. The methods of null broadening and sidelobe control are addressed in section 3. Section 4 gives the algorithm formulation. In section 5, simulation results are presented to verify the performance of the proposed approach. Section 6 concludes the paper.

II. BACKGROUND

Consider a Uniform Linear Array (ULA), which consists of M elements. The beamformer output of the ULA at time t is given by:

$$y(t) = \boldsymbol{w}^{\mathrm{H}}\boldsymbol{x}(t),$$

where $\boldsymbol{w} = [w_1, w_2, \ldots, w_M]^{\mathrm{T}}$ is the complex-valued weight vector. The superscripts $(\cdot)^{\mathrm{T}}$ and $(\cdot)^{\mathrm{H}}$ denote the transpose and conjugate transpose of a matrix, respectively. The $M \times 1$ vector of array observations $\boldsymbol{x}(t) = [x_1(t), x_2(t), \ldots, x_M(t)]^{\mathrm{T}}$ is given by:

$$\begin{aligned}\boldsymbol{x}(t) &= \boldsymbol{s}(t) + \boldsymbol{i}(t) + \boldsymbol{n}(t)\\ &= s(t)\boldsymbol{a}(\theta_0) + \sum_{j=1}^{J} i_j(t)\boldsymbol{a}(\theta_j) + \boldsymbol{n}(t),\end{aligned}$$

where J is the number of interference signals. $s(t)$ and $i_j(t)$ stand for the signal and interference, respectively. The signal and interference Directions of Arrival (DOAs) are θ_0 and

θ_j $(j=1,\dots,J)$, respectively, with corresponding steering vectors $\boldsymbol{a}(\theta_0)$ and $\boldsymbol{a}(\theta_j)$. $\boldsymbol{n}(t)=[n_1(t),\dots,n_M(t)]^{\mathrm{T}}$ with $n_i(t)$ denoting the additive noise of the ith sensor.

Let $\boldsymbol{R}$ denote the $M\times M$ theoretical covariance matrix of the array snapshot vector. Assume that $\boldsymbol{R}$ is a positive definite matrix with the following form:

$$\boldsymbol{R}=\sigma_0^2\boldsymbol{a}(\theta_0)\boldsymbol{a}^{\mathrm{H}}(\theta_0)+\sum_{j=1}^{J}\sigma_j^2\boldsymbol{a}(\theta_j)\boldsymbol{a}^{\mathrm{H}}(\theta_j)+\sigma_n^2\boldsymbol{I}_M,$$

where σ_0^2, σ_j^2 $(j=1,\dots,J)$ and σ_n^2 are the powers of the uncorrelated impinging signals $s(t)$, $i_j(t)$ and noise, respectively. $\boldsymbol{I}_M$ is the $M\times M$ identity matrix. The common formulation of the beamforming problem that leads to the MVDR beamformer is described below. First determine the $M\times 1$ vector $\boldsymbol{w}_0$ as the solution to the following linearly constrained quadratic problem,

$$\min_{\boldsymbol{w}} \boldsymbol{w}^{\mathrm{H}}\boldsymbol{R}\boldsymbol{w} \quad \text{subject to } \boldsymbol{w}^{\mathrm{H}}\boldsymbol{a}(\theta_0)=1. \tag{1}$$

Then the solution of equation (1) for this particular case can be given as:

$$w_{\mathrm{MVDR}}=\frac{\boldsymbol{R}^{-1}\boldsymbol{a}(\theta_0)}{\boldsymbol{a}^{\mathrm{H}}(\theta_0)\boldsymbol{R}^{-1}\boldsymbol{a}(\theta_0)}. \tag{2}$$

In practice, the exact covariance matrix is not available and is replaced by the sample covariance matrix $\hat{\boldsymbol{R}}$,

$$\hat{\boldsymbol{R}}=\frac{1}{N}\sum_{k=1}^{N}\boldsymbol{x}(k)\boldsymbol{x}^{\mathrm{H}}(k), \tag{3}$$

where N denotes the number of snapshots.

III. ADAPTIVE BEAMFORMING WITH NULL BROADENING AND SIDELOBE CONTROL

In this section, we firstly introduce the null broadening method to widen the nulling extent and control the nulling level. Secondly, multiple quadratic inequality constraints are derived to control sidelobe level. Finally, the modified CMT-MVDR problem is given.

A. Null broadening

1. Null extent control: Assume that the narrowband interference signals impinging on the array are uncorrelated with each other as well as with the spatially white noise. According to [2], the terms in the covariance matrix $\boldsymbol{R}$ for a one-dimensional array are given as:

$$R_{mn}=N_n\delta(m,n)+\sum_j\sigma_j^2 e^{j\frac{2\pi}{\lambda}(x_m-x_n)u_j},$$

where x_m is the location of the mth element. N_n is the noise power in the nth channel and $\delta(m,n)$ is a Kronecker delta function. The sum is performed over all interference signals with averaged power σ_j^2 and direction cosines $u_j=\sin\theta_j$, for θ_j measured from the broadside. According to [2], we construct a cluster of q equal-power incoherent signals around each original interfering signal to produce a notch of width W in each of the interference directions. In this case, the additional sources can be summed in closed form, as geometric sum and can be written as:

$$\sum_{k=1}^{q}(\sigma_j^2/q)e^{j\frac{2\pi}{\lambda}(x_m-x_n)(u_j+k\delta)}=\frac{\sin(q\Lambda_{mn})}{q\sin(\Lambda_{mn})}\sigma_j^2 e^{j\frac{2\pi}{\lambda}(x_m-x_n)u_j},$$

where $\Lambda_{mn}=\dfrac{\pi(x_m-x_n)\delta}{\lambda}$ and $\delta=\dfrac{W}{q-1}$. Since there is no angle dependence in the sinc function. A new covariance matrix term is given as $\tilde{R}_{mn}=R_{mn}\dfrac{\sin(q\Lambda_{mn})}{q\sin(\Lambda_{mn})}$. In matrix form, the CMT can be expressed as:

$$\tilde{\boldsymbol{R}}=\boldsymbol{R}\circ\boldsymbol{T}_{Mai}, \tag{4}$$

where "$\circ$" represents Hadamard product, that is multiplying the corresponding elements of the two matrixes and the form of matrix $\boldsymbol{T}_{Mai}$ is:

$$T_{mn}=(\sin(q\pi\delta(m-n)/2))/(q\sin(\pi\delta(m-n)/2)).$$

2. Null level control: Assume that the interference signal arrivals the received array from the angle of incident $\theta_p,(p=1,\dots,P)$. When the interference moves quickly, it is possible that the mismatch occurs for adaptive weight and data, due to the perturbation of the interference location. Let $\Delta\theta$ denote the angle spread for the interference signal, which comes from θ_p. Let $\theta_k\in[\theta_p-\Delta\theta,$ $\theta_p+\Delta\theta]$ $(k=1,\cdots,K)$ be chosen grid that approximates the angle spread area. To control the null level for the angle spread area $[\theta_p-\Delta\theta,\theta_p+\Delta\theta]$, we use the following multiple quadratic inequality constraints inside the angle spread area:

$$\left|\boldsymbol{w}^{\mathrm{H}}\boldsymbol{a}(\theta_k)\right|^2 \le \xi^2,\ \ k=1,\ldots,K, \tag{5}$$

where ξ^2 is the prescribed null level.

B. Sidelobe control

Let $\theta_l \in \Theta (l=1,\ldots,L)$ be a chosen grid that approximates the sidelobe beampattern areas Θ using a finite number of angles. To control the sidelobe level, we use the following multiple quadratic inequality constraints outside the mainlobe beampattern area:

$$\left|\boldsymbol{w}^{\mathrm{H}}\boldsymbol{a}(\theta_l)\right|^2 \le \varepsilon^2,\ \ k=1,\ldots,L, \tag{6}$$

where ε^2 is the prescribed sidelobe level.

C. The modified CMT-MVDR

Adding the constraints (5) and (6) to the MVDR beamforming problem (1) and using the new tapered covariance matrix (4) instead of the sample covariance matrix (3), we obtain the following modified CMT-MVDR problem:

$$\begin{aligned}\min_{\boldsymbol{w}} \boldsymbol{w}^{\mathrm{H}}\tilde{\boldsymbol{R}}\boldsymbol{w} \text{ subject to } \quad & \boldsymbol{w}^{\mathrm{H}}\boldsymbol{a}(\theta_0)=1\\ & \left|\boldsymbol{w}^{\mathrm{H}}\boldsymbol{a}(\theta_k)\right|^2 \le \xi^2 \qquad (7)\\ & \left|\boldsymbol{w}^{\mathrm{H}}\boldsymbol{a}(\theta_l)\right|^2 \le \varepsilon^2,\end{aligned}$$

where $k=1,\ldots,K$ and $l=1,\ldots,L$.

Notice that $\left|\boldsymbol{w}^{\mathrm{H}}\boldsymbol{a}(\theta_k)\right|^2$ can directly determine the output power of antenna array at the interference direction θ_k (refer to equation (17)), thus, it can be viewed as the "directional gain" of the antenna array.

In the next section, we will convert this problem (7) to an mp-QP problem, such that the optimal weight vector is estimated by the real-valued computation.

IV. ALGORITHM FORMULATION

A. CMT-mp-QP MVDR

In this section, we present the multi-parametric programming problem for covariance matrix taper MVDR beamformer, named as CMT-mp-QP MVDR. As seen in problem (7), the data is in general complex valued. However, for convenience, we will work with real-valued data. To do so, a pre-processing path is taken prior to the beamforming operation.

Let

$$\begin{aligned}\boldsymbol{R}_1 &= \mathrm{Real}\{\tilde{\boldsymbol{R}}\}, \quad \boldsymbol{R}_2 = \mathrm{Imag}\{\tilde{\boldsymbol{R}}\},\\ \boldsymbol{w}_1 &= \mathrm{Real}\{\boldsymbol{w}\}, \quad \boldsymbol{w}_2 = \mathrm{Imag}\{\boldsymbol{w}\},\\ \boldsymbol{a}_{01}(\theta_0) &= \mathrm{Real}\{\boldsymbol{a}(\theta_0)\}, \quad \boldsymbol{a}_{02}(\theta_0) = \mathrm{Imag}\{\boldsymbol{a}(\theta_0)\},\\ \boldsymbol{a}_{k1}(\theta_k) &= \mathrm{Real}\{\boldsymbol{a}(\theta_k)\}, \quad \boldsymbol{a}_{k2}(\theta_k) = \mathrm{Imag}\{\boldsymbol{a}(\theta_k)\},\\ \boldsymbol{a}_{l1}(\theta_l) &= \mathrm{Real}\{\boldsymbol{a}(\theta_l)\}, \quad \boldsymbol{a}_{l2}(\theta_l) = \mathrm{Imag}\{\boldsymbol{a}(\theta_l)\},\end{aligned}$$

where $k=1,\ldots,K$ and $l=1,\ldots,L$. $\mathrm{Real}\{\cdot\}$ and $\mathrm{Imag}\{\cdot\}$ stand for the real and imaginary part of a complex matrix or vector, respectively.

By simple algebra, the cost function $\boldsymbol{w}^{\mathrm{H}}\tilde{\boldsymbol{R}}\boldsymbol{w}$ can be rewritten as:

$$\begin{aligned}\boldsymbol{w}^{\mathrm{H}}\tilde{\boldsymbol{R}}\boldsymbol{w} &= \mathrm{Real}\{\boldsymbol{w}^{\mathrm{H}}\tilde{\boldsymbol{R}}\boldsymbol{w}\} + j\mathrm{Imge}\{\boldsymbol{w}^{\mathrm{H}}\tilde{\boldsymbol{R}}\boldsymbol{w}\}\\ &= \begin{pmatrix}\boldsymbol{w}_1\\ \boldsymbol{w}_2\end{pmatrix}^{\mathrm{T}} \begin{pmatrix}\boldsymbol{R}_1 & -\boldsymbol{R}_2\\ \boldsymbol{R}_2 & \boldsymbol{R}_1\end{pmatrix}\begin{pmatrix}\boldsymbol{w}_1\\ \boldsymbol{w}_2\end{pmatrix} +\\ &\quad j\begin{pmatrix}\boldsymbol{w}_1\\ \boldsymbol{w}_2\end{pmatrix}^{\mathrm{T}} \begin{pmatrix}\boldsymbol{R}_2 & \boldsymbol{R}_1\\ -\boldsymbol{R}_1 & \boldsymbol{R}_2\end{pmatrix}\begin{pmatrix}\boldsymbol{w}_1\\ \boldsymbol{w}_2\end{pmatrix}.\end{aligned}$$

It is easy to know that $\mathrm{Imag}\{\boldsymbol{w}^{\mathrm{H}}\tilde{\boldsymbol{R}}\boldsymbol{w}\}=0$ since $(\boldsymbol{w}^{\mathrm{H}}\tilde{\boldsymbol{R}}\boldsymbol{w})^{\mathrm{H}} = \boldsymbol{w}^{\mathrm{H}}\tilde{\boldsymbol{R}}\boldsymbol{w} \in \mathbb{R}$ for $\forall \boldsymbol{w} \in \mathbb{C}^M$. Thus, the modified MVDR problem (7) can be reformulated as the following mp-QP problem:

$$\min_{\boldsymbol{z}} \frac{1}{2}\boldsymbol{z}^{\mathrm{T}}\boldsymbol{H}\boldsymbol{z} \text{ subject to } \boldsymbol{G}\boldsymbol{z} \le \boldsymbol{b}, \tag{8}$$

where the matrices and vectors in equation (8) have the following forms:

$$\begin{aligned}\boldsymbol{z} &= [\boldsymbol{w}_1^{\mathrm{T}}, \boldsymbol{w}_2^{\mathrm{T}}] \in \mathbb{R}^{2M},\\ \boldsymbol{H} &= \begin{pmatrix}\boldsymbol{R}_1 & -\boldsymbol{R}_2\\ \boldsymbol{R}_2 & \boldsymbol{R}_1\end{pmatrix} \in \mathbb{R}^{2M\times 2M},\\ \boldsymbol{G} &= [\boldsymbol{G}_0^{\mathrm{T}}, \boldsymbol{G}_1^{\mathrm{T}}, \ldots, \boldsymbol{G}_K^{\mathrm{T}}, \boldsymbol{G}_1^{\mathrm{T}}, \ldots, \boldsymbol{G}_L^{\mathrm{T}}]^{\mathrm{T}},\\ \boldsymbol{G}_k &= [\boldsymbol{B}_k^T, -\boldsymbol{B}_k^T]^T, \quad \boldsymbol{G}_l = [\boldsymbol{B}_l^T, -\boldsymbol{B}_l^T]^T,\\ \boldsymbol{B}_k &= \begin{bmatrix}\boldsymbol{a}_{k_1}^{\mathrm{T}}(\theta_k) & \boldsymbol{a}_{k_2}^{\mathrm{T}}(\theta_k)\\ \boldsymbol{a}_{k_2}^{\mathrm{T}}(\theta_k) & -\boldsymbol{a}_{k_1}^{\mathrm{T}}(\theta_k)\end{bmatrix},\\ \boldsymbol{B}_l &= \begin{bmatrix}\boldsymbol{a}_{l_1}^{\mathrm{T}}(\theta_l) & \boldsymbol{a}_{l_2}^{\mathrm{T}}(\theta_l)\\ \boldsymbol{a}_{l_2}^{\mathrm{T}}(\theta_l) & -\boldsymbol{a}_{l_1}^{\mathrm{T}}(\theta_l)\end{bmatrix},\\ \boldsymbol{b} &= [\boldsymbol{b}_0^{\mathrm{T}}, \boldsymbol{b}_1^{\mathrm{T}}, \ldots, \boldsymbol{b}_K^{\mathrm{T}}, \boldsymbol{b}_1^{\mathrm{T}}, \ldots, \boldsymbol{b}_L^{\mathrm{T}}]^{\mathrm{T}},\ \boldsymbol{b}_0 = [1,0,-1,0]^{\mathrm{T}},\\ \boldsymbol{b}_k &= [\sqrt{\lambda_\xi}\xi, \sqrt{1-\lambda_\xi}\xi, -\sqrt{\lambda_\xi}\xi, -\sqrt{1-\lambda_\xi}\xi]^{\mathrm{T}},\\ \boldsymbol{b}_l &= [\sqrt{\lambda_\varepsilon}\varepsilon, \sqrt{1-\lambda_\varepsilon}\varepsilon, -\sqrt{\lambda_\varepsilon}\varepsilon, -\sqrt{1-\lambda_\varepsilon}\varepsilon]^{\mathrm{T}},\end{aligned}$$

where $k=1,\ldots,K$ and $l=1,\ldots,L$. λ_ξ and $\lambda_\varepsilon\in[0,1]$. The matrix $\boldsymbol{H}$ is a positive definite matrix.

B. The optimal solution

As shown in [17] and [18], CMT-mp-QP problem (8) can be solved by applying the Karush-Kuhn-Tucker (KKT) conditions,

$$\boldsymbol{Hz}+\boldsymbol{G}^{\mathrm{T}}\boldsymbol{\lambda}=\boldsymbol{0},\quad \boldsymbol{\lambda}\in\mathbb{R}^{4(K+1)}, \tag{9}$$

$$\lambda_i\boldsymbol{G}^i\boldsymbol{z}-\boldsymbol{b}^i=0,\quad i=1,\ldots,4(K+1), \tag{10}$$

$$\boldsymbol{\lambda}\geq\boldsymbol{0}, \tag{11}$$

$$\boldsymbol{Gz}-\boldsymbol{b}\leq\boldsymbol{0}. \tag{12}$$

In the sequel, let the superscript index denote a subset of the rows of a matrix or vector. Since $\boldsymbol{H}$ has full rank, equation (9) gives:

$$\boldsymbol{z}=-\boldsymbol{H}^{-1}\boldsymbol{G}^{\mathrm{T}}\boldsymbol{\lambda}. \tag{13}$$

Definition 1: Let $\boldsymbol{z}^*$ be the optimal solution to problem (8). We define active constraints the constraints with $\boldsymbol{G}^i\boldsymbol{z}-\boldsymbol{b}^i=0$ and inactive constraints the constraints with $\boldsymbol{G}^i\boldsymbol{z}-\boldsymbol{b}^i<0$. The optimal active set $A^*=\left\{i\middle|\boldsymbol{G}^i\boldsymbol{z}^*=\boldsymbol{b}^i\right\}$.

Definition 2: For an active set, we say that the Linear Independence Constraint Qualification (LICQ) holds if the set of active constraint gradients are linearly independent, i.e., $\boldsymbol{G}^A$ has full row rank.

Assuming that LICQ holds, equation (10) and equation (13) lead to:

$$\boldsymbol{\lambda}^A=-(\boldsymbol{G}^A\boldsymbol{H}^{-1}(\boldsymbol{G}^A)^{\mathrm{T}})^{-1}\boldsymbol{b}^A. \tag{14}$$

Equation (14) can now be substituted into equation (13) to obtain:

$$\boldsymbol{z}=\boldsymbol{H}^{-1}(\boldsymbol{G}^A)^{\mathrm{T}}(\boldsymbol{G}^A\boldsymbol{H}^{-1}(\boldsymbol{G}^A)^{\mathrm{T}})^{-1}\boldsymbol{b}^A. \tag{15}$$

Partition, now, the vector $\boldsymbol{z}$ into $\boldsymbol{z}_1,\boldsymbol{z}_2\in\mathbb{R}^M$, by $\boldsymbol{z}=[\boldsymbol{z}_1\ \boldsymbol{z}_2]^{\mathrm{T}}$ and define $\boldsymbol{w}_0$ as follows:

$$\boldsymbol{w}_0=\boldsymbol{z}_1+j\boldsymbol{z}_2\in\mathbb{C}^M. \tag{16}$$

It is clear that the optimal solution of problem (7) for this particular case is $\boldsymbol{w}_0$.

Summary of the proposed algorithm

1. Collect the sample data and estimate the covariance matrix $\hat{\boldsymbol{R}}=\dfrac{1}{N}\sum_{k=1}^{N}\boldsymbol{x}(k)\boldsymbol{x}^{\mathrm{H}}(k)$.

2. Modify the sample covariance matrix using the CMT matrix $\boldsymbol{T}$, $\hat{\boldsymbol{R}}=\hat{\boldsymbol{R}}\circ\boldsymbol{T}$.

3. Add the constrains of null level control $\left|\boldsymbol{w}^{\mathrm{H}}\boldsymbol{a}(\theta_k)\right|^2\leq\xi^2,(k=1,\ldots,K)$ and sidelobe level control $\left|\boldsymbol{w}^{\mathrm{H}}\boldsymbol{a}(\theta_l)\right|^2\leq\varepsilon^2,(l=1,\ldots,L)$ to the MVDR beamformer (1).

4. Calculate the modified CMT-MVDR beamforming optimization problem (7) using multi-parametric quadratic programming method.

C. Output SINR and array gain

To investigate the performance of the proposed method, this section gives the definitions of Signal-to-Interference-and-Noise Ratio (SINR) and array gain for an adaptive antenna array system. From $y(k)=\boldsymbol{w}^{\mathrm{H}}\boldsymbol{x}(k)$, the mean square power output of the beamformer can be expressed as:

$$\begin{aligned}P&=\mathrm{E}\left\{\left|y(k)\right|^2\right\}=\sigma_0^2\left|\boldsymbol{w}^{\mathrm{H}}\boldsymbol{a}(\theta_0)\right|^2+\boldsymbol{w}^{\mathrm{H}}\mathbf{R}_{j+n}\boldsymbol{w}\\&=\sigma_0^2\left|\boldsymbol{w}^{\mathrm{H}}\boldsymbol{a}(\theta_0)\right|^2+\sum_{j=1}^{J}\sigma_j^2\left|\boldsymbol{w}^{\mathrm{H}}\boldsymbol{a}(\theta_j)\right|^2+\sigma_n^2\boldsymbol{w}^{\mathrm{H}}\boldsymbol{\rho}_n\boldsymbol{w},\end{aligned} \tag{17}$$

where $\mathrm{E}\{\cdot\}$ denotes the statistical expectation. The $M\times M$ interference-plus-noise covariance matrix $\boldsymbol{R}_{j+n}$ is expressed as:

$$R_{j+n}=\mathrm{E}\{\boldsymbol{pp}^{\mathrm{H}}\}=\sum_{j=1}^{J}\sigma_j^2\boldsymbol{a}(\theta_j)\boldsymbol{a}^{\mathrm{H}}(\theta_j)+\sigma_n^2\boldsymbol{\rho}_n,$$

where $\boldsymbol{p}=\sum_{j=1}^{J}\boldsymbol{i}_j(k)\boldsymbol{a}(\theta_j)+\boldsymbol{n}(k)$ and σ_0^2 is the desired signal power. σ_j^2 $(j=1,\ldots J)$ and σ_n^2 are the interference signal power and noise power, respectively. $\boldsymbol{\rho_n}$ is the Hermitian cross-spectral density matrix of the noise normalized to have its trace equals to M .

SINR is defined as follows:

Definition 3: For an adaptive antenna array system, SINR is defined as the output signal power divided by the output interference-and-noise power and is given by:

$$\mathrm{SINR}(\boldsymbol{w})=\frac{\sigma_0^2\left|\boldsymbol{w}^{\mathrm{H}}\boldsymbol{a}_0\right|^2}{\boldsymbol{w}^{\mathrm{H}}\boldsymbol{R}_{j+n}\boldsymbol{w}}. \tag{18}$$

The signal power σ_0^2 can be estimated according to the following formulation:

$$\hat{\sigma}_0^2 = \boldsymbol{w}^{\mathrm{H}}\boldsymbol{R}\boldsymbol{w} = \frac{1}{\boldsymbol{a}_0^{\mathrm{H}}\boldsymbol{R}^{-1}\boldsymbol{a}_0}. \tag{19}$$

From equation (18) and equation (19), SINRs of CMT-mp-QP MVDR beamformer and mp-QP MVDR beamformer can be achieved, respectively.

Definition 4 For an adaptive antenna array system, the array gain is defined as the output Signal-to-Interference-and-Noise Ratio (SINR) divided by the input SINR and is given by:

$$G = \frac{\mathrm{SINR}_{\mathrm{out}}}{\mathrm{SINR}_{\mathrm{in}}} = \frac{\sigma_0^2\left|\boldsymbol{w}^{\mathrm{H}}a(\theta_0)\right|^2 \Big/ (\boldsymbol{w}^{\mathrm{H}}\boldsymbol{R}_{j+n}\boldsymbol{w})}{\sigma_0^2 \Big/ \sum_{j=1}^{J}\sigma_j^2 + \sigma_n^2}. \tag{20}$$

To calculate the output due to the desired signal, a distortionless constraint is imposed on $\boldsymbol{w}$ that $\boldsymbol{w}^{\mathrm{H}}a(\theta_0) = 1$. Consider the special case of spatial white noise and identical noise spectra at each sensor, the noise cross-spectral density matrix $\boldsymbol{\rho}_n$ reduces to an identity matrix. Thus the array gain for white noise is given by:

$$\begin{aligned} G &= \frac{\sum_{j=1}^{J}\sigma_j^2 + \sigma_n^2}{\boldsymbol{w}^{\mathrm{H}}\boldsymbol{R}_{j+n}\boldsymbol{w}} \\ &= \frac{\sum_{j=1}^{J}\sigma_j^2 + \sigma_n^2}{\sum_{j=1}^{J}\sigma_j^2\left|\boldsymbol{w}^{\mathrm{H}}a(\theta_j)\right|^2 + \sigma_n^2\boldsymbol{w}^{\mathrm{H}}\boldsymbol{w}} \\ &= \frac{\sum_{j=1}^{J}\sigma_j^2 / \sigma_n^2 + 1}{\sum_{j=1}^{J}\sigma_j^2 / \sigma_n^2\left|\boldsymbol{w}^{\mathrm{H}}a(\theta_j)\right|^2 + \left\|\boldsymbol{w}\right\|^2}, \end{aligned} \tag{21}$$

where $\|\cdot\|$ stands for the Euclidean norm.

From equation (21), the array gain of CMT-mp-QP MVDR beamformer and mp-QP MVDR beamformer can be calculated, respectively, according to the weight vectors given by equation (16) and equation (2).

V. SIMULATION RESULTS

In this section, we conduct some simulations to validate the proposed approach. Assume that the Uniform Linear Array (ULA) consists of seventeen sensors (M=17) equispaced by half-wavelength. Assume that the desired signal and two interference signals are plane waves impinging on the ULA from the directions 0° and $30^{\circ}, -30^{\circ}$, respectively. In these simulations, the Signal-to-Noise Ratio (SNR) is set to 0 dB, 35 dB and 35 dB for the desired signal and the two interference signals, respectively. The notch width $W = 9^{\circ}$ and $q = 5$. The sidelobe beampattern areas $[-90^{\circ}, -10^{\circ}] \cup [10^{\circ}, 90^{\circ}]$ are chosen and a uniform grid is used to obtain the angles. Sensor noises are modeled as spatially and temporally white Gaussian processes. It is assumed that $\xi^2 = 10^{-5}$ and $\varepsilon^2 = 10^{-2}$, i.e., we require the beampatterns null level below -50 dB and sidelobe level to be below -20 dB.

In the first simulation, 1024 snapshots are used to compute the direction patterns of mp-QP MVDR and CMT-mp-QP MVDR, which are plotted in Fig. 1. As shown in this figure, all the beampatterns place deep nulls at the DOAs of the interference signals and maintain a distortionless response for the signal-of-interest. However, mp-QP MVDR is not able to broaden the interference nulls and it has very high sidelobe level. The proposed algorithm can overcome these above shortcomings, with tapered covariance matrix that is and it can not only broaden the null width but also achieve lower sidelobe level.

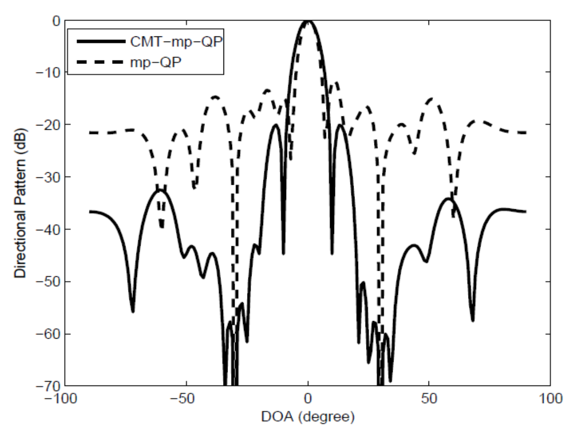

Fig. 1. Directional pattern curves of the proposed CMT-mp-QP method and pure mp-QP method.

In the second simulation, Fig. 2 gives the array gain curves (which are computed by equation (21)) of the aforementioned two beamformers, based on 200 independent trials under the hypothesis that SNRs range from -20 dB to 20 dB and the number of snapshots is equal to 1024. When $\mathrm{SNR} \le 0\mathrm{dB}$, mp-QP MVDR has a little better array gain than the proposed method. With the increase of SNR, it can be seen that CMT-mp-QP MVDR shows better array gain.

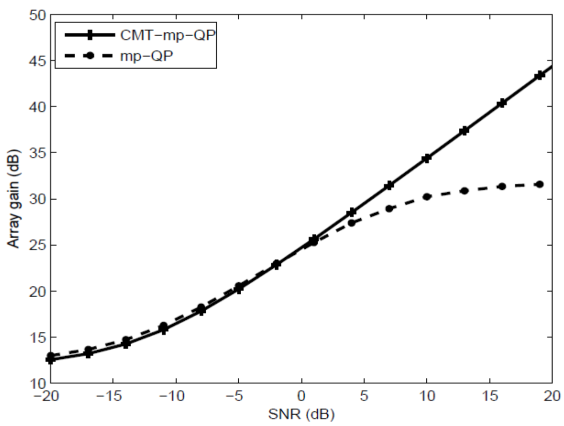

Fig. 2. Array gain versus SNR for various algorithms.

The third simulation considers that the number of snapshots is varied. Figure 3 shows the average output SINR curves (which are computed by equation (18) and equation (19)) of the aforementioned methods, based on 200 independent trials with the SNR equal to 10 dB. From the figure, it can be seen that the proposed method has better convergence even few samples are available. As the number of snapshots increases, the performances of both methods tend to stabilize, while CMT-mp-QP MVDR has higher output SINR than mp-QP MVDR.

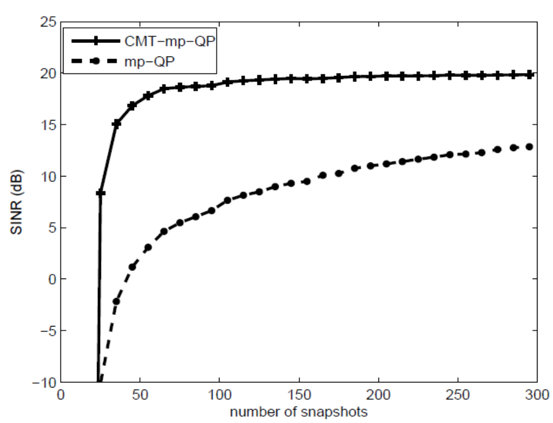

Fig. 3. Array gain versus number of snapshots.

VI. CONCLUSIONS

This paper presents an effective robust adaptive beamforming method with null broadening and sidelobe control. By modifying the measured covariance matrix, null broadening can be regarded as adding the coherent signals to each signal sources. Multiple quadratic inequality constraints outside the mainlobe beampattern area are used to guarantee the beampattern sidelobe level are strictly below some prescribed threshold. Then, the robust adaptive beamforming problem is formulated as a multi-parametric quadratic programming problem, such that the optimal weight vector can be estimated by real-valued computation. The performance of the presented method is verified by simulation.

ACKNOWLEDGMENT

This work has been supported by the Program for New Century Excellent Talents in University (NCET-13-0105; the Support Program for Hundreds of Outstanding Innovative Talents in Higher Education Institutions of Hebei Province, China, under Grant No. BR2-259; the Fundamental Research Funds for the Central Universities under Grant No. N120423002; the Program for Liaoning Excellent Talents in University (LJQ2012022); the Directive Plan of Science Research from the Bureau of Education of Hebei Province, China, under Grant No. Z2011129 and by the Specialized Research Fund for the Doctoral Program of Higher Education of China (No.20130042110003). The authors also gratefully acknowledge the helpful comments and suggestions of the reviewers, which have significantly improved the presentation of this paper.

REFERENCES

[1] Y. Zhang, H. Zhao, J. P. Lie, et al, "Robust beamforming technique with sidelobe suppression using sparse constraint on beampattern," *Applied Computational Electromagnetics Society Journal*, vol. 25, no. 11, pp. 947-955, 2010.

[2] R. J. Mailloux, "Covariance matrix augmentation to produce adaptive array pattern troughs," *Electronic Letters*, vol. 31, no. 10, pp. 771-772, 1995.

[3] M. Zatman, "Production of adaptive array troughs by dispersion synthesis," *Electronic Letters*, vol. 31, pp. 2141-2142, 1995.

[4] J. R. Guerci, "Theory and application of covariance matrix tapers for robust adaptive beamforming," *IEEE Trans. Signal Processing*, vol. 47, no. 4, pp. 977-985, 1999.

[5] F. L. Liu, J. K. Wang, C. Y. Sun and R. Y. Du, "Robust MVDR beamformer for nulling level

control via multi-parametric quadratic programming," *Progress In Electromagnetics Research* C, vol. 20, pp. 239-254, 2011.

[6] M. Wang and M. Fang, "A novel null broadening technique based on reduced-rank conjugate gradient algorithm," *Electronics Information Warfare Technology*, vol. 26, no. 4, pp. 14-17, 2011.

[7] F. L. Liu, R. Y. Du, J. K. Wang and B. Wang, "A robust adaptive control method for widening interference nulls," *IET International Radar Conference*, Guilin, China, pp. 297-300, 2009.

[8] F. L. Liu, C. Y. Sun and J. K. Wang, "Nulls control method based on semidefinite programming," *Journal of Northeastern University (Natural Science)*, vol. 32, no. 10, pp. 1386-1389, 2011.

[9] Q. T. Le, N. D. Nguyen and T. T. Dam, "Amplitude and phase adaptive nulling with a genetic algorithm for array antennas," *International Conference on Artificial Intelligence, Management Science and Electronic Commerce*, pp. 1887-90, 2011.

[10] D. Mandal, N. T. Yallaparagada, S. P. Ghoshal and A. K. Bhattacharjee, "Wide null control of linear antenna arrays using particle swarm optimization," *2010 Annual IEEE India Conference*, pp. 1-4, 2010.

[11] X. N. Zeng, Y. S. Zhang and H. B. Jin, "Application of wide nulling beamforming technology in anti-ARM battle," *Radar Science and Technology*, vol. 7, no. 1, pp. 71-74, 2009.

[12] M. R. R. Khan and V. Tuzlukov, "Null steering beamforming for wireless communication system using genetic algorithm," *IEEE International Conference on Microwave Technology and Computational Electromagnetics*, pp. 289-292, 2011.

[13] J. Liu, A. B. Gershman, Z. Q. Luo and K. M. Wong, "Adaptive beamforming with sidelobe control: a second-order cone programming approach," *IEEE Signal Processing Letters*, vol. 10, no. 11, pp. 331-334, 2003.

[14] Z. D. Zaharis, C. Skeberis and T. D Xenos, "Improved antenna array adaptive beamforming with low side lobe level using a novel adaptive invasive weed optimization method," *Progress In Electromagnetics Research*, vol. 124, pp. 137-150, 2012.

[15] D. P. Yang, H. Chen and K. P. Wang, "A simple algorithm of beamforming to achieve low sidelobe, audio engineering," *Audio Engineering*, vol. 33, no. 1, pp. 44-47, 2009.

[16] K. G. Song, Q. Gan and B. Tang, "A low sidelobe beamforming algorithm," *Signal Processing*, vol. 25, no. 5, pp. 777-80, 2009.

[17] P. Tondel, T. A. Johansen and A. Bemporad, "An algorithm for multi-parametric quadratic programming and explicit MPC solutions," *Automatica*, vol. 39, no. 3, pp. 489-497, 2003.

[18] A. Bemporad, M. Morari, V. Dua and E. E. Pistikopulos, "The explicit linear quadratic regular for constrained systems," *Automatica*, vol. 38, no. 1, pp. 3-20, 2002.

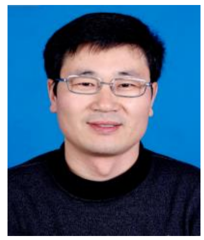

Fulai Liu was born in Hebei, China, in 1975. He received his B.S. degree from Hebei Normal University, Shijiazhuang, China, in 1999 and his M.S. and Ph.D. degrees from Northeastern University, Shenyang, China, in 2002 and in 2005, respectively. He is a member of IEEE and a member of IEEE Signal Processing Society. He has been a professor since 2010. He is currently working as a teacher at Northeastern University, Qinhuangdao, China. His research interests include adaptive signal processing, cognitive radio network and near space information processing.

Guozhu Sun was born in Hebei, China, in 1969. He received his B.S. degree from Hebei Medical College, Shijiazhuang, China, in 1991 and his M.S. and Ph.D. degrees from Hebei Medical University, Shijiazhuang, China, in 1998 and in 2007, respectively. He has been a professor since 2010. He is currently working as a Neurosurgeon at the 2nd Hospital of Hebei Medical University, Shijiazhuang, China. He is a Member of the WFON, a member of the Chinese Neurosurgical Society and a Member of the CCNS. His research interests include medical image processing in CNS, stereotactic and functional neurosurgery and brain protection.

Jinkuan Wang was born in 1957. He received his M.Eng. degree from Northeastern University, Shenyang, China, in 1985 and his Ph.D. degree from the University of Electro-Communications, Japan, in 1993. As a special member, he joined the Institute of Space and Astronautical Science, Japan, in 1990. He worked as an engineer in the Research Department of COSEL company, Japan, in 1994. He is currently a Professor in the Institute of Information and Engineering at Northeastern University, China, since 1998. His main interests are in the area of Intelligent Control and Adaptive Array.

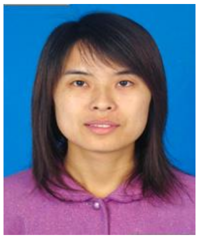

Ruiyan Du was born in 1978. She received her B.S. degree from Hebei Normal University, Shijiazhuang, China, in 1999, her M.S. degree from Yanshan University, Qinhuangdao, China, in 2006 and her Ph.D. degree from Northeastern University, Shenyang, China, in 2012. She is currently working as an Associate Professor at Northeastern University, Qinhuangdao, China. Her research interests focus on array signal processing, wireless communications, cognitive radio, etc.

Optimal Design of Electromagnetic Absorbers

R. Araneo and S. Celozzi

Department of Astronautic, Electrical and Energetic Engineering
University of Rome "La Sapienza", via Eudossiana 18, 00184 Rome, Italy
rodolfo.araneo@uniroma1.it, salvatore.celozzi@uniroma1.it

Abstract ─ A procedure for the optimal design of compact and light-weight electromagnetic absorbers is presented. The absorbers are designed to damp resonances inside metallic enclosures on the basis of Jaumann's theory; several layers of lossy (artificial) dielectrics are separated by two high/low impedance frequency selective surfaces and one resistive sheet. The constitutive parameters of the absorbing layers are optimized by means of the Particle Swarm Optimization method in order to maximize bandwidth and absorption rate of the structure in the GHz frequency range, where typically the first resonances of small enclosures occur.

Index Terms - Absorbing materials, electromagnetic shielding, finite integration technique, particle swarm optimization and shielding effectiveness.

I. INTRODUCTION

The design of layers capable of absorbing Electromagnetic (EM) waves has been afforded either in numerical studies, e.g., [1], [2] and in practical applications [3]. One of the most challenging benchmarks to test a design procedure for EM absorbers is represented by the resonances occurring in typical shielding enclosures. Metallic cabinets behave as overmoded cavities at working frequencies, and the twofold goal of avoiding unwanted emissions and improving immunity of shielded devices is accomplished by damping the EM field in the shielded region. The Shielding Effectiveness (SE) of an enclosure is usually quantified according to the IEEE Std. 299 in terms of the ratio of the incident over the shielded electric (magnetic) field at a selected point inside the enclosure; although, integral definitions have been proposed and adopted [4], [5]. It is well known that resonances can dramatically deteriorate the screening performance of the enclosure, because the excited internal modes can enhance the field in the victim proximity and apertures may increase these effects. Resonances can be suppressed by lining the internal enclosure surfaces with properly designed absorbers.

Research into EM wave absorbers started in the 1930's, shortly after the advent of radar with the aim of developing materials capable to reduce the radar cross-section (radar absorbing materials) and camouflaging military devices (stealth technologies) [6]. Through the years, the interest in absorbing materials has spread to the commercial sector to reduce interferences resulting from a growing number of EM apparatus, reaching into the radio frequency band [7]. Nowadays, there is a rising demand for lighter weight and more highly absorbing materials in a number of applications [8]. Absorbers can be roughly classified into impedance matching and resonant absorbers, though many absorbers have features of both these classifications; traditional designs include pyramidal, tapered loading, matching layers and ferrite-based absorbers [9], as well as Salisbury [10], [11] and Dallenbach [12] screens, Jaumann absorbers [13], [14] and circuit analog absorbers based on the use of lossy frequency selective surfaces [14], [15].

In this work, a procedure for the design of absorbing materials for damping resonances inside shielded enclosures is presented. The aims of the study are to design and optimize the performances of an absorbing structure in the GHz range, where the first resonances of commercial enclosures occur and to maximize the bandwidth and minimize the reflection coefficient for oblique

Submitted On: September 25, 2013
Accepted On: April 17, 2014

angles of incidence. The layered structure is based on Jaumann's theory and on circuit analogy. The main idea of Jaumann's theory is based on the achievement of a cancelling interference between incident and reflected wave by means of adequate dimensions and properties of the multi-layer structure. Absorption is enhanced alternating dielectrics and inductive, capacitive or resistive sheets; four layers of lossy dielectrics, one loaded with lossy wires are considered and alternated with three lossy sheets, two of which are lossy capacitive/inductive frequency selective surfaces [16], [17].

II. SYSTEM CONFIGURATION

The electromagnetic problem under analysis is sketched in Fig. 1 (a): a metallic enclosure, whose walls are assumed to be perfectly conducting and infinitesimally thin, presents an aperture on one side. When the enclosure is illuminated by an impinging external field $\mathbf{E}^i$ or driven by internal sources, e.g., electric $\mathbf{J}_s$ or magnetic $\mathbf{M}_s$ dipoles [5], internal resonances can be excited deteriorating the shielding performances of the enclosure. As an example, in Fig. 1 (b), it is reported the electric field shielding effectiveness SE_E of a commercial enclosure, having dimensions $a \times b \times c$ = 30×40×12 cm, with a rectangular aperture with dimensions $w \times h$ = 15×3 cm on its front side. Results are obtained by means of a Method of Moments (MoM) formulation [5] from 100 MHz to 3 GHz. The enclosure is illuminated with an y-directed uniform plane wave with the electric field linearly polarized along the shortest side of the aperture (i.e., the z-axis) and the observation point is in the center of the enclosure (E_z = 1 V/m). In this frequency range, the enclosure exhibits 81 resonant frequencies as shown in Fig. 1 (b), with vertical grey lines (only the first 27 up to 2 GHz are reported in Table 1). It is evident that resonances and anti-resonances appear in the frequency spectrum of the SE_E, depending on the position of the observation point inside the cavity and on the resonant modes that are excited by the source field. Furthermore, Fig. 1 (c) shows the pattern of the first mode, while Fig. 1 (d) shows the maps of the magnitude of the electric field on the *xy*-plane and *yz*-plane passing for the center of the enclosure. As it is evident, the magnitude of the electric field at the first resonance is maximum at the center of the shielded box where the SE_E is evaluated, so that the shielding effectiveness presents there's a minimum.

In order to improve the SE_E, especially in the neighborhood of the resonant frequencies, the interior cabinet surfaces are lined with an artificial absorbing material to damp the excited resonant fields, as shown in Fig. 1 (a).

The design procedure proceeds in two steps: first, the layers characteristics are determined with reference to a set of plane wave sources having different incidence angles in the assigned frequency bandwidth. Then, the multilayer effectiveness is tested inside the enclosure in order to ascertain whether the initial goals have been met with the absorber in place. An iteration with more stringent constraints may be necessary or not, depending on the configuration and on the experience in fixing the initial target values.

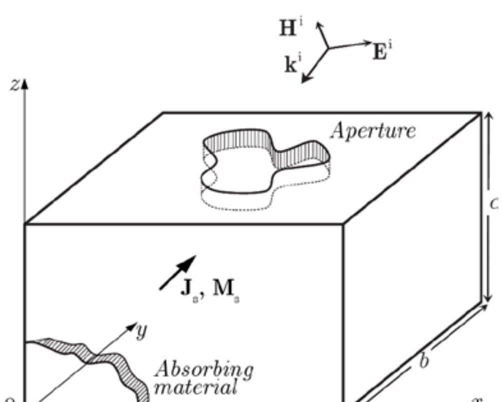

(a)

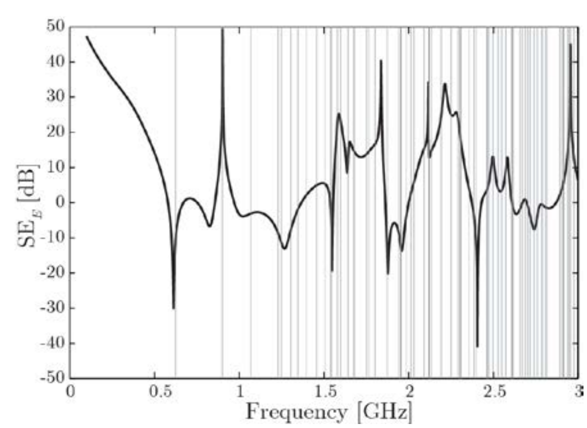

(b)

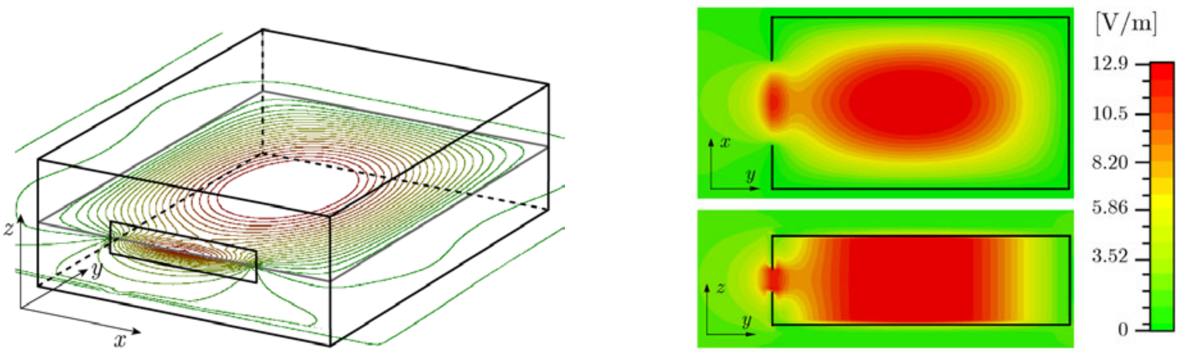

(c) (d)

Fig. 1. (a) Shielded enclosure, with an aperture on one side, loaded with absorbing material in order to damp its resonances; (b) SE E versus frequency at the center of the shielded enclosure illuminated by an y-directed impinging plane wave: a=30 cm, b=12 cm, c=40 cm, rectangular aperture with dimensions w=15 cm, h=3 cm, centered in the xz-side; (c) electric field map at the first resonant frequency and (d) electric field patterns at the first resonant frequency in the center of xy-plane and yz-plane.

Table 1: Natural resonant frequencies up to 2 GHz of the 30×12 cm enclosure, along with the mode indices *l*, *m* and *n*

l	*m*	*n*	*f* [GHz]	*l*	*m*	*n*	*f* [GHz]
1	1	0	0.624	2	2	1	1.766
2	2	0	0.900	2	4	0	1.801
2	1	0	1.067	3	3	0	1.873
1	3	0	1.230	1	5	0	1.939
2	2	0	1.249	2	0	1	1.599
0	1	1	1.304	2	1	1	1.643
1	0	1	1.345	3	2	0	1.675
1	1	1	1.396	0	3	1	1.680
0	2	1	1.456	1	3	1	1.753
2	3	0	1.504	3	0	1	1.951
1	2	1	1.540	0	4	1	1.951
3	1	0	1.545	2	3	1	1.955
1	4	0	1.580	3	1	1	1.986

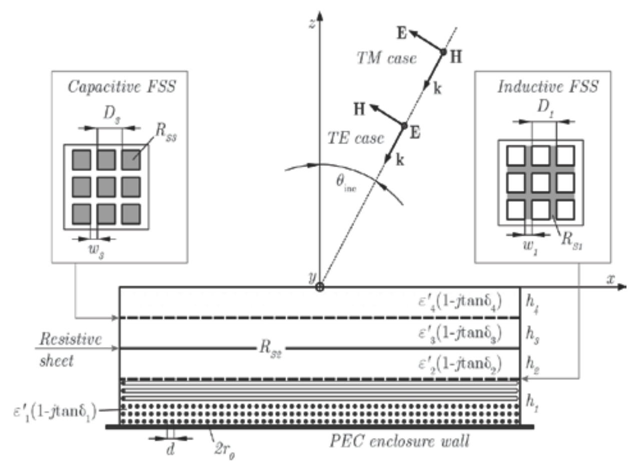

Fig. 2. Schematic of the multi-layer absorber; all the dielectrics are lossy $\varepsilon_r = \varepsilon_r' - j\varepsilon_r''$ and the dielectric adjacent to the PEC surface is a wire-medium.

III. EQUIVALENT CIRCUIT REPRESENTATION

The proposed absorbing material consists of four dielectric layers alternated with three lossy sheets, as depicted in Fig. 2. The outer sheet is a capacitive array of patches, the middle sheet is a homogeneous resistive sheet and the inner sheet is an inductive strip-grid. Furthermore, the dielectric layer adjacent to the PEC surface is a wire-medium, realized by means of orthogonal wires in order to achieve a better polarization insensitivity.

By proper selection of the geometrical and physical parameters of conductive sheets and dielectric layers, the result consisting in minimum EM field reflection over a prescribed frequency range and for oblique incidence angles is achieved. Particular effort has been devoted to make the absorber's characteristics as independent as possible of the incident angle [18]. To perform the design of the artificial material, an equivalent circuit representation is established by means of equivalent surface impedances and quasi-dynamic formulas for effective parameters obtained through homogenization procedures [19]. The equivalent circuit representation is more suitable for the optimal tuning of the constitutive parameters.

The propagation of uniform plane-waves in homogeneous stratified media can be modeled by means of the analogy with voltage and current waves on uniform equivalent Transmission Lines (TLs) [20], [21]; any arbitrary incident plane wave is decomposed into its fundamental TE_z and TM_z polarized waves, as in Fig. 2. The propagation constants $k_{z,i}$ and the intrinsic characteristic impedance $Z_{c,i}$ of the i-th medium at angular frequency ω, are functions of both polarization and angle of incidence θ_{inc} as:

$$k_{z,i} = k_0 \sqrt{\varepsilon_{r,i} - \sin^2 \theta_{inc}}, \quad (1a)$$

$$Z_{c,i}^{TE} = \frac{\omega \mu_0}{k_{z,i}}, \quad (1b)$$

$$Z_{c,i}^{TM} = \frac{k_{z,i}}{\omega \varepsilon_0 \varepsilon_{r,i}}, \quad (1c)$$

where $j = \sqrt{-1}$, k_0 is the wavenumber in free space, ε_0 and μ_0 are, respectively, the absolute permittivity and permeability of vacuum and $\varepsilon_{r,i}$ is the relative electric permittivity of i-th medium. The square root branch in (1a) is specified by the condition $-\pi < \arg(k_{z,i}) \le 0$. The free space surrounding the structure is modeled by a port with interior impedance Z_{fs}, according to (1b)-(1c), where $\varepsilon_{r,i}$ is set equal to 1. Thus, the equivalent circuit reported in Fig. 3 is obtained.

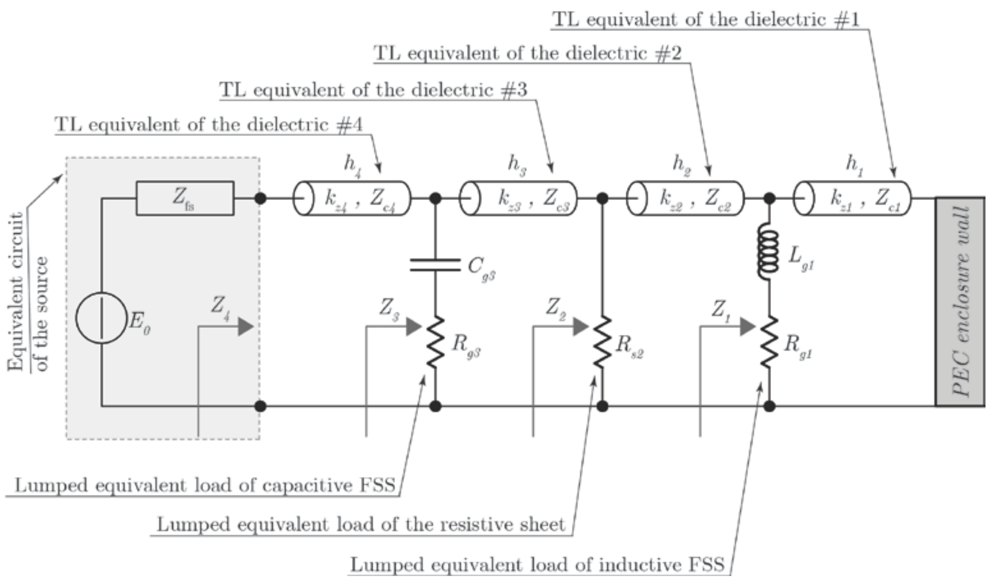

Fig. 3. Equivalent circuit model of the overall system; an equivalent EM field source (frequency-, polarization- and angle-of-incidence-dependent) incident on a multi-layer absorber.

To account for the three sheets located at the interfaces between dielectrics, equivalent lumped impedances are derived and inserted transversally in the equivalent circuit. An array of patches (outer interface #3), at frequencies well below the array resonances, exhibits an equivalent grid capacitance C_g [22]:

$$C_g^{TM} = \frac{2\alpha}{\eta_{\text{eff}} \omega}, \quad (2a)$$

$$C_g^{TE} = \frac{2\alpha}{\eta_{\text{eff}} \omega} \left(1 - \frac{\sin^2 \theta_{inc}}{2 \mu_0 \varepsilon_{\text{eff}}} \right), \quad (2b)$$

where α is the grid parameter:

$$\alpha = \frac{k_{\text{eff}} D}{\pi} \ln \left(\frac{1}{\sin \left(\frac{\pi w}{2D} \right)} \right), \quad (3)$$

and the effective (complex) permittivity is function of the two adjacent dielectric permittivity's:

$$\varepsilon_{\text{eff}} = \varepsilon_0 \frac{\varepsilon_{r,i} + \varepsilon_{r,i+1}}{2}. \tag{4}$$

In (3), w is the width of the gap between adjacent patches, D is the period of the structure (as shown in Fig. 2), η_{eff} is the effective intrinsic wave impedance, $\eta_{\text{eff}} = \sqrt{\mu_0/\varepsilon_0\varepsilon_{\text{eff}}}$ and k_{eff} is the effective wavenumber, $k_{\text{eff}} = k_0\sqrt{\varepsilon_{\text{eff}}}$. If the sheet is lossy, an equivalent resistance R_g should be inserted in series with the capacitance. According to [23], the resistance can be computed as:

$$R_g = \frac{R_s}{D-w}\frac{C_g}{\varepsilon_{\text{eff}}}, \tag{5}$$

where R_s is the surface resistance of the sheet (measured in Ω/sq).

For a grid of strips (inner interface #1), the grid impedance is inductive. Through the Babinet's principle, the inductance can be derived straightforwardly from (2) as [22]:

$$L_g^{TM} = \frac{\eta_{\text{eff}}\alpha}{2\omega}\left(1 - \frac{\sin^2\theta_{inc}}{2\mu_0\varepsilon_{\text{eff}}}\right), \tag{6a}$$

$$L_g^{TE} = \frac{\eta_{\text{eff}}\alpha}{2\omega}, \tag{6b}$$

where (3)-(4) still hold, considering w as the strip width (see Fig. 2). If the sheet is lossy, an equivalent resistance R_g should be inserted in series with the inductance. According to [23], the resistance is:

$$R_g^{TE/TM} = \frac{R_s}{w}\frac{L_g^{TE/TM}}{\mu_{\text{eff}}}. \tag{7}$$

The homogeneous resistive sheet located at the interface #2, is represented by its surface resistance R_{s2}, as shown in Fig. 3.

The layers between sheets are assumed to be lossy dielectric with relative dielectric constant $\varepsilon_{r,i} = \varepsilon'_{r,i} - j\varepsilon''_{r,i} = \varepsilon'_{r,i}\left(1 - j\tan\delta_i\right)$, where $\tan\delta_i$ is the loss tangent of the i-th dielectric medium. The inner dielectric adherent to the PEC surface of the enclosure is an artificial lossy wire-medium, as shown in Fig. 2. In the long-wavelength limit, such a structure behaves like an homogeneous material whose effective relative permittivity is a frequency-dependent scalar quantity. In the case of E-polarized incident plane wave and lossy wires with finite conductivity σ, the dielectric constant reads [24]:

$$\varepsilon_{r,i} = \varepsilon'_{r,i} - j\varepsilon''_{r,i} = \varepsilon_{r,h} + \frac{c_0\eta_0}{j\omega d^2\left(j\omega L + \zeta_s\right)}, \tag{8}$$

where c_0 is the free space speed of light, η_0 is the wave impedance in free space, d is the period of the wire grid and ε_{rh} is the relative permittivity of the host medium. In (8), the per unit length external inductance of wires L is given by:

$$L = \frac{\mu_0\mu_{rh}}{2\pi}\ln\left[\frac{d^2}{4r_0\left(d - r_0\right)}\right], \tag{9}$$

being r_0 the wire radius. The per unit length impedance ζ_s, accounting for wire losses is:

$$\zeta_s = \frac{1+j}{2\pi r_0}\sqrt{\frac{\pi\eta_0 f}{c_0\sigma}}\frac{I_0(\xi)}{I_1(\xi)}. \tag{10}$$

In (10), $I_0(\cdot)$ and $I_1(\cdot)$ are, respectively, the modified Bessel functions of the first kind of order 0 and 1, and:

$$\xi = (1+j)\sqrt{\omega\mu_0\sigma}\,r_0. \tag{11}$$

In order to obtain a material effective under both TM_z and TE_z polarizations, two set of wires mutually perpendicular have been introduced in order to achieve polarization insensitivity.

The actual reflection coefficient Γ of the multilayered material at air/absorber interface #4, must be computed by using the well-known transmission line theory. Starting from the inner layer #1 and moving toward the free space, the input impedance Z_i at the beginning of the i-th line (assuming the line terminated at $l = h_i$ on the impedance Z_{i-1}, with $Z_0 = 0$ since the first line is terminated on the PEC surface of the enclosure) is evaluated:

$$Z_i = Z_{c,i}\frac{Z_{i-1} + Z_{c,i}\tanh(jk_{z,i}h_i)}{Z_{c,i} + Z_{i-1}\tanh(jk_{z,i}h_i)}. \tag{12}$$

Then the impedance value Z_i is updated by performing the parallel of the computed Z_i with the lumped sheet admittance Y_i^{sheet} (we assume $Y_4^{sheet} = 0$ since there is no sheet at the air/absorber interface), according to:

$$Z_i = \left(\frac{1}{Z_i} + Y_i^{sheet}\right)^{-1}. \tag{13}$$

Finally, once the Z_4 is available, the reflection coefficient (to be minimized) of the absorbing material can be computed as:

$$\Gamma = \frac{Z_4 - Z_{\text{fs}}}{Z_4 + Z_{\text{fs}}}. \tag{14}$$

It should be noted that Γ has to be minimized in a prescribed frequency range and for various incidence angles and polarizations.

IV. OPTIMIZATION

To optimize all the geometrical and constitutive parameters of the absorbing material in order to reduce its reflection coefficient Γ in the prescribed frequency range, the Particle Swarm Optimization (PSO) has been used. Several metaheuristic evolutionary algorithms are available today, such as the Genetic Algorithm (GA), the Ant Colony Optimization (ACO), the Bees Algorithms and the PSO, and they have been applied successfully in the design of absorbing materials [25]-[28]. Since its proposal by Kennedy and Eberhart in 1995 [29], the PSO has rapidly become very popular as an efficient optimization method for solving single objective and multi-objective optimization problems. In addition, a large number of works dealing with the application of the PSO technique to engineering problems, is available in literature [30]-[34] and the authors have developed a good expertise with this method in several past works [7], [34]-[36]. For these reasons, the PSO have been selected for the optimization process.

In the present work, a simple variation of the original PSO, referred to as Meta Particle Swarm Optimization (MPSO) [27] is adopted. It simply consists in subdividing the entire swarm in more subgroups of particles moving through the space domain $\mathcal{D}$. Each j-th group is composed of M_j particles flying with a velocity vector $\mathbf{v}_t^{m,j} = \left[v_{1,t}^{m,j}, \quad v_{2,t}^{m,j}, \quad \ldots, \quad v_{N,t}^{m,j} \right]^T$, at time t (with m =1, 2, …, M_j), around a multidimensional search space $\mathcal{D}$. During its flight, each particle updates its position $\mathbf{x}_t^{m,j} = \left[x_{1,t}^{m,j}, \quad x_{2,t}^{m,j}, \quad \ldots, \quad x_{N,t}^{m,j} \right]^T$ according to its own experience, to that of the group, which the particle belongs to and to the experience of the entire warm. The MPSO method combines three search levels:

1. A local single-particle search: the m-th particle knows its personal best position $\mathbf{b}_L^{m,j}$ (local optimum solution); i.e., the coordinates associated with the best solution that the particle has achieved so far.
2. A group local search: the m-th particle exchanges information with other particles of the same group and knows the $\mathbf{b}_S^j$ value (global optimum solution inside the j-th group); i.e., the coordinates associated with the best position even tracked by the group giving the best fitness value in the group population.
3. A swarm global search: the m-th particle exchanges information with all other particles and knows the best global value $\mathbf{b}_G$ (global optimum solution); i.e., the coordinates associated with the best position even tracked by the swarm giving the best fitness value in the entire population.

At each algorithm step, $\mathbf{b}_L^{m,j}$, $\mathbf{b}_S^j$ and $\mathbf{b}_G$ are computed, updated and used by the particles to adjust their velocities and positions in order to improve their current fitness through the following two updating equations:

$$\begin{aligned} \mathbf{v}_{t+1}^{m,j} &= w\mathbf{v}_t^{m,j} + c_1\varphi_1 \left(\mathbf{b}_L^{m,j} - \mathbf{x}_t^{m,j} \right) \\ &+ c_2\varphi_2 \left(\mathbf{b}_S^{j} - \mathbf{x}_t^{m,j} \right) + c_3\varphi_3 \left(\mathbf{b}_G - \mathbf{x}_t^{m,j} \right), \end{aligned} \tag{15a}$$

$$\mathbf{x}_{t+1}^{m,j} = \mathbf{x}_t^{m,j} + \mathbf{v}_{t+1}^{m,j}. \tag{15b}$$

The entire optimization relies on the correct manipulation of the particles' velocities; w is the inertia factor, which keeps the particle in its current trajectory. The last three terms inject deviation according to the distances from $\mathbf{b}_L^{m,j}$, $\mathbf{b}_S^j$ and $\mathbf{b}_G$ best locations through the cognitive factor c_1, the group social factor of the j-th group c_2 and the global social factor c_3. The numbers φ_1, φ_2 and φ_3 are random variables distributed in the range [0,1], which inject the unpredictability of the particles' movement. The convergence of the algorithm depends on the proper tuning of the acceleration coefficients and on the boundary conditions used to prevent the explosion of the particles [37].

It should be noted that all the groups interact among them in the optimization process. In the early time of the iteration process, the global best particle $\mathbf{b}_G$ appears in every subgroup alternately, which shows the well global exploration performance that tends to concentrate in the territory around the group best particle $\mathbf{b}_S^j$ in the medium time of the process. Then, when the algorithm enters the latter time of the process, $\mathbf{b}_G$ is almost fixed in some subgroup and the algorithm begins with a local research around the best position tracked by the swarm. Several papers [38], [39] have introduced additional factors in the velocity equation; named repulsive factors in order to encourage individual particles, located in the territory of other groups to escape from the other groups' territory in efficient manners and consequently search for multiple optima in the solution space.

In the problem at hand, each particle $x_{j,t}^{m,j}$ consists of a possible set of values for the constitutive/geometrical parameters of the absorbing material. The inertia and acceleration coefficients have been chosen according to [37] and the reflecting boundary conditions have been used to relocate the particles that fly outside the allowed solution space. The cost function $\mathcal{F}$ that needs to be minimized is defined as:

$$\mathcal{F} = \frac{1}{2N_{freq}N_{inc}} \cdot \sum_{l=TE,TM} \sum_{m=1}^{N_{freq}} \sum_{n=1}^{N_{inc}} \left|\Gamma_l\left(\omega_m, \theta_{inc,n}\right) - \Gamma_0\right|^2, \tag{16}$$

where N_{freq} is the number of sampling frequencies ω_m distributed over the band of interest, N_{inc} is the number of angles of incidence $\theta_{inc,n}$, Γ_0 is the target value to be achieved and $\Gamma_l\left(\omega_m, \theta_{inc,n}\right)$ is the computed actual value of the reflection coefficient.

V. RESULTS

The methodology has been applied for the design of two absorbers in the frequency range from 100 MHz up to 3 GHz. The first one is constrained to possess best performance below 1 GHz because it is aimed at absorbing the first resonant modes. The second one is designed to absorb the higher modes of the enclosure occurring at frequencies above 1 GHz.

The following constraints have been enforced:

1. The periods D_1 and D_3 of both the selective surfaces (patch array and strip-grid) have been considered equal (through several simulations we have found that the optimum solution is near the condition D_1=D_3, so that this constrain has been directly enforced in the optimization process in order to obtain a simpler absorber).
2. The host dielectric of the wire-medium (medium #1) has been considered to be foam, $\varepsilon_{rh} = 1$.
3. The loss tangent of all the remaining dielectrics has been set equal to 1.25×10^{-4}.
4. The two frequency selective surfaces have been considered lossless.

The geometrical variables and physical parameters that have been optimized are reported in Table 2 with their "optimum" values.

Table 2: Optimized values of the constitutive parameters of the absorber obtained through the PSO

Parameter	Absorber #1	Absorber #2
ε_2	9.9	4.5
ε_3	2.6	1.2
ε_4	5.9	2.9
h_1	4.8 mm	1.6 mm
h_2	5.5 mm	1.6 mm
h_3	5.8 mm	1.7 mm
h_4	6 mm	2 mm
D_1=D_3	22.8 mm	18.4 mm
w_1	0.8 mm	0.2 mm
w_3	2.2 mm	1.8 mm
R_{s2}	81.5 Ω/sq	243.7 Ω/sq
d	1 mm	0.3 mm
r_0	10 μm	5 μm

The frequency spectrum of the reflection coefficients Γ for both TM_z and TE_z polarizations are reported in Figs. 4, for different angles of incidence θ_{inc} for either of the absorbers. In all the Figs., it also reported the frequency trend of the prescribed reflectivity Γ_0, that has been assumed equal to a band-pass Chebyshev filter of second type of order 4, for the design of the absorber #1 and 5, for the design of the absorber #2, with stop-band ripple equal to 10 dB and stop-band-edge frequencies equal to 100 MHz and 3 GHz in either cases. The absorbing performance are not substantially degraded, increasing the incidence angle θ_{inc}. It is possible to note that under TM_z polarization, the absorbing performance of the two absorbers are less stable with respect to the angle of incidence; nevertheless, they show higher absorbing coefficients for all the angles of incidence.

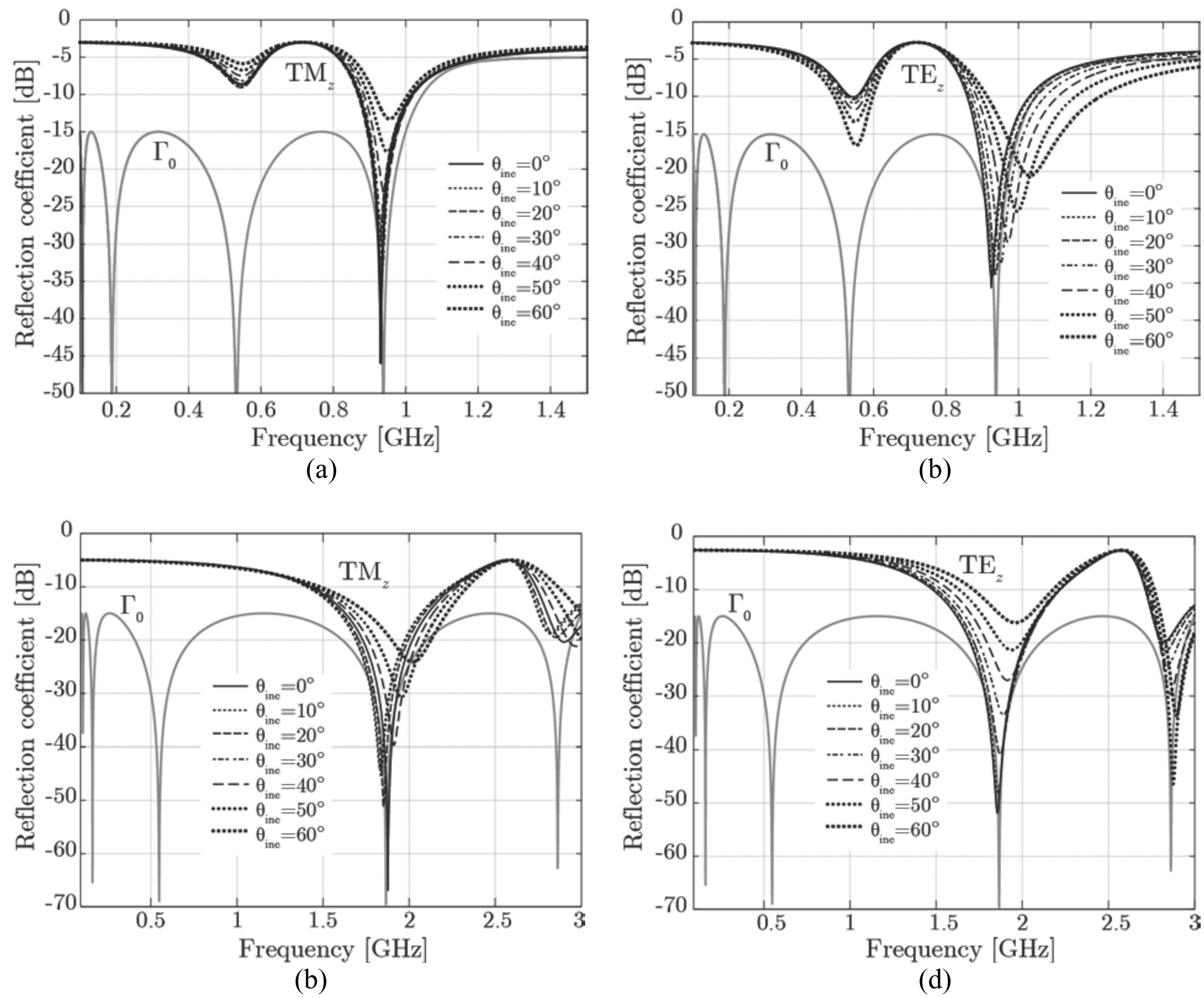

Fig. 4. Reflection coefficients Γ of the two absorbers versus frequency f for TM_z and TE_z polarizations for different angles of incidence θ_{inc}.

For the sake of completeness, the best value $\mathbf{b}_G$ and the mean value of the swarm (that has been subdivided in 4 tribes) during the search are reported in Figs. 5, for both the absorbers. It is evident that after a very steep descent in the first steps, the tribes move slowly but quite constantly toward the best solution.

Finally, the shielding effectiveness SE_E of the commercial enclosure studied in Figs. 1, having dimensions $a \times b \times c$ = 30×40×12 cm, with a rectangular aperture with dimensions $w \times h$ =15×3 cm on its front side, has been newly computed twice under a perpendicularly impinging plane wave ($\mathbf{E} = \mathrm{E}\hat{z}$ and $\mathbf{k} = \mathrm{k}\hat{y}$); a first time with absorber #1 placed on its interior walls, then with absorber #2. The results have been obtained by means of the Commercial Software CST Microwave Studio based on the Finite Integration Technique in the Time Domain. The results are reported in Figs. 6. It is possible to note that the absorbers are effective in damping the effect of the first resonant frequencies of the shielded enclosure and their performance are reasonable compared to their geometrical dimensions and the values of their constitutive parameters. The attenuation shown by both the absorbers when placed inside the test enclosure are substantially in accordance with the theoretical predictions under plane wave incidence, with variable angle of incidence θ_{inc}. Finally, Figs. 7 show the pattern of the electric filed at the first resonant frequency of the enclosure f = 0.624 GHz, without (Fig. 7 (a)) and with (Fig. 7 (b)) the absorber #1 on the interior sides of the walls of the enclosure.

The absorber is effective in reducing the magnitude of the resonant field mode, especially in the central zone of the enclosure.

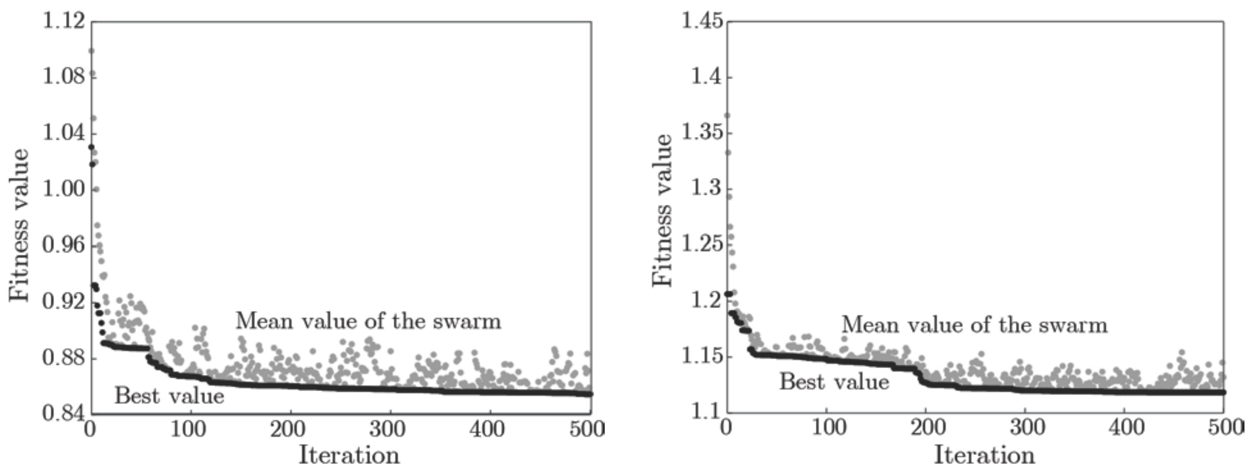

Fig. 5. Best value and mean value of the swarm during the optimization process.

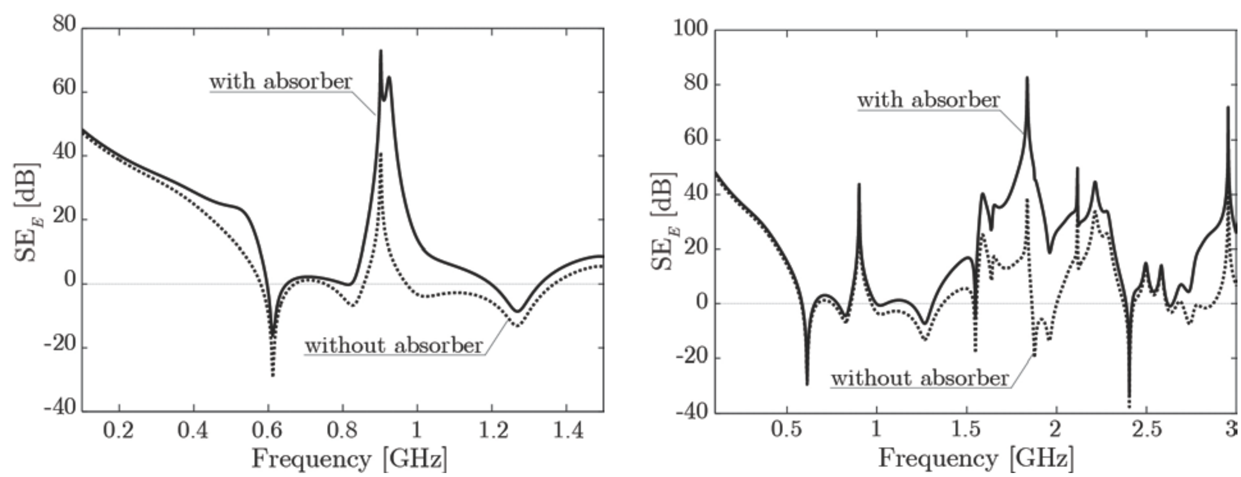

Fig. 6. Shielding effectiveness of the enclosure reported in Figs. 1, with and without the designed absorbers placed on its interior walls.

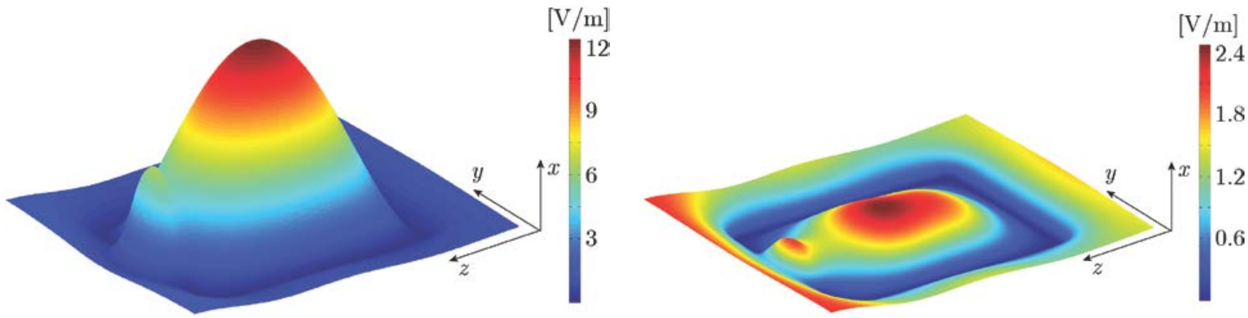

Fig. 7. Pattern of the electric field inside the enclosure at the first resonant frequency $f = 0.624$ GHz, with and without absorber #1.

VI. CONCLUSION

In this work, an optimal design procedure is presented, aimed at achieving compact and light-weight absorbing structures for damping resonances inside shielded enclosure. The proposed absorber is based on the concepts of Jaumann's layers and circuit analog absorbers; it employs four layers of lossy (artificial) dielectrics, separated by two high/low impedance frequency selective surfaces and one resistive sheet. The parameters of the absorber have been optimized by means of a PSO, in order to maximize its performance in the frequency range between 0.1 GHz and 3 GHz, for various incidence angles. The results show that an absorber with the expected performance can be obtained, demonstrating the effectiveness of the proposed design procedure and absorber configuration.

REFERENCES

[1] W. Abdelli, X. Mininger, L. Pichon and H. Trabelsi, "Impact of composite materials on the shielding effectiveness of enclosures," *ACES Journal*, vol. 27, no. 4, pp. 369-375, 2012.

[2] M. Agatonovic, Z. Marinkovic and V. Markovic, "Application of anns in evaluation of microwave pyramidal absorber performance," *ACES Journal*, vol. 27, no. 4, pp. 326-333, 2012.

[3] E. A. Hashish, S. M. Eid and S. F. Mahmoud, "Design of wideband planar absorbers using composite materials," *ACES Journal*, vol. 24, no. 4, pp. 413-418, 2009.

[4] S. Celozzi, "New figures of merit for the characterization of the performance of shielding enclosures," *IEEE Trans. Electromagn. Compat.*, vol. 46, no. 1, February 2004.

[5] R. Araneo and G. Lovat, "Analysis of the shielding effectiveness of metallic enclosures excited by internal sources through an efficient method of moment approach," *ACES Journal*, vol. 25, no. 7, pp. 600-611, July 2010.

[6] W. Emerson, "Electromagnetic wave absorbers and anechoic chambers through the years," *IEEE Trans. Antennas Propagat.*, vol. 4, pp. 484-490, July 1973.

[7] R. Araneo, G. Lovat and S. Celozzi, "Shielding effectiveness evaluation and optimization of resonance damping in metallic enclosures," *In Proc. IEEE Asia-Pacific Electromagn. Compat. Symp.*, pp. 528-531, April 12-16, 2010.

[8] E. Michielssen, S. R. J. M. Sajer and R. Mittra, "Design of lightweight, broad-band microwave absorbers using genetic algorithms," *IEEE Trans. Antennas Propagat.*, vol. 41, no. 6, pp. 1024-1031, June 1993.

[9] F. L. Teixeira, "On aspects of the physical realiza-bility of perfectly matched absorbers for electro-magnetic waves," *Radio Science*, vol. 38, no. 2, VIC 15, pp.1-15, 2003.

[10] W. W. Salisbury, "Absorbent body for electromagnetic waves," *US patent 2599944*, June 1952.

[11] R. L. Fante, M. T. McCormack, T. D. Syst and M. A. Wilmington, "Reflection properties of the salisbury screen," *IEEE Trans. Antennas Propagat.*, vol. 36, no. 10, pp. 1443-1454, October 1988.

[12] W. Dallenbach and W. Kleinsteuber, "Reflection and absorption of decimeter-waves by plane dielectric layers," *Hochfreq. u Elektroak.*, vol. 51, pp. 152-156, 1938.

[13] H. Severin, "Nonreflecting absorbers for microwave radiation," *In Electromag. Wave Theory Symp.*, vol. 7, pp. 385-392, 1956.

[14] B. A. Munk, "Frequency selective surfaces: theory and design," New York: *Wiley*, 2000.

[15] S. A. Tretyakov and S. I. Maslovski, "Thin absorbing structure for all incidence angles based on the use of a high-impedance surface," *Microw. Opt. Techn. Let.*, vol. 38, no. 3, pp. 175-178,

August 2003.
[16] R. Araneo, G. Lovat and S. Celozzi, “Shielding effectiveness of periodic screens against finite high-impedance near-field sources,” *IEEE Trans. Electromagn. Compat*., vol. 53, no. 3, pp. 706-716, August 2011.
[17] G. Lovat, R. Araneo and S. Celozzi, “Dipole excitation of periodic metallic structures,” *IEEE Trans. Antennas Propagat.*, vol. 59, no. 6, pp. 2178-2189, June 2011.
[18] J. A. Gordon, L. Holloway and A. Dienstfrey, “A physical explanation of angle-independent reflection and transmission properties of metafilms/metasurfaces,” *IEEE Antennas Wireless Propagat. Lett*., vol. 8, pp. 1127-1130, 2009.
[19] M. Silveirinha and C. Fernandes, “Homogenization of metamaterial surfaces and slabs: the crossed wire mesh canonical problem,” *IEEE Transactions on Antennas and Propagation*, vol. 53, no. 1, pp. 59-69, January 2005.
[20] K. A. Michalski and J. R. Mosig, “Multilayered media green’s functions in integral equation formulations,” *IEEE Trans. Antennas Propagat*., vol. 45, no. 3, pp. 508-519, March 1997.
[21] R. Araneo and S. Celozzi, “Analysis of the shielding performance of ferromagnetic screens,” *IEEE Trans. Magn*., vol. 39, no. 2, pp. 1046-1052, March 2003.
[22] O. Luukkonen, C. Simovski, G. Granet, G. Goussetis, D. Lioubtchenko, A. V. Raisanen and S. A. Tretyakov, “Simple and accurate analytical model of planar grids and high-impedance surfaces comprising metal strips or patches,” *IEEE Trans. Antennas Propagat.*, vol. 56, no. 6, pp. 1624-1632, June 2008.
[23] F. Bilotti, A. Toscano, L. Vegni, K. Aydin, K. B. Alici and E. Ozbay, “Equivalent-circuit models for the design of metamaterials based on artificial magnetic inclusions,” *IEEE Trans. Microwave Theory Tech.*, vol. 55, no. 12, pp. 2865-2873, 2007.
[24] G. Lovat, P. Burghignoli and S. Celozzi, “Shielding properties of a wire-medium screen,” *IEEE Trans. Electromagn. Compat*., vol. 50, no. 1, pp. 80-88, February 2008.
[25] J. B. Kim and J. H. Byun, “Salisbury screen absorbers of dielectric lossy sheets of carbon nanocomposite laminates,” *IEEE Trans. Electromagn. Compat.*, vol. 54, no. 1, pp. 37-42, February 2012.
[26] R. K. Gao, W. Hoefer, T. S. Low and E. P. Li, “Robust design of electromagnetic wave absorber using the Taguchi method,” *IEEE Trans. Electromagn. Compat*., vol. 55, no. 6, pp. 1076-1083, December 2013.
[27] S. Cui and D. S. Weile, “Application of a parallel particle swarm optimization scheme to the design of electromagnetic absorbers,” *IEEE Trans. Antennas Propagat.*, vol. 53, no. 11, pp. 3616-3624, November 2005.
[28] S. Genovesi, A. Monorchio, R. Mittra and G. Manara, “A sub-boundary approach for enhanced particle swarm optimization and its application to the design of artificial magnetic conductors,” *IEEE Trans. Antennas Propagat*., vol. 55, no. 3, pp. 766-770, March 2007.
[29] J. Kennedy and R. C. Eberhart, “Particle swarm optimization,” *In Proc. IEEE. Int. Neural Networks Conf.*, vol. IV, pp. 1942-1948, 1995.
[30] A. Adly and S. K. Abd-El-Hafiz, “Utilizing particle swarm optimization in the field computation of non-linear magnetic media,” *ACES Journal*, vol. 18, no. 3, pp. 202-209, 2003.
[31] M. Farmahini-Farahani, R. Faraji-Dana and M. Shahabadi, “Fast and accurate cascaded particle swarm gradient optimization method for solving 2-d inverse scattering problems,” *ACES Journal*, vol. 24, no. 5, pp. 511-517, 2009.
[32] W. C. Weng, “Optimal design of an ultra-wideband antenna with the irregular shape on radiator using particle swarm optimization,” *ACES Journal*, vol. 27, no. 5, pp. 427-434, 2012.
[33] C. L. Li, C. H. Huang, C. C. Chiu and C. H. Sun,“Comparison of dynamic differential evolution and asynchronous particle swarm optimization for inverse scattering of a two-dimensional perfectly conducting cylinder,” *ACES Journal*, vol. 27, no. 10, pp. 850-865, 2012.
[34] R. Araneo, S. Celozzi and G. Lovat, “Design of impedance matching couplers for power line communications,” *In Proc. IEEE Electromagn. Compat. Symp.*, pp. 64-69, August 17-21, 2009.
[35] R. Araneo, S. Celozzi, G. Lovat and F. Maradei, “Multiport impedance matching technique for power line communications,” *In IEEE Int. Symp. on Power Line Communications and Its Applications* (ISPLC), pp. 96-101, 2011.
[36] R. Araneo, S. Celozzi, G. Lovat and F. Maradei, “Computer-aided design of coupling units for naval-network power line communications,” *In IEEE Int.Symp. on Industrial Electronics* (ISIE), pp. 2961-2966, 2010.
[37] M. Clerc and J. Kennedy, “The particle swarm: explosion, stability, and convergence in a multi-dimensional complex space,” *IEEE Trans. Evol. Comput.*, vol. 6, pp. 58-73, February 2002.
[38] J. H. Seo, C. H. Im, C. G. Heo, J. K. Kim, H. K. Jung and C. G. Lee, “Multimodal function optimization based on particle swarm optimization,” *IEEE Trans. Magn*., vol. 42, no. 4, pp. 1095-1098, April 2006.
[39] D. K. Woo, J. H. Choi, M. Ali and H. K. Jung, “Anovel multimodal optimization algorithm

applied to electromagnetic optimization," *IEEE Trans. Magn*., vol. 47, no. 6, pp. 1667-1673, June 2011.

Rodolfo Araneo received his M.S. (cum laude) and Ph.D. degrees in Electrical Engineering from the University of Rome "La Sapienza", Rome, in 1999 and 2002, respectively. Araneo received the Past President's Memorial Award in 1999 from IEEE Electromagnetic Compatibility (EMC) Society and won the best conference paper at the 2011 IEEE EMC Symposium. His research activity is mainly in the field of EMC and includes numerical and analytical techniques for modeling high-speed printed circuit boards, shielding and transmission line analysis. He has authored more than 110 papers in international journals and conference proceedings. He is coauthor of the book "Electromagnetic Shielding" published by John Wiley and Sons.

Salvatore Celozzi is Full Professor of Electrical Engineering with the Department of Astronautical, Electrical and Energetic Engineering at the University of Rome "La Sapienza". Celozzi has published more than 120 papers in international journals or conference proceedings, mainly in the fields of electromagnetic shielding and transmission lines. He served as Associate Editor of the IEEE Electromagnetic Compatibility (1995-2000) and authored a book on Electromagnetic Shielding for Wiley in 2008. His current research interests include transmission lines, electromagnetic compatibility, meta- and piezo-materials and numerical methods in electromagnetics.

Bandwidth Improvement of Omni-Directional Monopole Antenna with a Modified Ground Plane

Nasser Ojaroudi [1], Noradin Ghadimi [1] and Yasser Ojaroudi [2]

[1] Young Researchers and Elite Club
Islamic Azad University, Ardabil Branch, Ardabil, Iran
noradin.ghadimi@gmail.com

[2] Young Researchers and Elite Club
Islamic Azad University, Germi Branch, Germi, Iran

Abstract **─** This study introduces a new design of low profile, multi-resonance and omni-directional monopole antenna for Ultra-Wideband (UWB) applications. The proposed antenna configuration consists of an ordinary square radiating patch and a ground plane with pairs of inverted fork-shaped slits and inverted Γ-shaped parasitic structures, which provides a wide usable fractional bandwidth of more than 135%. By cutting a pair of inverted fork-shaped slits in the ground plane and also by inserting a pair of inverted Γ-shaped conductor-backed plane in the feed gap distance, additional resonances are excited and hence much wider impedance bandwidth can be produced; especially at the higher band. By obtaining the third and fourth resonances, the usable lower frequency is decreased from 3.12 GHz to 2.83 GHz and also the usable upper frequency of the presented monopole antenna is extended from 10.3 GHz to 14.87 GHz. The proposed antenna has symmetrical structure with an ordinary square radiating patch; therefore, displays a good omni-directional radiation patterns, even at the higher frequencies. The antenna radiation efficiency is greater than 87% across the entire radiating band. The measured results show that the proposed antenna can achieve the Voltage Standing Wave Ratio (VSWR) requirement of less than 2.0 GHz in frequency range from 2.83 GHz to 14.87 GHz, which is suitable for UWB systems.

Index Terms **─** Omni-directional radiating patterns and printed monopole antenna.

I. INTRODUCTION

After allocation of the frequency band from 3.1 GHz to 10.6 GHz for the commercial use of Ultra-Wideband (UWB) systems by the Federal Communication Commission (FCC) [1], ultra-wideband systems have received phenomenal gravitation in wireless communication. Designing an antenna to operate in the UWB frequency range is quite a challenge, because it has to satisfy the requirements such as ultra-wide impedance bandwidth, omni-directional radiation pattern, constant gain, high radiation efficiency, constant group delay, low profile, easy manufacturing, etc. [2]. In UWB communication systems, one of key issues is the design of a compact antenna while providing wideband characteristic over the whole operating band. Consequently, a number of microstrip antennas with different geometries have been experimentally characterized [3-4]. Some methods are used to obtain the multi-resonance function in the literature [5-8].

In this paper, a different method is proposed to obtain the very wideband bandwidth for the compact monopole antenna. In the proposed antenna, we use pairs of inverted fork-shaped slits and Γ-shaped conductor-backed plane in the ground plane, which provides a wide usable fractional bandwidth of more than 135%. Regarding Defected Ground Structures (DGS) theory, the creating slits in the ground plane provide additional current paths. Moreover, these structures change the inductance and capacitance of the input impedance, which in turn leads to change the bandwidth [9-11]. Therefore, by cutting a pair of inverted fork-shaped slits in the ground plane, much enhanced impedance bandwidth may be achieved. In addition, based on Electromagnetic Coupling Theory (ECT), by adding a pair of inverted Γ-shaped conductor-

Submitted On: December 8, 2013
Accepted On: March 2, 2014

backed plane in the air gap distance, additional coupling is introduced between the bottom edge of the square patch and the ground plane and its impedance bandwidth is improved without any cost of size or expense. Good VSWR and radiation pattern characteristics are obtained in the frequency band of interest. The designed antenna has a small size of 12×18 mm^2.

II. MICROSTRIP ANTENNA DESIGN

The presented small monopole antenna fed by a microstrip line is shown in Fig. 1, which is printed on an FR4 substrate of thickness of 1.6 mm, permittivity of 4.4 and loss tangent 0.018.

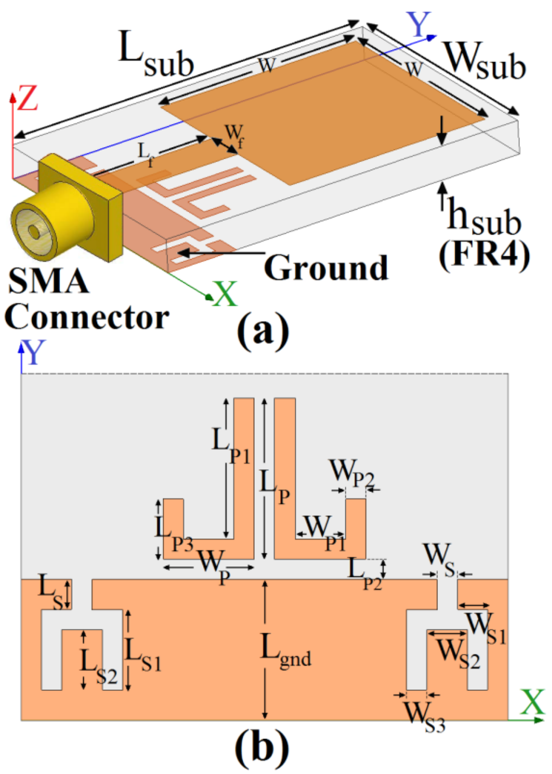

Fig. 1. Geometry of proposed omni-directional monopole antenna: (a) side view and (b) modified ground plane.

The basic monopole antenna structure consists of a square radiating patch, a feed line and a ground plane. The square radiating patch has a width W. The patch is connected to a feed line of width W_f and length L_f. The width of the microstrip feed line is fixed at 2 mm, as shown in Fig. 1. On the other side of the substrate, a conducting ground plane with two inverted fork-shaped slits and a pair of Γ-shaped parasitic structures is placed. The proposed antenna is connected to a 50-Ω SMA connector for signal transmission.

The DGS applied to a ground plane causes a resonant character of the structure transmission with a resonant frequency controllable by changing the shape and size of the slits [3]. In addition, based on ECT, by using a parasitic structure in air gap distance, an additional coupling is introduced between the bottom edge of the square patch and the ground plane and its impedance bandwidth is improved without any cost of size or expense. Therefore, by cutting two inverted fork-shaped slits and also by embedding a pair of inverted Γ-shaped parasitic structures and carefully adjusting these parameters, much enhanced impedance bandwidth may be achieved. The final values of proposed design parameters are displayed in Table 1.

Table 1: The final values of proposed design parameters

$W_{sub} = 12mm$	$L_{sub} = 18mm$	$h_{sub} = 1.6mm$
$W_f = 2mm$	$L_f = 7mm$	$W = 10mm$
$W_S = 0.5mm$	$L_S = 0.5mm$	$W_{S1} = 0.75mm$
$L_{S1} = 2.5mm$	$W_{S2} = 1mm$	$L_{S2} = 2mm$
$W_{S3} = 0.5mm$	$W_P = 2.25mm$	$L_P = 3.5mm$
$W_{P1} = 125mm$	$L_{P1} = 3mm$	$W_{P2} = 0.5mm$
$L_{P2} = 0.5mm$	$L_{P3} = 0.75mm$	$L_{gnd} = 3.5mm$

III. RESULTS AND DISCUSSIONS

The proposed microstrip monopole antenna with various design parameters was constructed and the numerical and experimental results of input impedance and radiation characteristics are presented and discussed. Ansoft HFSS simulations are used to optimize the design and agreement between the simulation and measurement is obtained [11].

Figure 2 shows the structure of the various antennas used for simulation studies. VSWR characteristics for ordinary square patch antenna (Fig. 2 (a)), square antenna with a pair of inverted fork-shaped slits (Fig. 2 (b)) and the proposed antenna (Fig. 2 (c)) are compared in Fig. 3. As shown in Fig. 3, in the proposed antenna configuration, the ordinary square monopole can provide the fundamental and next higher resonant radiation band at 4.8 GHz and 8.2 GHz, respectively; in the absence of the inverted fork-shaped slits and a pair of inverted Γ-shaped conductor-backed plane. It is observed that by using these modified elements including pairs of inverted fork-shaped slits and Γ-shaped conductor-backed plane, additional third (10.9 GHz) and fourth (14.2 GHz) resonances are excited, respectively, and hence the bandwidth is increased. As illustrated in Fig. 3, the embedded structures in the ground plane and also the generation of extra resonances have an effect of disappear for the second resonance of the antenna. This is because the coupling between the ground plane and radiating patch for the second resonance becomes weaker.

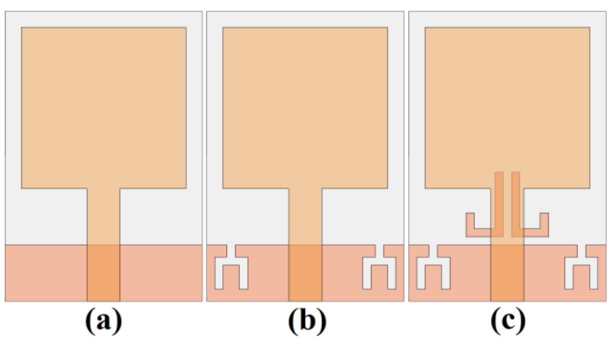

Fig. 2. (a) Ordinary square monopole antenna, (b) the antenna with a pair of inverted fork-shaped slits in the ground plane and (c) the proposed monopole antenna.

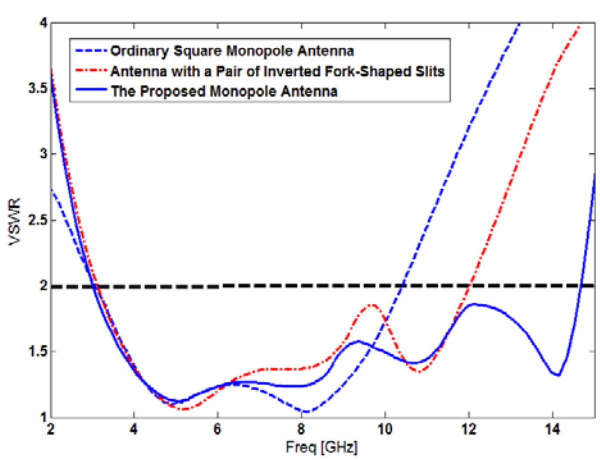

Fig. 3. Simulated VSWR characteristics for the various monopole antennas shown in Fig. 2.

In order to understand the phenomenon behind these additional resonances performance, the simulated current distributions on the ground plane for the proposed antenna at 10.9 GHz and 14.5 GHz (third and fourth resonances) are presented in Figs. 4 (a) and (b), respectively. As shown in Fig. 4 (a), the currents concentrated on the edges of the interior and exterior of the inverted fork-shaped slits at third resonance frequency (10.9 GHz). Also, as illustrated in Fig. 4 (b), the current concentrated on the edges of the interior and exterior of the inverted Γ-shaped parasitic structures at fourth resonance frequency (14.2 GHz).

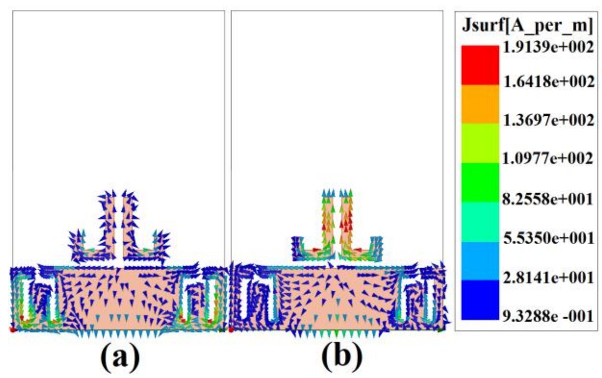

Fig. 4. Simulated surface current distributions on the ground plane for the proposed antenna: (a) at 10.9 GHz and (b) at 14.2 GHz.

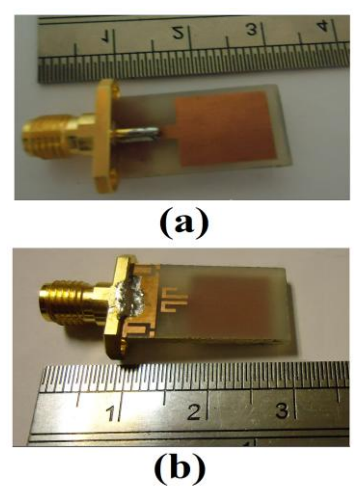

Fig. 5. Photograph of the realized printed monopole antenna: (a) top view and (b) bottom view.

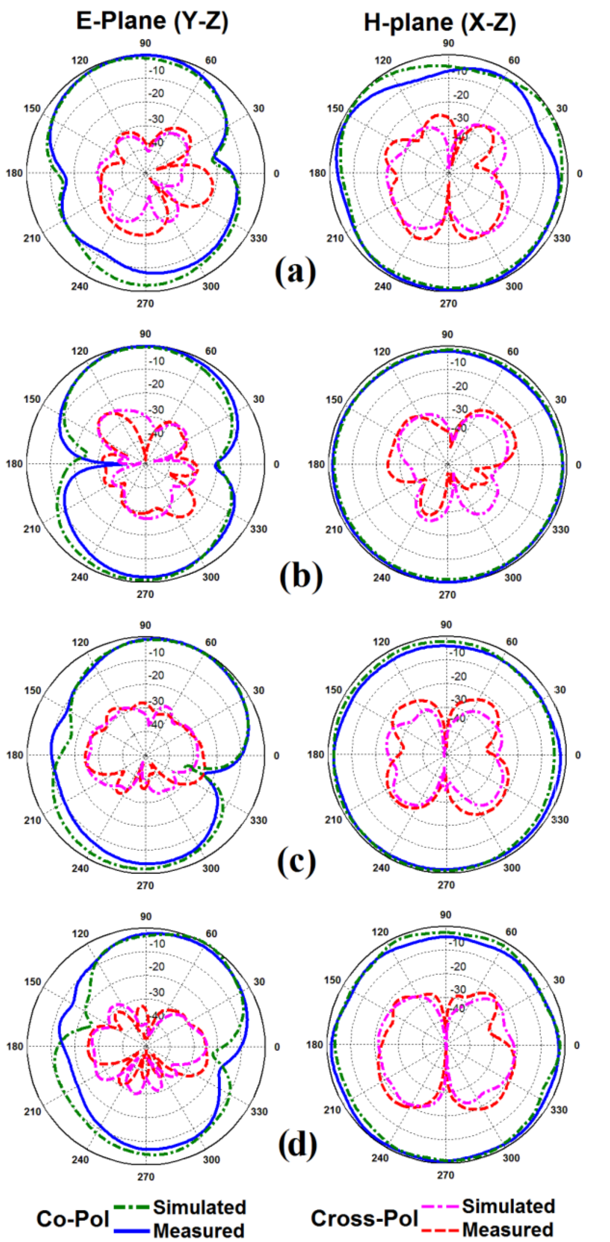

Fig. 6. Measured and simulated radiation patterns of the proposed antenna: (a) 5 GHz, (b) 8 GHz, (c) 11 GHz and (d) 14 GHz.

As shown in Fig. 5, the proposed antenna was fabricated and tested. The VSWR characteristic of the antenna was measured using a network analyzer in an anechoic chamber. The radiation patterns have been measured inside an anechoic chamber using a double-ridged horn antenna as a reference antenna placed at a distance of 2 m. Also, a two-antenna technique using a spectrum analyzer and a double-ridged horn antenna as a reference antenna placed at a distance of 2 m is used to measure the radiation gain in the z axis direction (x-z plane).

Figure 6 depicts the measured and simulated radiation patterns of the proposed antenna, including the co-polarization and cross-polarization in the H-plane (x-z plane) and E-plane (y-z plane). It can be seen that quasi-omni-directional radiation pattern can be observed on x-z plane over the whole UWB frequency range, especially at the low frequencies. The radiation pattern on the y-z plane displays a typical figure-of-eight, similar to that of a conventional dipole antenna. It should be noticed that the radiation patterns in E-plane become imbalanced as frequency increases because of the increasing effects of the cross-polarization. The patterns indicate at higher frequencies and more ripples can be observed in both E and H-planes, owing to the generation of higher-order modes [14-16].

Figure 7 shows the measured and simulated VSWR characteristics of the proposed antenna. The fabricated antenna has the frequency band of 2.83 GHz to 14.87 GHz.

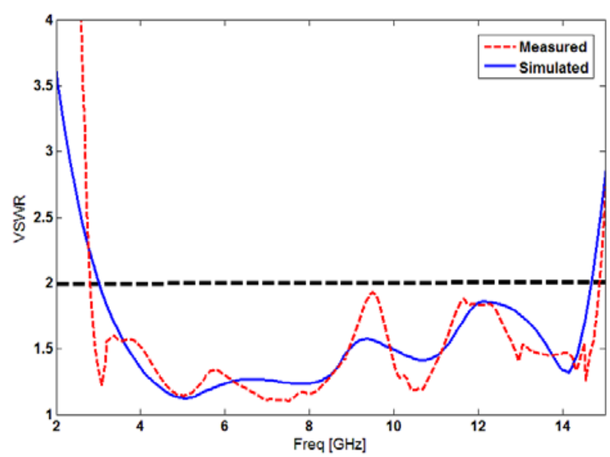

Fig. 7. Measured and simulated VSWR characteristics of the proposed monopole antenna.

The simulated radiation efficiency characteristic of the proposed antenna is shown in Fig. 8. Results of the calculations using the software HFSS indicated that the proposed antenna features a good efficiency, being greater than 87% across the entire radiating band. In addition, the simulated and measured maximum gains of the antenna against frequency are illustrated in Fig. 8.

The antenna gain has a flat property, which increases by the frequency. As seen, the proposed antenna has sufficient and acceptable gain levels in the operation bands [17-18].

In the UWB communication systems, antennas should be able to transmit the electrical pulse with minimal distortion. If group delay variation exceeds more than 1 *ns*, phases are no more linear in far field and phase distortion occurs, which can cause a serious problem for UWB applications. Figure 9 shows the simulated group delay property of the proposed monopole antenna. As illustrated, the variation is less than 0.25±0.4 over the frequency band from 3 GHz to 14.5 GHz. It shows that the antenna has low-impulse distortion and is suitable for UWB applications [18-21].

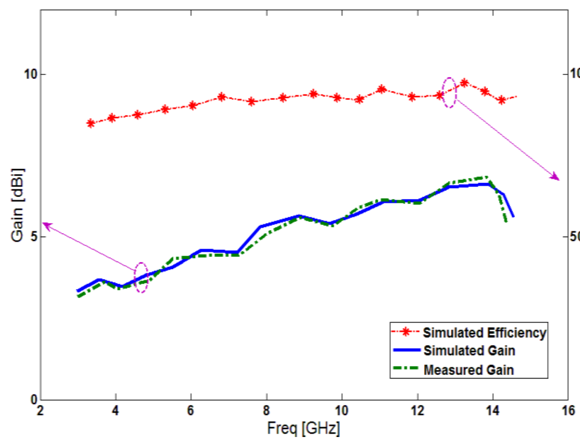

Fig. 8. Measured and simulated radiation efficiency and gain of the proposed antenna.

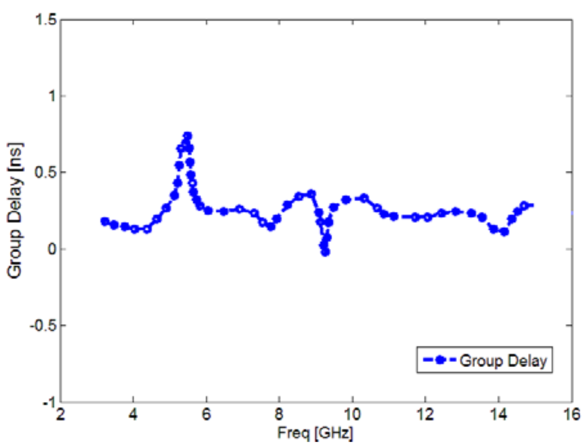

Fig. 9. Simulated group delay characteristic of the proposed antenna.

The radiating mechanism of the proposed antenna is more novel than was explained in previous works. The proposed structure is the combination of the monopole antenna with the dipole and slot antenna. In this study, the modified ground-plane structure is the combination of the monopole antenna and the slot antenna. By using the modified conductor-backed plane, the interaction of the two parts of the overall antenna has occurred. The embedding parasitic structure in the ground plane of the monopole antenna acts as a dipole antenna that can provide an additional current path. Also, the entire back conducting plane could be part of the radiator, especially when operating at lower frequencies [22-24].

Table 2: Comparison of previous designs with the proposed antenna

Ref.	FBW (%)	Dimension (mm)	Gain (dBi)
[13]	47%	33×33	3.5~6
[14]	87%	22×24	1~5.5
[15]	87%	32×25	2~5.5
[16]	91%	26×26	3-7
[17]	112%	20×20	2~4.7
[18]	118%	40×10	2.3~6.3
[19]	130%	12×18	2.7-5.5
[20]	132%	25×26	not reported
This Work	*136%*	*12×18*	*3.3~6.5*

Table 2 summarizes the previous designs and the proposed antenna. As seen, the proposed antenna has a compact size with very wide bandwidth in comparison with the pervious works. In addition, the proposed antenna has good omni-directional radiation patterns with low cross-polarization level, even at the higher and upper frequencies. As the proposed antenna has symmetrical structure and an ordinary square radiating patch without any slot and parasitic structures at top layer, in comparison with previous multi-resonance UWB antennas, the proposed antenna displays a good omni-directional radiation pattern, even at lower and higher frequencies [20]. Also, the proposed microstrip-fed monopole antenna has sufficient and acceptable radiation efficiency, group delay and antenna gain levels in the operation bands [25-27].

IV. CONCLUSION

In this manuscript, a novel compact Printed Monopole Antenna (PMA) with multi-resonance characteristics has been proposed for UWB applications. The fabricated antenna can operate from 2.83 GHz to 14.87 GHz. In order to enhance the bandwidth, we insert a pair of inverted fork-shaped slits in the ground plane and also by adding two inverted Γ-shaped conductor-backed plane with variable dimensions, additional resonances are excited and hence much wider impedance bandwidth can be produced. The designed antenna has a simple configuration with small size of 12×18 mm^2 and an ordinary square radiating patch, which its radiation efficiency is greater than 87%. Simulated and experimental results show that the proposed antenna could be a good candidate for UWB systems application.

ACKNOWLEDGMENT

The authors are thankful to Microwave Technology (MWT) Company staff, for their beneficial and professional help (www.microwave-technology.com).

REFERENCES

[1] *FCC News release, FCC NEWS (FCC 02-48)*, February 14, 2002.
[2] D. Cheng, "Compact ultra-wideband microstrip resonating antenna," *US patent7872606*, January 2011.
[3] M. Mighani, M. Akbari and N. Felegari, "A novel SWB small rhombic microstrip antenna with parasitic rectangle into slot of the feed line," *Applied Computational Electromagnetics Society (ACES) Journal*, vol. 27, no. 1, pp. 74-79, January 2012.
[4] M. N. Jahromi and N. K. Barchloui, "Analysis of the behavior of Sierpinski carpet monopole antenna," *Applied Computational Electromagnetics Society (ACES) Journal*, vol. 24, no. 1, pp. 32-36, February 2009.
[5] W. C. Weng, "Optimal design of an ultra-wideband antenna with the irregular shape on radiator using particle swarm optimization," *Applied Computational Electromagnetics Society (ACES) Journal*, vol. 27, no. 5, pp. 427-434, May 2012.
[6] G. Zhang, J. S. Hong, B. Z. Wang and G. Song, "Switched band-notched UWB/WLAN monopole antenna," *Applied Computational Electromagnetics Society (ACES) Journal*, vol. 27, no. 3, pp. 256-260, March 2012.
[7] R. Azim, M. T. Islam and N. Misran, "Design of a planar UWB antenna with new band enhancement technique," *Applied Computational Electromagnetics Society (ACES) Journal*, vol. 26, no. 10, pp. 856-862, October 2011.
[8] C. Y. D. Sim, W. T. Chung and C. H. Lee, "Planar UWB antenna with 5 GHz band rejection switching function at ground plane," *Progress In Electromagnetics Research*, vol. 106, pp. 321-333, 2010.
[9] N. Behdad and K. Sarabandi, "A compact antenna for ultra-wideband applications," *IEEE Transactions on Antennas and Propagation*, vol. 53, pp. 2185-2192, 2005.
[10] A. J. Kerkhoff, R. L. Rogers and H. Ling, "Design and analysis of planar monopole antennas using a genetic algorithm approach," *IEEE Trans Antennas Propag*., vol. 2, pp. 1768-1771, 2004.
[11] Ansoft high frequency structure simulation (HFSS), ver. 13, *Ansoft Corporation*, 2010.
[12] K. Chung, T. Yun and J. Choi, "Wideband CPW-fed monopole antenna with parasitic elements and slots," *ElectronicsLetters*, vol. 40, no. 17, pp. 1038-1040, 2004.
[13] W. L. Chen, G. M. Wang and C. X. Zhang, "Bandwidth enhancement of a microstrip-line-fed printed wide-slot antenna with a fractal-shaped slot," *IEEE Transactions on Antennas and Propagation*, vol. 57, pp. 1276-2179, 2009.
[14] R. Azim, M. T. Islam and N. Misran, "Compact tapered-shape slot antenna for UWB applications," *IEEE Antennas and Wireless Propagation Letters*, vol. 10, pp. 1190-1193, 2011.
[15] Y. Li, W. Li and Y. Lu, "A switchable UWB slot antenna using SIS-HSIR and SIS-SIR for multi-mode wireless communications applications," *Applied Computational Electromagnetics Society (ACES) Journal*, vol. 27, pp. 340-351, 2012.
[16] L. Liu, S. W. Cheung and T. I. Yuk, "Compact MIMO antenna for portable devices in UWB applications," *IEEE Transactions on Antennas and Propagation*, vol. 61, pp. 4257-4264, 2013.
[17] M. Ojaroudi and N. Ojaroudi, "Ultra-wideband small rectangular slot antenna with variable band-stop function," *IEEE Trans. Antennas Propag*., vol. 62, pp. 490-494, 2014.
[18] X. N. Low, Z. N. Chen and T. S. P. See, "A UWB dipole antenna with enhanced impedance and gain performance," *IEEE Transactions on Antennas and Propagation*, vol. 57, pp. 2966-2959, 2009.
[19] N. Ojaroudi and M. Ojaroudi, "Small monopole antenna with multi-resonance characteristic by using rotated t-shaped slit and parasitic structure for UWB systems," *Microw. Opt. Technol. Lett*., vol. 55, pp. 482-485, 2013.

[20] A. K. Gautam, S. Yadav and B. K. Kanaujia, “A CPW-fed compact UWB microstrip antenna,” *IEEE Antennas and Wireless Propagation Letters*, vol. 12, pp. 151-154, 2013.
[21] N. Ojaroudi, “Design of ultra-wideband monopole antenna with enhanced bandwidth,” *21st Telecommunications Forum,* TELFOR 2013, Belgrade, Serbia, pp. 1043-1046, November 27-28, 2013.
[22] N. Ojaroudi, “A new eesign of koch fractal slot antenna for ultra-wideband applications,” *21st Telecommunications Forum,* TELFOR 2013, Belgrade, Serbia, pp. 1051-1054, November 27-28, 2013.
[23] N. Ojaroudi, “Compact UWB monopole antenna with enhanced bandwidth using rotated l-shaped slots and parasitic structures,” *Microw. Opt. Technol. Lett.*, vol. 56, pp. 175-178, 2014.
[24] N. Ojaroudi, S. Amiri and F. Geran, “A novel design of reconfigurable monopole antenna for UWB applications,” *Applied Computational Electromagnetics Society (ACES) Journal*, vol. 28, no. 6, pp. 633-639, July 2013.
[25] N. Ojaroudi, “Application of protruded strip resonators to design an UWB slot antenna with WLAN band-notched characteristic,” *Progress in Electromagnetics Research C*, vol. 47, pp. 111-117, 2014.
[26] N. Ojaroudi, “Microstrip monopole antenna with dual band-stop function for UWB applications,” *Microw. Opt. Technol. Lett*., vol. 56, pp. 818-822, 2014.
[27] N. Ojaroudi, “Small microstrip-fed slot antenna with frequency band-stop function,” *21st Telecommunications Forum*,” TELFOR 2013, Belgrade, Serbia., pp. 1047-1050, November 27-28, 2013.

Compact Microstrip Lowpass Filter with Ultra-Wide Stopband using Stepped-Impedance Trapezoid Resonators

G. Zhang, J. Wang, Y. Dou, and H. Cui

Ministerial Key Laboratory of JGMT,
Nanjing University of Science and Technology, Nanjing 210094, China
elegzhang@gmail.com, elejpwang@gmail.com, eledouy@gmail.com, elehfc@gmail.com

Abstract **—** A new microstrip lowpass filter with compact size and ultra-wide stopband is presented. The resonance properties of a microstrip main transmission line parallel loaded with the stepped-impedance trapezoid resonator are studied. Analysis results reveal that a compact size and ultra-wide stopband lowpass filter can be realized by properly introducing multiple stepped-impedance trapezoid resonators in the design. A demonstration filter with 3 dB cutoff frequency at 0.8 GHz has been designed, fabricated, and measured. Results indicate that the proposed filter is able to suppress the 17^{th} harmonic response by 15 dB, together with a small size of 0.057 λg $\times$0.077 λg, where λg is the guided wavelength at 0.8 GHz.

Index Terms **—** Compact, lowpass filter, microstrip, trapezoid resonator, and ultra-wide.

I. INTRODUCTION

Planar lowpass filters with compact size and high performance are in great demand for modern wireless communication systems to suppress harmonics and spurious signals. Conventional lowpass filters using shunt stubs or high-low impedance transmission lines have been widely used in microwave systems for their excellent characteristics [1]. However, compact size and high performance are hard to achieve simultaneously. Therefore, many works report attempts to achieve both size reduction and performance enhancement [2–11].

In general, there are two methods to design a lowpass filter with compact size and wide stopband. The first method is to form a lowpass filter by cascading multiple resonators [2-5]. With this method, Li et al. designed a lowpass filter by cascading multi-radial patch resonators [2]. Although, sharp roll-off was achieved, the size of the filter was relatively large and only the 6^{th} harmonic response was suppressed. A microstrip lowpass filter with low insertion loss and sharp roll-off was proposed by cascading modified semi-circlar and semi-elliptical microstrip patch resonators [3]. However, the circuit size and passband performance still need improvement. Therefore, to further improve the stopband performance, Ma et al. proposed a lowpass filter by cascading LC resonant structures and transformed radial stubs. Although, better than 13^{th} harmonic suppression was realized, this method increased design complexity and circuit area [4]. As for the work reported in [5], a microstrip lowpass filter with compact size and ultra-wide stopband had been achieved but at the cost of a relatively complex circuit design. The second method is to design a lowpass filter by using modified stepped impedance hairpin resonators [6-8]. Using stepped impedance hairpin resonators with radial stubs, Wei et al., proposed a lowpass filter with 7^{th} harmonic suppression performance [6]. Although, a compact design had been realized with this method, further improvement should be carried out in stopband bandwidth. The stopband performance should also be improved in [7], as the compact lowpass filter using a coupled-line hairpin unit, one spiral slot, and two open stubs only achieve 10 dB attenuation up to 20 GHz inside the stopband. A very wide stopband lowpass filter is achieved with a novel application of shunt open-stubs at the feed points of a center fed coupled-line hairpin resonator [8], but the

Submitted On: April 17, 2013
Accepted On: February 2, 2014

reflection loss is relatively large. In addition, using defected ground structure is also a popular and useful way [9-11]. A lowpass filter composed of semi-circlar defected ground structures and semi-circlar stepped-impedance shunt stubs is proposed in [9], which increases the circuit complexity and circuit size.

The motivation of this paper is to design a new microstrip lowpass filter with both compact size and ultra-wide stopband. To achieve compact size and ultra-wide stopband rejection, stepped-impedance trapezoid resonators are introduced and parallel loaded on the main transmission line of the filter. A demonstration filter with 3 dB cutoff frequency at 0.8 GHz has been designed, fabricated, and measured. Measured results indicate that the designed filter has an ultra-wide stopband with better than 15 dB suppression up to 13.7 GHz. Furthermore, the size of the filter is only 11.6 × 15.7 mm^2, which corresponds to a compact electrical size of 0.057 λ_g × 0.077 λ_g, where λ_g is the guided wavelength at 0.8 GHz.

II. FILTER DESIGN

Figure 1 shows the layout of the proposed lowpass filter, which is composed of a high impedance microstrip main transmission line and five stepped-impedance trapezoid resonators. Each stepped-impedance trapezoid resonator is composed of a high impedance transmission line and a trapezoidal patch, which are connected in series. Figure 2 shows the lumped-element equivalent circuit of the presented lowpass filter. In the circuit, the high impedance line is mainly represented by the inductance L_0 and L_1. The symbols C_a, C_b, and C_c mainly represent the capacitances between the resonator 1, 2, 3, and the ground plane, respectivly, while L_a, L_b, and L_c mainly represent the inductances of the high impendance of the stepped-impedance resonator 1, 2, and 3. The symbol C_{bc} means the coupling capacitance between resonators 1 and 3. The capacitor and inductor values of the lumped-element equivalent circuit of the proposed lowpass filter are given as follows: C_a = 4.6 pF, C_b = 1.9 pF, C_c = 6.6 pF, C_{bc} = 0.1 pF, L_0 = 5.6 nH, L_1=15.8 nH, L_a=0.9 nH, L_b=0.92 nH, and L_c=0.27 nH.

To illustrate the design theory of the proposed filter, frequency responses of four stepped-impedance rectangular trapezoid resonators and one stepped-impedance isosceles trapezoid resonator have been studied, respectively. As can be seen from Fig. 3 (a), a microstrip main transmission line with only two stepped-impedance rectangular trapezoid resonators, i.e., resonator 1, exhibits a wide stopband together with one transmission pole (TP) at about 4.4 GHz. In order to suppress the undesired frequency response, another two stepped-impedance rectangular trapezoid resonators, i.e., resonator 2, are also introduced to the design.

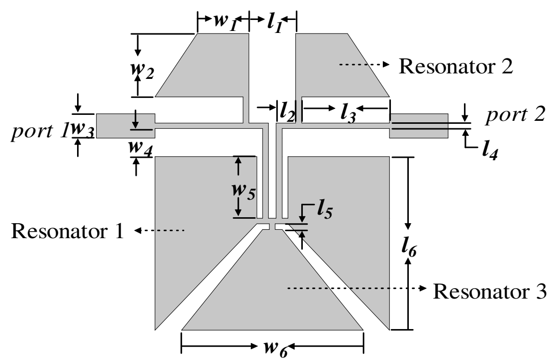

Fig. 1. Layout of proposed lowpass filter.

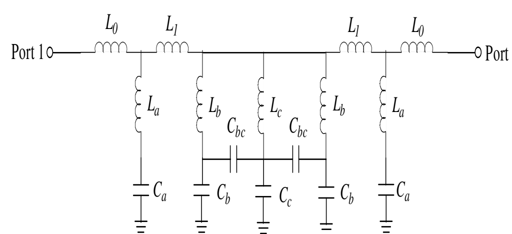

Fig. 2. Lumped-element equivalent circuit of the proposed lowpass filter.

Figure 3 (b) investigates the resonant properties of the stepped-impedance trapezoid resonators. It can be seen that one transmission zero (TZ) at about 4.4 GHz in the stopband is achieved. This transmission zero is caused by the resonance of loaded stepped-impedance trapezoid resonators and its frequency location can be controlled by the structure parameters of the stepped-impedance trapezoid resonators. Based on the investigation mentioned above, if we can properly combine the four stepped-impedance rectangular trapezoid resonators in a filter, the mutual suppression of spurious passbands and thereby a better stopband performance is expected to be achieved. Figure 3 (c) shows the frequency response of the filter with four stepped-impedance rectangular trapezoid resonators, i.e., resonators 1 and 2. As expected, by locating the transmission zero in Fig. 3 (b) around the position of spurious response appeared at about 4.4 GHz in Fig. 3 (a), we finally achieve the new lowpass filter with an enhanced stopband performance.

In order to achieve sharp roll-off rate, one stepped-impedance isosceles trapezoid resonator, i.e., resonator 3, is also introduced to the filter. It is can be seen in Fig. 3 (d) a sharp roll-off rate is achieved by the adoption of resonator 3. Therefore, if we properly combine the three types of stepped-impedance trapezoid resonators, i.e., resonators 1, 2, and 3, in one filter, a compact microstrip lowpass filter with ultra-wide stopband can be realized.

The new lowpass filter is designed and fabricated based on the analysis mentioned above. The structure parameters are as follows: l_1 = 2.2 mm, l_2 = 0.9 mm, l_3 = 4.5 mm, l_4 = 0.2 mm, l_5 = 0.2 mm, l_6 = 9.3 mm, w_1 = 2.6 mm, w_2 = 3.4 mm, w_3 = 1.16 mm, w_4 = 1.4 mm, w_5 = 3.4 mm, and w_6 = 9.3 mm, The substrate used here has a relative dielectric constant of 3.38 and a thickness of 0.508 mm. Figure 4 is the photograph of the proposed lowpass filter.

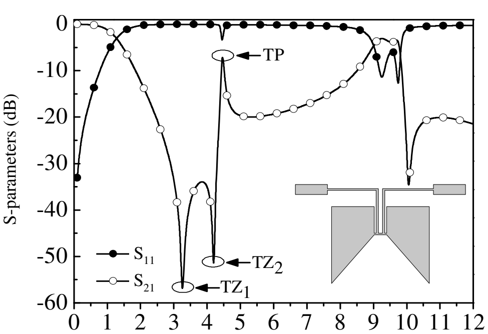

(a)

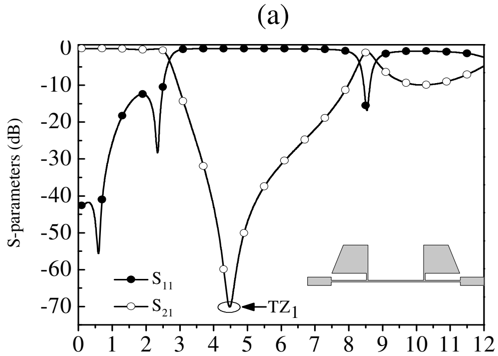

(b)

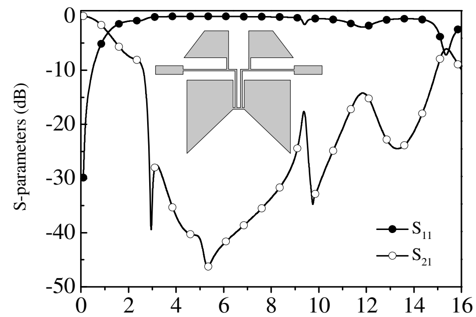

(c)

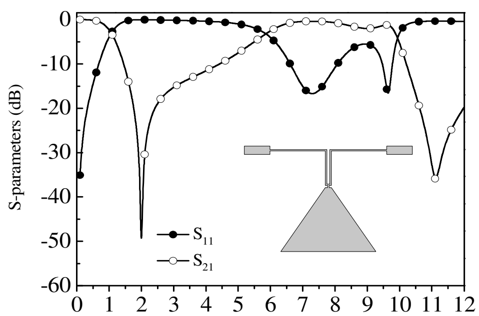

(d)

Fig. 3. Simulated S-parameters of the studied resonators; a) filter with stepped-impedance rectangular trapezoid resonator 1, b) filter with stepped-impedance rectangular trapezoid resonator 2, c) filter with stepped-impedance rectangular trapezoid resonator 1 and 2, and d) filter with stepped-impedance isosceles trapezoid resonator 3.

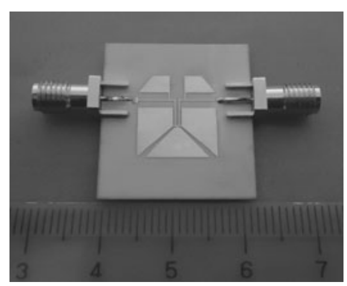

Fig. 4. Photograph of the proposed lowpass filter.

III. SIMULATION AND MEASUREMENT RESULTS

Simulation was accomplished by using EM simulation software ANSOFT HFSS 12. The comparisons among the circuit model EM simulated results and the equivalent lumped element circuit results are given in Fig. 5.

Measurement was carried out on an Agilent 8722ES network analyser. Figure 6 shows the simulated and measured results, which are in good agreement. As can be observed from Fig. 6, the measured 3 dB cutoff frequency f_c is located at 0.8 GHz, as expected. Figure 6 also shows that the spurious frequencies suppressed by better than 15 dB from 2.36 GHz up to 13.7 GHz. Thus, the proposed filter has a property of 17^{th} harmonic suppression. Furthermore, the proposed filter exhibits a small electrical size of 0.057 $\lambda_g \times$ 0.077 λ_g, where λ_g is the guided wavelength at 0.8 GHz. For comparison, Table I summarizes the performance of some published lowpass filters. As can be seen from the table, our proposed filter has the properties of compact size, simple circuit topology, and ultra-wide stopband among the quoted filters.

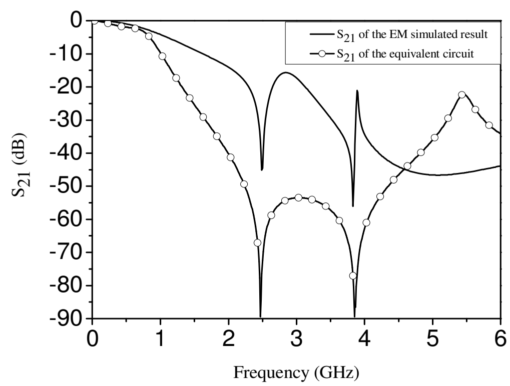

Fig. 5. Comparisons among the equivalent circuit model calculated results and EM simulated results.

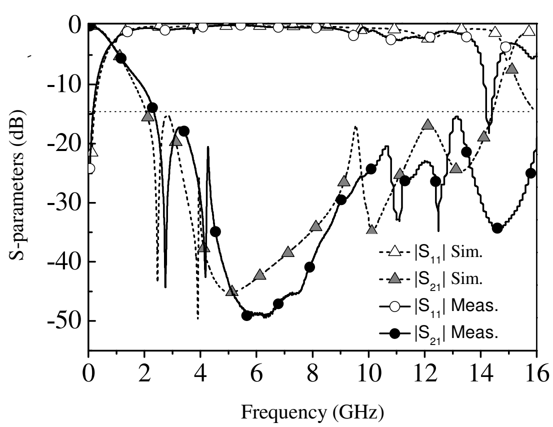

Fig. 6. Simulated and measured S-parameters of the proposed filter.

Table I: Performance comparisons among published filters and proposed ones.

Ref.	Harmonic suppression	Cutoff frequency(GHz)	Circuit size
2	6^{th}	2.4	$0.351\lambda_g \times 0.106\lambda_g$
3	6^{th}	3.12	$0.395\lambda_g \times 0.151\lambda_g$
4	13^{th}	3	$0.310\lambda_g \times 0.240\lambda_g$
5	16^{th}	1	$0.111\lambda_g \times 0.091\lambda_g$
6	7^{th}	1.67	$0.104\lambda_g \times 0.104\lambda_g$
7	10^{th}	2	$0.101\lambda_g \times 0.150\lambda_g$
8	9^{th}	0.5	$0.104\lambda_g \times 0.214\lambda_g$
9	5^{th}	2.7	$0.134\lambda_g \times 0.323\lambda_g$
This work	17^{th}	0.8	$0.057\lambda_g \times 0.077\lambda_g$

IV. CONCLUSION

A new microstrip lowpass filter is presented in this letter. One prototype filter with 3 dB cutoff frequency at 0.8 GHz has been demonstrated. Results indicate that the demonstrator has the properties of compact size, good passband performance, and ultra-wide stopband. With all these good features, the proposed filter is applicable for modern communication systems.

ACKNOWLEDGMENT

This work was supported by the Nature Science Foundation of China under Grant No.61101047 and the Specialized Research Fund for the Doctoral Program by the Ministry of Education of China under Grant No.20113219120015.

REFERENCES

[1] D. Pozar, *Microwave Engineering*, Wiley, USA, pp. 412-415, 2005.

[2] J.-L. Li, S.-W. Qu, and Q. Xue, “Compact microstrip lowpass filter with sharp roll-off and wide stop-band,” *IEE Electron. Lett.*, vol. 45, no. 2, pp. 110-111, Jan. 2009.

[3] M. Hayati, A. Sheikhi, and A. Lotfi, “Compact lowpass filter with wide stopband using modified

semi-elliptic and semi-circular microstrip patch resonator," *IEE Electron. Lett.*, vol. 46, no. 22, pp. 1507-1509, Oct. 2010.
[4] K. Ma and K. Yeo, "New ultra-wide stopband lowpass filter using transformed radial stubs," *IEEE Trans. Microw. Theory Tech.*, vol. 59, no. 3, pp. 604-611, Mar. 2011.
[5] J. Wang, H. Cui, and G. Zhang, "Design of compact microstrip lowpass filter with ultra-wide stopband," *IEE Electron. Lett.*, vol. 48, no. 14, pp. 854-856, July 2012.
[6] X. Wei, P. Wang, M. Liu, and Y. Shi, "Compact wide-stopband lowpass filter using stepped impedance hairpin resonator with radial stubs," *IEE Electron. Lett.*, vol. 47, no. 15, pp. 862-863, July 2011.
[7] F. Wei, L. Chen, and X.-W. Shi, "Compact lowpass filter based on coupled-line hairpin unit," *IEE Electron. Lett.*, vol. 48, no. 7, pp. 379-381, Mar. 2012.
[8] V. Velidi and S. Sanyal, "Sharp roll-off lowpass filter with wide stopband using stub-loaded coupled-line hairpin unit," *IEEE Microw. Wirel. Compon. Lett.*, vol. 21, no. 6, pp. 301-303, June 2011.
[9] F. Wei, X.-W. Shi, B. Li, Q. Huang, and X. Wang, "Design of a compact microstrip low-pass filter using defected ground structure," *Microwave Opt. Technol. Lett.*, vol. 50, no. 12, pp. 3157-3160, Dec. 2008.
[10] G. Al-Omair, S. Mahmoud, and A. Al-Zayed, "Lowpass and bandpass filter designs based on DGS with complementary split ring resonators," *Applied Computational Electromagnetic Society (ACES) Journal*, vol. 26, no. 11, pp. 907-914, Nov. 2011.
[11] M. Challal, A. Boutejdar, M. Dehmas1, A. Azrar, and A. Omar, "Compact microstrip low-pass filter design with ultra-wide reject band using a novel quarter-circle DGS shape," *Applied Computational Electromagnetic Society (ACES) Journal*, vol. 27, no. 10, pp. 808-815, Oct. 2012.

Gang Zhang received the B.S. degree in Electronics and Information Engineering from NJUST, Nangjing, China, in 2010. He is currently working toward the Ph.D. degree in Electromagnetic Field and Microwave Technology in NJUST. His research interest is the design of miniaturized high performance microwave/millimeter-wave passive device and numerical methods in electromagnetics.

Jianpeng Wang received the M. Sc. and Ph. D. degree from UESTC, Chengdu, China, in 2004, and 2007, respectively, both in Electronic Engineering. Since January 2008, he has been with the Ministerial Key Laboratory of JGMT, School of Electronic and Optical Engineering, NJUST, where he is currently an Associate Professor. His research interests include the high performance microwave/millimeter-wave passive components, circuits and systems realized on PCB, LTCC, etc.

Yan Dou received the B.S. degree in Electronics and Information Engineering from Anhui University, Hefei, China, in 2011. She is currently working toward the Master's degree in Electromagnetic Field and Microwave Technology in NJUST. Her research interest is the design of miniaturized high performance microwave passive device.

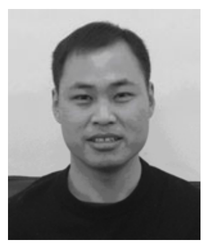

Haifei Cui received the B.S. degree in Electronics and Information Engineering from Anhui University, Hefei, China, in 2008. He is currently working toward the Ph.D. degree in Electromagnetic Field and Microwave Technology in NJUST. His research interest is the design of miniaturized high performance microwave passive device.

Optimization of Interior Permanent Magnet Motor on Electric Vehicles to Reduce Vibration Caused by the Radial Force

L. Y. Xiang, S. G. Zuo, L. C. He, M. H. Zhang, J. J. Hu, and G. Long

Clean Energy Automotive Engineering Center
Tongji University, Shanghai 201804, China
xlongyang10@126.com, sgzuo@tongji.edu.cn, helvchang2006@163.com, zsyzmh@126.com, ericaj@126.com, longguo.111@163.com

Abstract **–** The vibration and noise level of a driven motor on electric vehicles has a great influence on the overall comfort of the whole vehicle. In this paper, the main vibrational harmonic waves with high amplitudes of Interior Permanent Magnet (IPM) motor were investigated via an experiment. In order to lower the amplitudes of these harmonic waves, the paper carries out the optimization of radial force of the IPM motor based on the parameter sensitivity analysis and also implemented the structural optimization, according to the dynamic response of the stator. The final dynamic simulation of the optimized model excited by the optimized radial force, show that the optimization results in a better performance of the vibration behaviors. This study could provide some guidelines for the optimal design of the interior permanent magnet motor to reduce vibration.

Index Terms **–** Interior permanent magnet motor, radial force optimization, stator structural optimization and vibration behavior.

I. INTRODUCTION

An electric vehicle is one of the energy-saving and environmental-friendly transportation tools. The driven motor is one of the most important parts on an electric vehicle. However, the vibration and noise of the motors on vehicles is more serious than that of normal ones, which has a bad influence on the comfort of the vehicle. Thus it is necessary to conduct the study of the causes, factors and optimization of the vibration behaviors of the driven motors on electric vehicles. Interior Permanent Magnet (IPM) motors are most often used to drive the electric vehicles. For this kind of motor, the radial force inside stimulates the stator, which leads to the vibration and noise [1]. Accordingly, the existing studies on the vibration of IPM motors mainly focuses on the calculation and analysis of the radial force and the vibration modes of the stator.

Zhu is one of the earliest scholars to study the vibration and noise characteristics of permanent magnet motors. In his study, the instantaneous magnetic field distribution of brushless permanent magnet DC motor was calculated and the effects of four factors were analyzed: open-circuit field, armature-reaction field, stator slotting and loads. The results of analytical method agreed with the ones of finite element method [2]-[5], which laid the theoretical foundation of the calculation of the radial force; although, he didn't study the vibrational optimization of the motor. In the 21st century, the electromagnetic numerical method finite element method, as an example, is used more often for the motor analysis. Chen made use of finite element method to analyze the relationship between the radial force and stator teeth, width of rotor back iron and slot opening of the permanent magnet brushless motor. He found that the lower amplitudes of the radial forces resulted from larger stator teeth width, smaller rotor back iron width and slot opening [6]; however, he only pointed out the relationship and didn't further study the parameter optimization. Zhang studied the radial force of switched reluctance motors using skewed slot structure based on finite element method. The simulated results show that using skewed slot could reduce the radial force [7]; however, he didn't consider the effects of other parameters on the radial force, such as air gap length, thickness and depth of

Submitted On: April 17, 2013
Accepted On: March 11, 2014

permanent magnet. Abbas used analytical and FEM to calculate the radial forces exerted on different parts of the coils [8]; however, he didn't consider the effects of the radial force on the vibration of the motor.

In addition, there were also some scholars who studied the structural optimization of motor stators. Choi presented a topology optimization method of IPM motor stator cores to reduce cogging torque. The optimization results show that configurations having dummy slots were desirable, but the number of dummy slots differed [9]. Kwack used the level set method to optimize the structure of motor stator in order to reduce torque ripples, by minimizing the difference between torque values at defined rotor positions and the constant target torque value under constrained material usage [10]. Both studied the torque, instead of the vibration of the motors. Additionally, they didn't use a 3-D model for the optimization.

This paper aims at the vibration reduction of IPM motor by the optimization of radial force and stator structure, which are the two main factors of motor vibration. It discusses the vibration behavior of IPM motor on electric vehicles via an experiment to investigate the main vibrational harmonic waves with high amplitudes. Then the parameters that have influences on the radial forces were optimized according to the sensitivity analysis, as well as the 3-dimentinal model of stator was optimized to reduce the dynamic response of the stator. Lastly, the final simulation of the optimized stator model excited by the optimized radial forces showed that the vibration level of the stator had declined to a large extent than that of the original model, which meant that the vibration behavior of the IPM stator was much better.

II. EXPERIMENTAL ANALYSIS

In this paper, in order to measure the vibration level of the IPM motor a test bench was established, which can take into account the effects of changing loads of torques. The noise was also measured; although, in this experiment we mainly focus on the vibration analysis.

A. Experiment introduction

In this paper, a test bench system was established to measure the vibration of the IPM motor used to drive electric vehicles, as shown in Fig. 1. The system included electric eddy current dynamometer, its controller and cooling water box as the loading subsystem, as well as the protective cover and sound absorption material as the sound isolating subsystem. Nine microphones were arranged around the motor, as shown in Fig. 2 (a) (black points); there were also 4 vibration acceleration transducers pasted on the surface of the motor, as shown in Fig. 2(b).

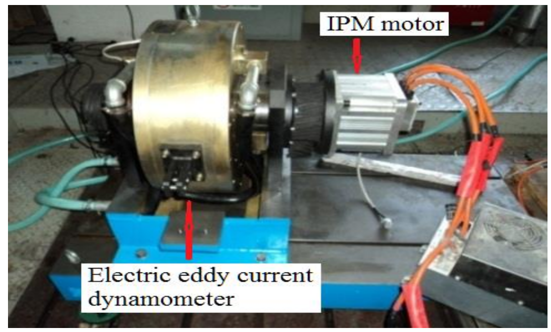

Fig. 1. Vibration test bench of IPM motor.

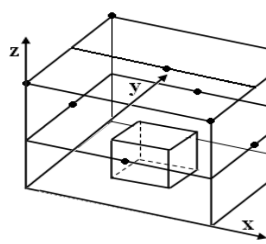

(a)

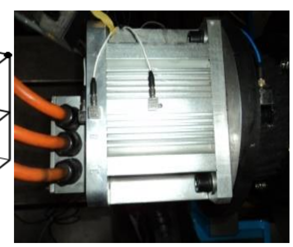

(b)

Fig. 2. Arrangement of microphones and vibration acceleration transducers.

In order to study the real vibration levels of the IPM motor on an electric vehicle, the working conditions of the testing motor should be the same as those working on electric vehicles. The working conditions of the motor in this experiment included steady ones and transient ones. The steady states of the motor corresponded to those when the vehicle drove with the velocity from 5 Km/h to 40 Km/h; every 5 Km/h as an increment. The transient conditions of the motor corresponded to those when the vehicle sped up with the velocity from 5 Km/h to 40 Km/h. The correspondent rotational speeds and torques were calculated according to the vehicles driving conditions. In this way, the vibration levels of the motor on the test bench were almost the same as on the electric vehicle.

B. Vibration analysis of experimental results

In order to study the relationship of the vibration level and the rotational speed of the motor, the paper carried out the frequency spectrum analysis of the vibration acceleration signals of the motor surface while the motor sped up. The waterfall of motor radial vibration acceleration is shown in Fig. 3.

It could be found from Fig. 3 that there were vibration harmonic waves that changed with the rotational speed; because the law is the same for any rotational speed, it was reasonable to choose one steady state of the motor for analysis to study the harmonic waves of the vibration spectrum. In addition, the rated condition was most often used and was representative; therefore, this paper chose the rated condition for study. The rotational speed was $n = 2400 r/\min$ and the torque was $T = 30 N/m$. The radial vibration frequency spectrum of the motor under this condition is shown in Fig. 4.

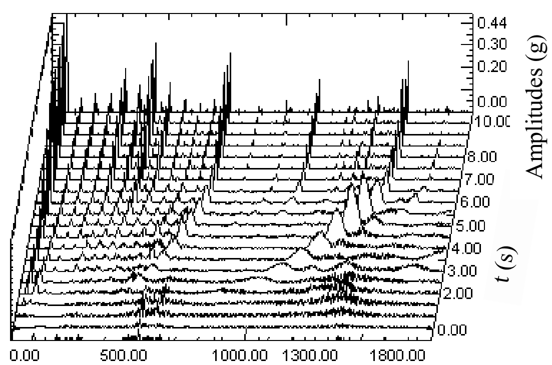

Fig. 3. Waterfall of motor radial vibration acceleration.

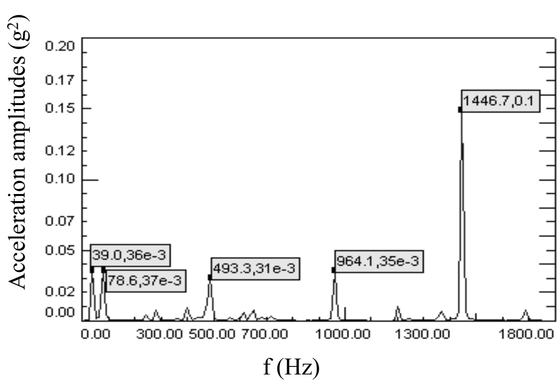

Fig. 4. Frequency spectrum of motor radial vibration acceleration.

For this working condition, the rotational frequency of the motor was $f = n/60 = 40Hz$. The frequency of controlling current was $f_1 = n \cdot p / 60 = 240 Hz$; where $p = 6$ was the number of pole-pairs of the motor. It was shown in Fig. 4 that the main components of motor vibration included the rotational frequency and its second harmonic frequency as well as the second, fourth, and sixth harmonic frequencies of the current frequency; where the sixth harmonic frequency has the highest amplitude.

As the rotational frequency and its second harmonic frequency were caused by the mechanical effects, this paper mainly studied the second, fourth and sixth harmonic waves of the current frequency of the vibration for optimization. Since the vibration of the IPM motor stator is mainly determined by the radial force and the stator structure, this paper implemented the optimization of the radial force and the stator structure, respectively in the following parts.

III. OPTIMIZATION OF RADIAL FORCE

A. Analytical calculation of radial force

According to Maxwell's law, the radial force was expressed as:

$$p_n(\theta,t) = \frac{b^2(\theta,t)}{2\mu_0}, \quad (1)$$

where μ_0 was the magnetic conductivity of air, $\mu_0 = 4\pi \times 10^{-7} H/m$ and $b(\theta,t)$ was air gap magnetic flux density.

The air gap magnetic flux density could be calculated by:

$$b(\theta,t) = \lambda(\theta,t) f(\theta,t), \quad (2)$$

where $\lambda(\theta,t)$ was the air gap magnetic permeance and $f(\theta,t)$ was the air gap magnetic potential.

The air gap magnetic permeance was composed by 4 parts, as in:

$$\lambda(\theta,t) = \Lambda_0 + \sum_{k1} \lambda_{k1} + \sum_{k2} \lambda_{k2} + \sum_{k1} \sum_{k2} \lambda_{k1} \lambda_{k2}, \quad (3)$$

where Λ_0 was the constant component, λ_{k1} was the harmonic wave magnetic permeance when the rotor was smooth and the stator was slotted and λ_{k2} was the harmonic wave magnetic permeance when the stator was smooth and the rotor was slotted.

The air gap magnetic potential was caused mainly by stator field current and rotor permanent magnet, as in:

$$f_c = \frac{N_c I_c}{2}, \tag{4}$$

$$f_m(\theta,t) = f_0(\theta,t) + \sum_v f_v(\theta,t) + \sum_\mu f_\mu(\theta,t), \tag{5}$$

$$f(\theta,t) = f_c + f_m(\theta,t), \tag{6}$$

where f_c was the air gap magnetic potential caused by stator field current, N_c was the number of coil in one slot, I_c was the current in one coil, $f_m(\theta,t)$ was the air gap magnetic potential caused by rotor permanent magnet, $f_0(\theta,t)$ was the synthetic magnetic potential of fundamental wave, $f_v(\theta,t)$ was the harmonic wave magnetic potential of stator winding and $f_\mu(\theta,t)$ was the harmonic wave magnetic potential of rotor.

As for the real motor in this paper, the rotor was smooth, the stator was slotted and there was no air gap permeance. Leaving out the vibration force waves of high orders and low amplitudes, the radial force was expressed as:

$$p_n(\theta,\text{t}) = \frac{1}{2\mu_0}\left\{\begin{array}{l}\frac{B_1^2}{2}\cos(2p\theta - 2\omega_1 t - 2\varphi_0) + \\ \sum_v \sum_\mu B_v B_\mu \cos[(\mu \pm v)\theta - (\omega_\mu \pm \omega_1)t - (\varphi_\mu \pm \varphi_v)]\end{array}\right\}. \tag{7}$$

In this formula, B_1 is the magnetic potential of the basic wave, p is the number of pole-pairs of the motor, θ is the angular displacement in the air gap, t is the time, μ, v are the orders of the harmonic waves, ω is the angular frequency of the harmonic wave and φ is the phase of the harmonic wave.

Similar with the working condition in the experiment, the radial force of the rated condition was calculated and the frequency spectrum is shown in Fig. 5.

Figure 5 shows that the main components of radial force included 480 Hz, 960 Hz and 1439 Hz, which are in accordance with the vibration frequency components measured in the experiment. They were respectively the second, fourth and sixth harmonic frequencies of the current frequency. Accordingly, the analytical calculation could reflect the harmonic waves of the radial force.

B. Magnetic finite element simulation

Magnetic finite element modeling:

For the 3-phase, 6-state IPM permanent motor with 18 teeth and 12 poles that was studied in this paper, the number of slots per pole per phase is 1/2. It was equal to 6 unit motors and each unit motor had 3 teeth and 2 poles. Since every unit motor had the same magnetic field, this paper used unit motors for magnetic simulation to save time. According to the real parameters of the motor, the magnetic model of 2 unit motors was established in ANSOFT. Then the stator, rotor, air gap and magnets were meshed with different sizes. After meshing of the model, the paper got the finite element model of the unit motors, as shown in Fig. 6.

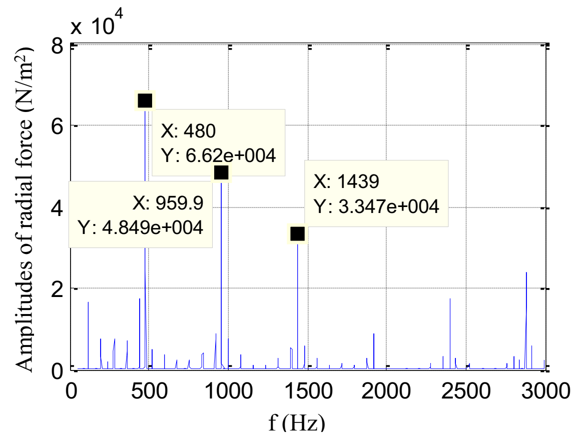

Fig. 5. Frequency spectrum of radial force in analytical method.

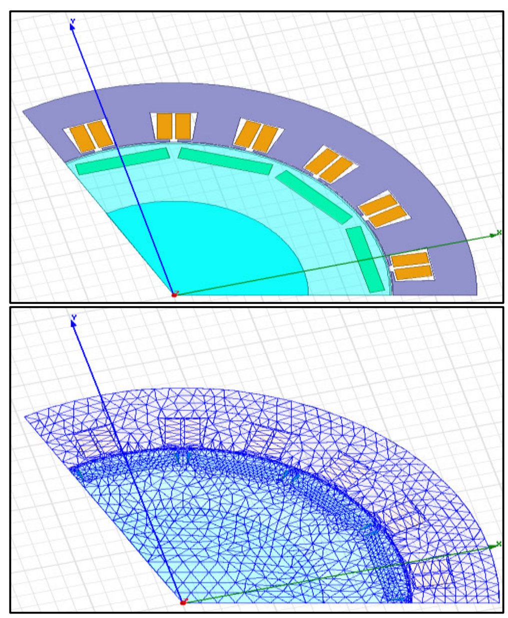

Fig. 6. Magnetic model and finite element model of the unit motors.

Calculation of radial force:

Under the rated working condition, the

rotating speed was 2400 r/min, the load was 18 N/m, the voltage was 120 v and the electric current frequency was 240 Hz. The Maxwell 2-D transient magnetic field solver was used for the simulation. The simulation step was 0.0001 s and the time duration was 0.5 s. For the finite element model of the unit motors under rated condition, the radial force in the air gap was calculated and its frequency spectrum is shown in Fig. 7.

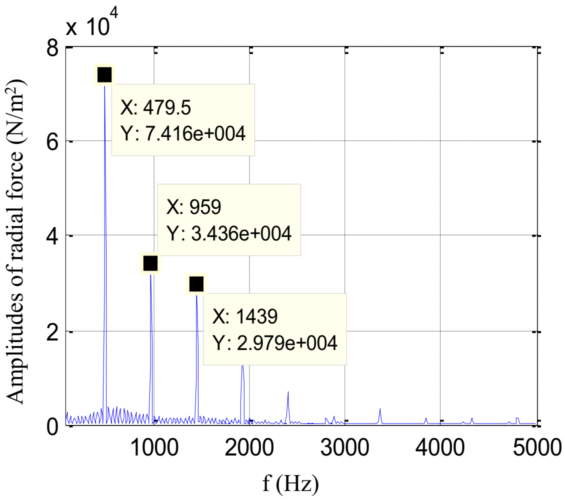

Fig. 7. Frequency spectrum of radial force in the air gap by simulation.

It was shown in Fig. 7 that the main frequencies of the radial force were the second, fourth and sixth harmonic frequencies of the current frequency. The results were in accordance with the main frequencies of analytical calculation, as in Fig. 5 and the experimental result, which confirmed the validity of the simulation. It was shown in both Figs. 5 and 7 that the energy of the second harmonic waves was more than 40% of the whole energy; the fourth and sixth harmonic waves were respectively about 20%. This means that the energy distribution and the ratio of harmonic waves were consistent. Considering that in the analytical calculation the equation (2) is an approximation, there is some deviation of the amplitudes between the analytical results and the simulation result. Therefore, the paper used the finite element model, which was more accurate than analytical model, for further analysis.

It was known from the experiment that the sixth harmonic wave of the current of the vibration had the highest amplitude, so the reduction of the amplitude of this wave in the radial force is the key for the improvement of the vibration behavior.

C. Parameter sensitivity analysis

It was obvious that the thickness and depth of the permanent magnet of IPM motor had an influence on the air gap flux density, which had an effect on the radial force. Additionally, the existing studies showed that the air gap length and the slot opening width also had an influence on the air gap flux density, which then affected the frequency and amplitude of the radial force [11]-[12]. This section used these four parameters for sensitivity analysis of the radial force under rated condition in order to choose the sensitive parameter intervals for optimization to get lower radial forces. Only one parameter changed at one time, the other settings remained unchanged. It should be noticed that the parameter ranges in this section all meet the requirement of design handbook of permanent magnetic motor, which means that the variations won't affect the performances of the motor too much [1].

The previous study in this paper showed that second, fourth and sixth harmonic waves of the radial force was the main exciting source of the vibration of the motor; therefore, this section mainly studied the parameter sensitivity to the second, fourth and sixth harmonic waves of radial force. During the study of the influence on the radial force of one parameter, other parameters remained unchanged. The studied ranges of the objective parameters were around and symmetrical about the original values of the motor. As the values were quite small, it is difficult and costly to manufacture extremely precise motors. Thus, it is not necessary to conduct a statistical study. The paper divided each parameter range into four intervals and four analysis, as shown in Table 1. Then when the value of the studied parameter is respective to the boundary values of the intervals, the second, fourth and sixth harmonic frequencies of the radial force are calculated. The results of the radial forces when the four parameters differed, are shown in Fig. 8. The comparison of the results indicated the laws that the radial force increased slowly with the increase of the width of stator slot openings, decreased slowly with the increase air gap length, increased rapidly with the increase of thickness of the permanent and decreased rapidly with the increase of depth of the permanent.

Table 1: Parameter intervals division

Parameters (mm)	Interval 1	Interval 2	Interval 3	Interval 4	Original Value
Slot opening width	(0.5, 1.5)	(1.5, 2.5)	(2.5, 3.5)	(3.5, 4.5)	2.5
Air gap length	(0.7, 0.8)	(0.8, 0.9)	(0.9, 1.0)	(1.0, 1.1)	0.9
Thickness of permanent magnet	(2.5, 3.5)	(3.5, 4.5)	(4.5, 5.5)	(5.5, 6.5)	4.5
Depth of permanent magnet	(0.1, 0.7)	(0.7, 1.3)	(1.3, 2.3)	(2.3, 3.3)	1.3

As the value of these four parameters differed so much, this paper used the following method to carry out the sensitivity analysis. Take the air gap length for example, the original air gap length was l_0 and the amplitude of sixth harmonic wave of the radial force was b_0. One interval of the air gap length was $l_1 \sim l_2$, when the air gap length was respectively l_1 and l_2, the corresponding amplitudes of sixth harmonic waves of the radial forces were b_1 and b_2. Then the change rate of air gap length in this interval was k_b, which was taken as the sensitivity index [13], was defined as:

$$k_b = \left[(b_2 - b_1)/b_0\right] / \left[(l_2 - l_1)/l_0\right].$$

It could be seen that k_b was a dimensionless quantity. It considered the original dimensions and the change at the same time so it could scientifically reflect the parameter sensitivity to radial force.

The change rates of other parameters were calculated in the same way with air gap length. The sensitivities of the four parameters in all intervals to the second, fourth and sixth harmonic waves are shown in Fig. 9. In Fig. 9, the positive and negative values meant that the amplitudes of radial force increased or decreased with the increase of the studied parameter.

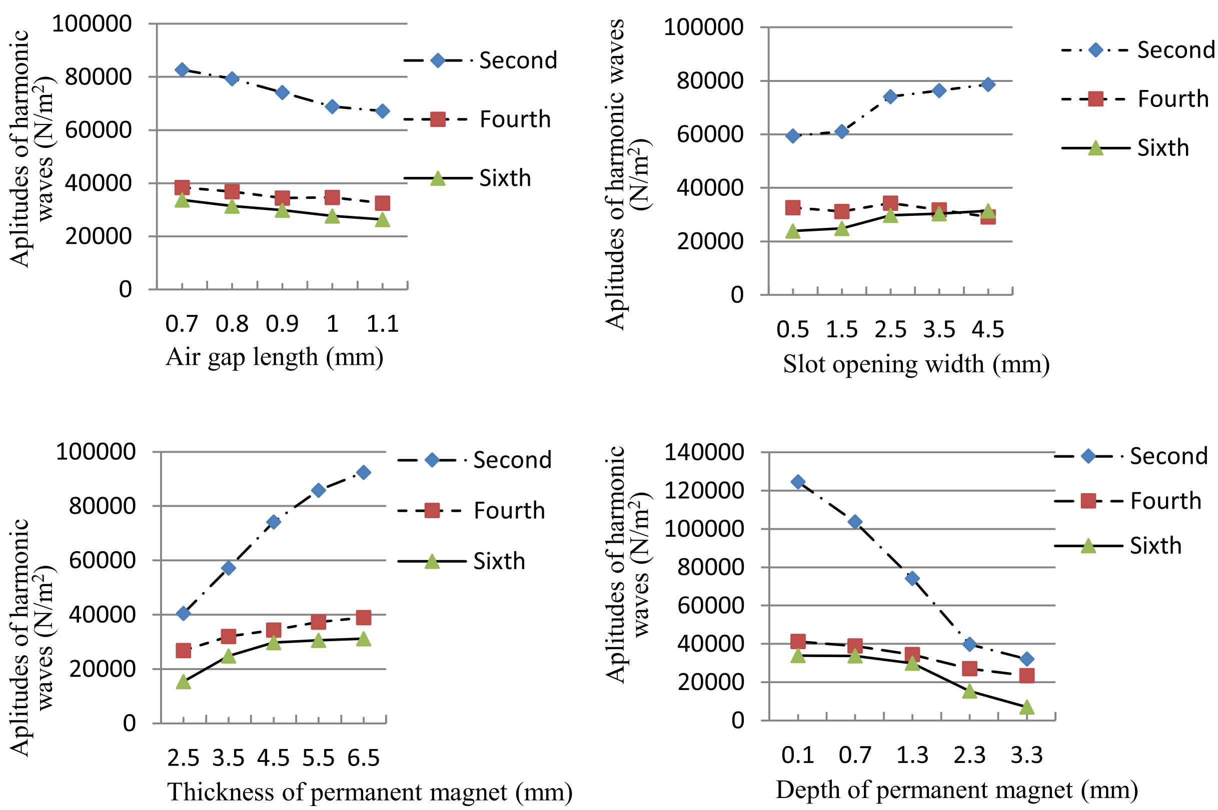

Fig. 8. Calculated radial forces of different parameters.

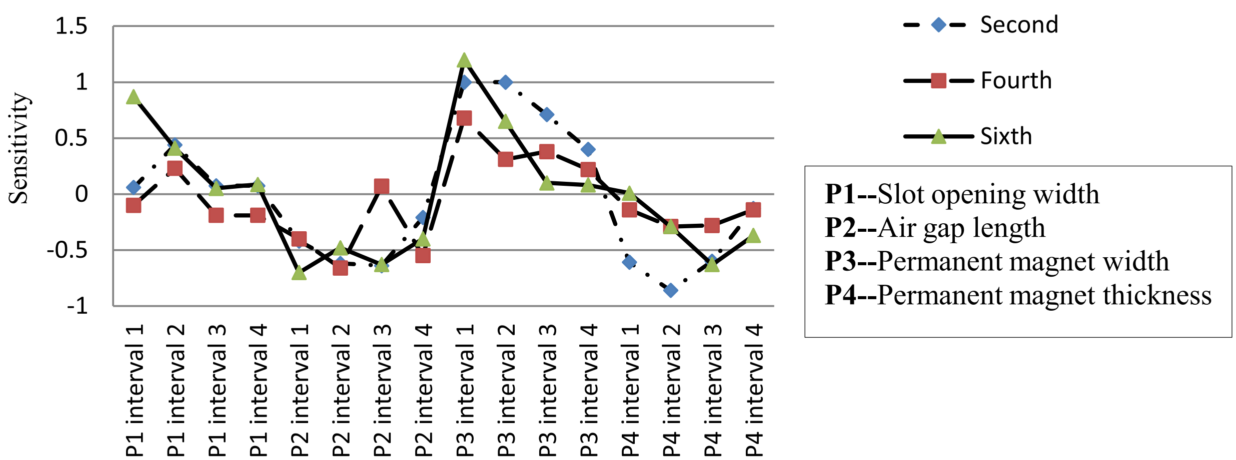

Fig. 9. Parameter sensitivities to the amplitudes of harmonic waves of radial force.

D. Parameter optimization

It was known from the previous analysis that it was important to reduce the amplitudes of the sixth harmonic waves of radial forces to reduce vibration. Those parameter intervals with high sensitivities to the sixth harmonic waves were interval 1 of width of permanent magnet, interval 3 of depth of permanent magnet, interval 1 and interval 2 of the width of stator slot opening, and all the intervals of the air gap length. Thus, the parameter values should be determined in these intervals respectively.

The paper determined the parameter values in order to achieve lower amplitudes of the radial forces according to what is analyzed above. The parameters should be chosen in the sensitive intervals and could result in smaller radial forces. In this way, the desired radial forces could be achieved without changing the parameters too much. Accordingly, the width of permanent magnet should be as small as possible in interval 1, the depth of permanent magnet should be as large as possible in interval 3 and the air gap length should be as large as possible in the four intervals. As for the stator slot opening width, the values in interval 1 were too small, which might lead to some errors and high costs of manufacture and installation. Also, with consideration of the sensitivity of the second and fourth harmonic waves, the value of slot opening width should be as small as possible in interval 2. Under the comprehensive consideration, the finally determined values of the parameters were shown in Table 2.

Table 2: Optimized parameter values

Parameters	Values (mm）
Thickness of permanent magnet	2.5
Depth of permanent magnet	2.3
Air gap length	1.1
Slot opening width	1.5

According to the optimized parameters in Table 2, the new finite element model of unit motors was established in software ANSOFT, to calculate the radial forces. The main frequencies of the radial force after optimization were the second, fourth and sixth harmonic frequencies of the current frequency; which were the same with those before optimization, but the amplitudes of the radial forces are optimized. The comparison of amplitudes of radial forces before and after optimization are shown in Table 3. It can be seen that the amplitudes of second, fourth and sixth harmonic waves had been reduced to a large extent; especially the amplitude of sixth harmonic wave, which declined by two-thirds.

IV. STATOR STRUCTURAL OPTIMIZATION

The purpose of the stator structural optimization in this paper was that when the weight and boundary dimension remained unchanged, the dynamic displacement responsecaused by the given excitation should be as small as possible. That is to say, when the excitation remains unchanged, the vibrational energy of the stator should be reduced to improve the vibration behavior of the motor.

Table 3: Force amplitudes of main harmonic waves

Harmonic Waves	Second	Fourth	Sixth
Original amplitude (mm)	74160	34360	29790
Optimized amplitude (mm)	39870	21990	9967
Optimized percentage	46%	36%	67%

A. Determination of parameters and objective function for optimization

This chapter carried out the stator structural optimization of IPM motor on electric vehicles. The study aimed to improve the dynamic response behavior of the stator without changing the performance of the motor. During the design of motors, inner diameter and effective length of the iron core were the main parameters that determined the performance of the motor. The original values of the motor structural parameters are shown in Table 4.

Table 4: Motor parameter values

Parameters	Values
No. of pole-pairs	2p = 6
Inner diameter of iron core	$D_{i1} = 130\,mm$
Outer diameter of iron core	$D_1 = 180\,mm$
Shell thickness	$\Delta h = 4mm$
Yoke thickness	14 mm
Length of iron core	86 mm

The existing study indicated that the parameters that had an influence on the vibration modes of motor stator were the shell thickness, outer diameter of iron core and thickness of stator yoke [14]. As the yoke thickness was associated with the inner and outer diameters of the stator, when the inner diameter remains unchanged, the yoke thickness changes with the outer diameter. Thus, this paper chose the outer diameter of iron core and shell thickness as optimization variables. During the optimization, the unchanged inner diameter and effective length of the iron core ensured the performance of the motor.

The original value of shell thickness was 4 mm, which was quite small. With consideration of the requirement of structural strength, the range of shell thickness for optimization should be a little larger, as 4~8 mm in this paper. In addition, the volume of the motor shouldn't be too large, so the stator boundary dimension was set as less than 5% larger than the original value. At the same time, the minimum of the stator yoke thickness was set as 5 mm to avoid the magnetic saturation. Accordingly, the range of outer diameter of the iron core was 81~90 mm.

The optimization was achieved in software ANSYS and the whole process was conducted with ANSYS Parameter Design Language. The range between the maximum and the minimum of the dynamic displacement that was the fluctuating amplitude of the dynamic displacement of the stator surface, reflected the vibration energy of the stator. In order to reduce the vibration level of the motor stator, it was effective to reduce the fluctuating amplitude of the dynamic displacement of the stator surface, which was chosen as the objective function for optimization in this paper.

Accordingly, the parameters were set as follows during the optimization:

(1) Design variables:
Outer radius of the iron core: 81~90 mm;
Shell thickness: 4~8 mm.

(2) State variables:
$R_1 - R_{i1} \geq 16mm$ (stator yoke thickness is not smaller than 5 mm)
Stator boundary dimension $\leq$ 1.05×190 mm (original value)

(3) Objective function:
Fluctuating amplitude of dynamic displacement of the stator surface.

B. Optimization result

The process was programmed with ANSYS Parameter Design Language. First, the 3-D model of stator was established, as shown in Fig. 10. Second, the model was excited by the time-domain radial forces calculated by simulation in chapter 3.2.2. Then the transient analysis started. During the calculation, the shell thickness and outer radius of the iron core of the model changed to another set of values, according to equal step sweeping method of ANSYS and another step of transient analysis began. During every step, the objective function was recorded and it changed with the step number of the optimization, as shown in Fig. 11. Figure 11 showed that the objective function of the 26th step number was the smallest, which meant the corresponding parameters were approximately the best. Then these parameters were rounded off, as shown in Table 5.

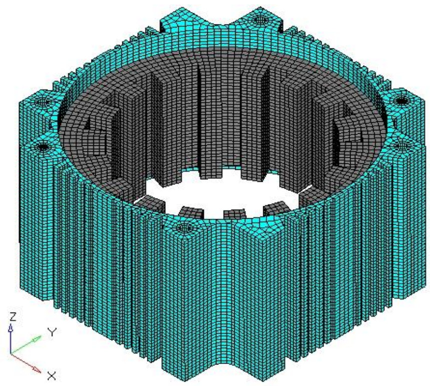

Fig. 10. Finite element model of the stator.

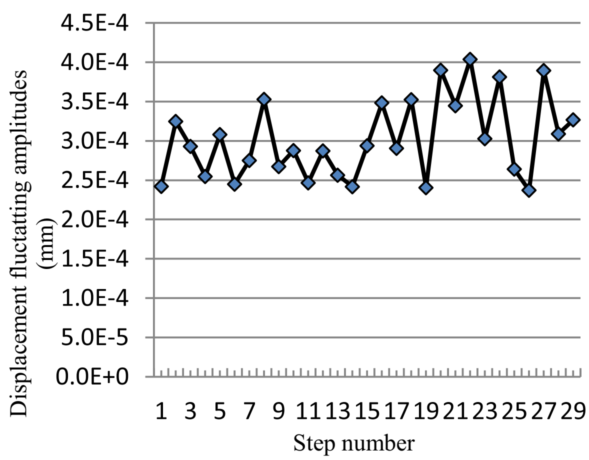

Fig. 11. Changes of objective function during optimization.

It was shown that after optimization the stator boundary dimension was only 2 mm larger than the original value, which met the requirement that it was less than 5% larger than the original value. Additionally, the outer diameter of the iron core decreased by 4 mm and the shell thickness increased by 4 mm. The transient displacement responses of the stator surface before and after optimization with the same excitation are shown in Fig. 12. The corresponding amplitudes of the main frequencies are shown in Table 6. In Table 6 it shows that after optimization the amplitudes of the main frequencies decreased to quite a large extent. That means that the dynamic response of the motor stator with the same excitation reduced after optimization.

Table 5: Parameters of motor stator after optimization

Parameters	Boundary Dimension	Outer Diameter of Iron Core	Shell Thickness
Values (mm)	192	176	8

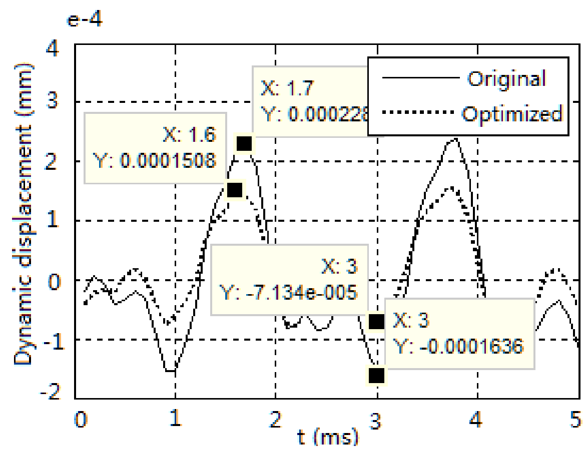

Fig. 12. Transient dynamic displacement responses of the stator before and after optimization.

Table 6: Displacement amplitudes of the main frequencies before and after optimization

Harmonic Frequencies	Second (480Hz)	Fourth (960Hz)	Sixth (1440Hz)
Original amplitude (mm)	6.69e-5	2.83e-5	5.12e-5
Optimized amplitude (mm)	3.85e-5	2.04e-5	3.68e-5
Percentage of optimization	42%	28%	28%

V. TRANSIENT DYNAMIC ANALYSIS OF THE OPTIMIZED MODEL

After the optimization of the radial force and the stator structure, a new model was established for simulation to verify the optimization effect. The optimized finite element model of the stator was excited by the optimized radial force for frequency response analysis.

Then the paper conducted the frequency

response analysis of the rated condition, which was a steady state. The results of the frequency response analysis showed that after optimization the main harmonic frequencies of the vibration acceleration were the same with those before optimization. They were 480 Hz, 960 Hz and 1439 Hz, which were the second, fourth and sixth harmonic frequencies of the current frequency; especially the sixth harmonic wave with the highest amplitude. The amplitudes of the main harmonic waves decreased to a large extent. The comparison of the amplitudes of the harmonic waves are shown in Table 7. It could be found from Table 7 that the average decrease of the amplitudes was 60%, which meant the optimization reduced the vibration level greatly. Accordingly, the optimization was quite ideal.

Table 7: Vibration acceleration amplitudes of main frequencies

Frequency (Hz)	480	960	1439
Original amplitudes (m/s^2)	0.7	0.6	1.9
Optimized amplitudes (m/s^2)	0.17	0.20	1.0
Percentage of optimization	76%	67%	37%

VI. CONCLUSION

The following conclusions could be drawn from this study on the analysis of the vibration behaviors of the motor and its optimization.

In this paper, the main vibration harmonic waves of the IPM motor on electric vehicles were investigated by frequency spectrum analysis of the experimental result. It was found that the second, fourth and sixth harmonic waves of the current frequency in the vibration had the highest amplitudes.

The optimization of the radial force based on the parameter sensitivity analysis could result in smaller radial forces without changing the parameters too much. It was also desirable to use the 3-D model of the stator for structural optimization to reduce the dynamic response of the stator.

The final transient dynamic simulation of the optimized model excited by the optimized radial forces showed that the vibration level decreased by 60% averagely, which verified the good effects of the optimization in this paper.

ACKNOWLEDGEMENT

The research was supported by the "973" program of China (2011CB711200) and the National Natural Science Foundation of China (51075302).

REFERENCE

[1] L. C. He, Study on electromagnetic noise of permanent magnet brushless DC drive motor for electric vehicle (in Chinese), Ph.D. Thesis, Tongji University of China, Shanghai, 2012.

[2] Z. Q. Zhu, D. Howe, E. Bolte and B. Achermann, Instantaneous magnetic field distribution in "Brushless permanent magnet DC motors, part I: open-circuit field." *IEEE Trans. Mag.*, vol. 29, no. 1, pp. 124-135, January 1993.

[3] Z. Q. Zhu and D. Howe, "Instantaneous magnetic field distribution in brushless permanent magnet DC motors, part II: armature-reaction field," *IEEE Trans. Mag.*, vol. 29, no. 1, pp. 124-135, January 1993.

[4] Z. Q. Zhu and D. Howe, "Instantaneous magnetic field distribution in brushless permanent magnet DC motors, part III: effect of stator slotting," *IEEE Trans. Mag.*, vol. 29, no. 1, pp. 124-135, January 1993.

[5] Z. Q. Zhu and D. Howe, "Instantaneous magnetic field distribution in brushless permanent magnet DC motors, part IV: magnetic field on load," *IEEE Trans. Mag.*, vol. 29, no. 1, pp. 124-135, January 1993.

[6] H. S. Chen and M. C. Tsai, "Design considerations of electromagnetic force in a direct drive permanent magnet brushless motor," *Journal of Applied Physics*, vol. 103, no. 7, pp. 7F117-1-3, April 2008.

[7] H. J. Zhang, J. J. Zhang and R. Z. Gao, "Radial force reduction for switched reluctance motor with skewed slot structure based on FEM," *Journal of Scientific and Industrial Research*, vol. 69, no. 8, pp. 594-599, August 2010.

[8] "Analytical and FEM based calculation of electromagnetic forces exerted on cylindrical coils due to their own current," *Applied Computational Electromagnetics Society Journal*, vol. 27, no. 11, pp. 866-872, November 2012.

[9] J. S. Choi, K. Izui, S. Nishiwaki, A. Kawamoto and T. Nomura, "Topology optimization of the stator for minimizing gogging torque of IPM motors," *IEEE Trans. Mag.*, vol. 47, no. 10, pp. 3024-3027, October 2011.

[10] J. Kwack, S. Min and J. P. Hong, "Optimal stator design of interior permanent magnet motor to reduce torque ripple using the level set method,"

IEEE Trans. Mag., vol. 46, no. 6, pp. 2108-2111, June 2010.

[11] X. Y. Wang, Q. Y. Wang and Y. F. Wang, "Analysis of the magnetic field of the six-phase disc PMSM and effect of air gap length on the air gap magnetic field," *2008 11th International Conference on Electrical Machines and Systems (ICEMS 2008)*, pp. 3212-3215, 2008.

[12] L. S. Stephens and M. A. Casemore, "Influence of stator slot geometry and rotor eccentricity on field distribution in cylindrical magnetic actuators," *IEEE Trans. Mag.*, vol. 38, no. 2, pp. 1348-1356, March 2002.

[13] D. M. Hamby, "A review of techniques for parameter sensitivity analysis of environmental models," *Environmental Monitoring and Assessment*, vol. 32, no. 2, pp. 135-154, September 1994.

[14] R. F. Chen, Study of vibration and noise characteristics and optimal design of stator of brushless DC drive motor (in Chinese), Master Thesis, Tongji University of China, Shanghai, 2011.

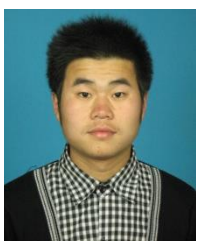

Longyang Xiang a PhD candidate majoring in Vehicle Engineering at Tongji University, Shanghai, China. He received his Bachelor degree of Mechanical Engineering in 2010 from Hunan University, Changsha, China. His main research interests are in the control of vibration and noise of vehicles and analysis and design of mufflers.

Shuguang Zuo a professor at Tongji University, Shanghai, China. He received his B.S. degree in Mechanical Design and Manufacture from Hunan Agricultural University, Changsha, China in 1990 and his M.S. and Ph.D. degrees in Vehicle Engineering from Jilin University, Changchun, China in 1993 and 1996, respectively. He joined Tongji University, Shanghai, China, as Associate Professor in 1998, then he became a professor in 2004. His main research interests are in the control of vibration and noise of vehicles and vehicle system dynamics.